



UNIVERSIDADE  
FEDERAL  
DE PERNAMBUCO



**Universitat de les  
Illes Balears**

## **Anticipated synchronization in neuronal circuits**

Fernanda Selingardi Matias

Advisors: Mauro Copelli and Claudio R. Mirasso

Joint PhD  
Universidade Federal de Pernambuco  
Universitat de les Illes Balears  
March 2014

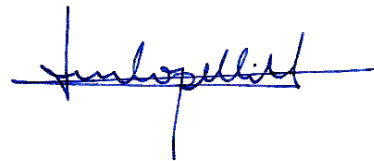
Claudio Rubén Mirasso Santos, catedrático de la Universidad de las Islas Baleares y Mauro Copelli, Professor Adjunto 3 de Universidade Federal de Pernambuco, Brasil,

CERTIFICAN

Que la presente memoria de tesis, titulada “Anticipated Synchronization in Neuronal Circuits”, ha sido realizada por Fernanda Selingardi Matias bajo su dirección en el Instituto de Física Interdisciplinar y Sistemas Complejos (CSIC-UIB) y el Departamento de Física de la Universidade Federal de Pernambuco, y para dar constancia firman la misma.



Claudio Mirasso Santos  
Director



Mauro Copelli  
Director



Fernanda Selingardi Matias  
Doctoranda

*If the brain were simple enough for us to understand it, we would be too  
simple to understand it"*

—KEN HILL



# Resumo

Sincronização antecipada (AS, do inglês "anticipated synchronization") é uma forma de sincronização que ocorre quando uma influência unidirecional é enviada de um transmissor para um receptor, mas o receptor lidera o transmissor no tempo. Esta sincronização contra-intuitiva pode ser uma solução estável entre dois sistemas dinâmicos acoplados em uma configuração mestre-escravo quando o escravo recebe uma retroalimentação atrasada e negativa. Diversos exemplos de AS foram encontrados em diferentes sistemas, no entanto, faltam evidências experimentais de AS no cérebro. Nessa tese, nós investigamos a existência de AS em uma rede neuronal do tipo mestre-escravo quando a retroalimentação atrasada e negativa é substituída por um circuito inibitório dinâmico mediado por sinapses químicas. No nível neuronal, mostramos a existência de AS em um microcircuito de 3 neurônios e em um de 3 populações neuronais nos quais a retroalimentação é proporcionada ou por um interneurônio ou por uma subpopulação de neurônios inibitórios. Uma transição suave de sincronização atrasada (DS, do inglês "delayed synchronization") para AS ocorre quando a condutância sináptica inibitória é aumentada. Mostramos que o fenômeno é robusto quando variamos os parâmetros dos modelos dentro de um intervalo fisiológico aceitável. Os efeitos da plasticidade sináptica dependente do tempo nas transições DS-AS também foram investigados. Os resultados obtidos a partir dos nossos modelos são comparáveis a dados obtidos experimentalmente enquanto macacos realizam certas atividades cognitivas. Em alguns casos, uma influência unidirecional dominante de uma região cortical para outra pode vir acompanhada de um tempo de atraso tanto positivo como negativo. Apresentamos um modelo para AS entre duas regiões cerebrais e comparamos estes resultados com os dados experimentais, obtendo excelente concordância.

**Palavras-chave:** Sincronização Antecipada, Modelos Neuronais, Retroalimentação Inibitória, Curva de Resposta de Fase, Plasticidade Sináptica Dependente do Tempo, Causalidade, Análise de Dados.



# Resumen

La sincronización anticipada (SA) es una forma de sincronización que se produce cuando una influencia unidireccional se transmite desde un emisor a un receptor, pero el sistema receptor adelanta al emisor en el tiempo. Este fenómeno, contrario a la intuición, puede ser una solución estable de dos sistemas dinámicos acoplados en una configuración maestro - esclavo cuando el esclavo está sujeto a una retroalimentación negativa retardada. Hay muchos ejemplos de SA que se han encontrado en diferentes sistemas, sin embargo, no existe evidencia ni teórica ni experimental de que ocurra en el cerebro. En este trabajo de tesis se investiga la existencia la SA en circuitos neuronales cuando la realimentación retardada se sustituye por un bucle inhibitorio mediado por sinapsis químicas. A nivel neuronal, se muestra la existencia de SA en circuitos de 3 neuronas o 3 poblaciones de neuronas, donde la retroalimentación la proporciona una interneurona o una subpoblación de neuronas inhibitorias. Una transición de sincronización retrasada (SR) a SA se produce suavemente cuando se incrementa la conductancia sináptica inhibitoria. Se encuentra que el fenómeno es robusto para una amplio espectro de parámetros del modelo dentro del rango fisiológico. También se investiga el papel de la plasticidad neuronal en la transición SR-SA. Los resultados obtenidos a partir del modelo se comparan con los obtenidos experimentalmente en monos cuando realizan ciertas tareas cognitivas. En algunos casos, una influencia direccional dominante de un área cortical a otra se acompaña de un retardo que puede ser negativo o positivo. Se presenta un modelo para las relaciones entre dos regiones corticales del cerebro y se compararan los resultados numéricos con los datos experimentales, obteniendo un excelente acuerdo.

**Palabras clave:** Sincronización Anticipada, Modelos Neuronales, Retroalimentación inhibitoria, Curva de Respuesta de Fase, Plasticidad Sináptica Dependiente del Tiempo, Causalidad, Análisis de Datos.





# Abstract

Anticipated Synchronization (AS) is a form of synchronization that occurs when a unidirectional influence is transmitted from an emitter to a receiver, but the receiver system leads the emitter in time. This counterintuitive phenomenon can be a stable solution of two dynamical systems coupled in a master-slave configuration when the slave is subject to a negative delayed self-feedback. Many examples of AS dynamics have been found in different systems, however, theoretical and experimental evidence for it in the brain has been lacking. In this thesis work we investigate the existence of AS in neuronal circuits when the delayed feedback is replaced by an inhibitory loop mediated by chemical synapses. At the neuronal level, we show the existence of AS in 3-neuron or 3-neuron-populations microcircuits, where the self-feedback is provided either by an interneuron or by a subpopulation of inhibitory neurons. A smooth transition from delayed synchronization (DS) to AS typically occurs when the inhibitory synaptic conductance is increased. The phenomenon is shown to be robust for a wide range of model parameters within a physiological range. The role of spike-timing-dependent plasticity in DS-AS transitions is also investigated. The results obtained from the model are compared with those obtained experimentally in monkeys performing certain cognitive tasks. In some cases a dominant directional influence from one cortical area to another is accompanied by either a negative or a positive time delay. We present a model for AS between two brain regions and compare its results to the experimental data, obtaining an excellent agreement.

**Keywords:** Anticipated Synchronization, Neuronal models, Inhibitory feedback, Phase Response Curve, Spike-timing Dependent Plasticity, Causality, Data Analysis.



# Contents

<b>1</b>	<b>Introduction</b>	<b>1</b>
1.1	What is Anticipated Synchronization?	1
1.1.1	Physical systems	2
1.1.2	Biological systems	3
1.1.2.1	The inhibitory feedback loop	4
1.2	Brief computational neuroscience overview	5
1.2.1	Neuronal level	5
1.2.2	Chemical synapses	8
1.2.3	Neuronal populations	9
1.2.4	Synchronization in the brain	9
1.3	Experimental considerations	10
<b>2</b>	<b>Anticipated synchronization in microcircuits</b>	<b>13</b>
2.1	Master-Slave-Interneuron: the 3-neuron motif	13
2.1.1	Neuron model	14
2.1.2	Synaptic coupling	15
2.2	Three dynamical regimes	16
2.2.1	Phase-locking: delayed and anticipated synchronization	16
2.2.2	Phase-drift	17
2.3	Scanning parameter space	19
2.4	The effect of a common Driver	22
2.5	Neuronal chain networks	25
2.6	Proposed experiment	26
2.6.1	The hybrid patch clamp setup	26
2.6.2	Modified Hodgkin-Huxley model	28
2.6.3	AS in the presence of noise	29
2.7	Other motifs	31
2.7.1	Bidirectional coupling	31
2.7.2	An extra slave	34
2.7.3	Motor circuit in the spinal cord	34
<b>3</b>	<b>Phase response curve</b>	<b>39</b>
3.1	What is it and why is it useful?	39
3.2	Master-Slave: two unidirectionally coupled oscillators	42
3.2.1	Poincaré phase map	42

3.3	Slave-Interneuron: bidirectional coupling	42
3.3.1	Stability analysis	44
3.4	Master-Slave-Interneuron coupling	44
3.4.1	Particular case	46
3.4.2	Stability Analysis	46
3.4.3	Phase model	47
3.5	Numerical results	48
<b>4</b>	<b>Neuronal populations</b>	<b>51</b>
4.1	Modeling collective oscillations in large-scale systems	51
4.1.1	Cortico-cortical network	52
4.1.2	Defining time delay in the model	53
4.2	How to characterize AS?	55
4.2.1	LFP scale	56
4.2.2	Neuronal scale	58
4.3	Robustness in parameter space	59
4.4	Modified motifs	60
4.4.1	Slave-Interneuron as one cortical population	60
4.4.2	Bidirectional coupling	61
4.5	Changing neuronal variability of the Slave	63
4.6	A toy model for the thalamus	64
4.7	Stability analysis of phase-locking regimes between neuronal populations	67
4.8	Discussion	70
4.8.1	Neuronal populations can exhibit AS	70
4.8.2	Different synchronization regimes within the same anatomical connectivity	70
<b>5</b>	<b>Cortical data analysis</b>	<b>73</b>
5.1	More realistic features	74
5.2	Data acquisition	76
5.3	Granger causality	76
5.3.1	Causality measures in neuroscience	77
5.4	Spectral Analysis of LFP and simulation data.	78
5.5	Comparing data and model	79
5.5.1	Model reproduces experimental coherence and GC spectra	80
5.6	Discussion	82
5.6.1	Relative time delay is a poor indicator of directional influence	82
5.6.2	Correspondence between dynamical synchronization regime and functional brain state	82
5.6.3	Effective connections and functional significance	83
<b>6</b>	<b>The interplay between spike-timing dependent plasticity and anticipated synchronization in the organization of neuronal networks</b>	<b>85</b>
6.1	Synaptic plasticity	85

6.1.1	Spike-timing-dependent plasticity (STDP)	86
6.2	AS and STDP synergetically organize the network dynamics	88
6.3	STDP in the 3-neuron motif	88
6.4	STDP between neuronal populations	92
6.4.1	AS in the presence of STPD: an emergent property	92
6.4.2	Hybrid STDP and AS stabilize synaptic weight distribution	94
6.4.3	Other STDP rules	94
<b>7</b>	<b>Concluding remarks and further perspectives</b>	<b>97</b>



# Introduction

The desire to understand nature is the moving force that makes science advance. The ability to make models about the world and use them to predict facts and act on them is not just intrinsically related to our daily researches, but also to our everyday life. This is the very evidence that one of the specialties of our brain is to make models. In an extreme view, our brain is the machine that constructs the (models of) reality [1].

What mechanisms allow us to model and predict facts are one of the great questions in neuroscience. In Buzsaki’s words, “brains are foretelling devices and their predictive powers emerge from the various rhythms they perpetually generate” [2]. Exposing the mechanisms that allow complex things to happen in a coordinated way in the brain has produced some of the most spectacular discoveries in the field. These synchronized activities in the brain are the subject of this Thesis. In particular, we are interested in the time differences between synchronized components.

## 1.1 What is Anticipated Synchronization?

Synchronization is an astonishing universal collective phenomenon. It has been reported in a striking variety of physical and biological systems, spanning from the subatomic to the astronomical scales. The history of synchronized oscillators goes back to Huygens’ work with two weakly coupled pendulum clocks. In a classical context, synchronization means adjustment of rhythms of self-sustained periodic oscillators due to their weak interaction. In the past decades an increased interest in the topic of synchronization of chaotic systems has arisen [3]. It was in the context of coupled chaotic units that the concept of anticipated synchronization was discovered [4, 5, 6].

Two identical autonomous dynamical systems coupled in an unidirectional configuration (that we call master-slave) can be described by the following equations:

$$\begin{aligned}\dot{\mathbf{x}} &= \mathbf{f}(\mathbf{x}(t)), \\ \dot{\mathbf{y}} &= \mathbf{f}(\mathbf{y}(t)) + K[\mathbf{x}(t) - \mathbf{y}(t - t_d)],\end{aligned}\tag{1.1}$$

if the second system (the slave) is subjected to a negative delayed self-feedback.  $\mathbf{x}$  and  $\mathbf{y} \in \mathbb{R}^n$  are dynamical variables representing the master and the slave,  $\mathbf{f}(\mathbf{x})$  is a vector function which defines the autonomous dynamical system,  $K$  is a matrix representing a coupling parameter and  $t_d$  is a positive constant delay time.

The presence of the feedback, or the “memory term”, enables the existence of a trivial solution  $\mathbf{y}(t) = \mathbf{x}(t + t_d)$ , which can be easily verified by direct substitution in the system above.

The striking aspect of this solution is its meaning: the state of the driven system  $\mathbf{y}$  anticipates the driver's state  $\mathbf{x}$ . In other words, the slave predicts the master. This counter-intuitive synchronization manifold, called “anticipated synchronization” (AS) was discovered in 2000, by Voss [4]. The existence of AS is even more remarkable when the dynamics of the master system  $\mathbf{x}$  is “intrinsically unpredictable” as in chaotic systems [4, 6, 5]. Along these years, AS has been shown to be stable in a plenty of scenarios, including theoretical and experimental works.

Voss also proposed another coupling scheme that could exhibit AS [4]. The “complete replacement” was described by:

$$\begin{aligned}\dot{\mathbf{x}} &= -\alpha\mathbf{x}(t) + \mathbf{f}(\mathbf{x}(t-t_d)), \\ \dot{\mathbf{y}} &= -\alpha\mathbf{y}(t) + \mathbf{f}(\mathbf{x}(t)).\end{aligned}\tag{1.2}$$

The manifold  $\mathbf{y}(t) = \mathbf{x}(t+t_d)$  is also a solution of this system. In this situation, the anticipation time can be arbitrarily large, while the stability of AS in the former case (Eq. 1.1, called “delay coupling”) requires some constraints on the constant delay time  $\tau$  and coupling  $K$  [4, 6, 5]. Despite this fact, the delay coupling scheme is more interesting since we can maintain the master's dynamics unperturbed and change just the slave's couplings. In this Thesis we will deal with the former case.

### 1.1.1 Physical systems

When Voss introduced the concept of AS, he proposed that it would open new avenues in the study, prediction and control of chaotic systems [4, 6, 5]. Indeed, one of the first numerical verification of AS was done by Masoller [7] in the following year. She numerically found anticipated synchronization regime in a model of two chaotic semiconductor lasers with optical feedback when a small amount of the intensity of master laser was injected coherently into the slave laser.

AS was also observed between delayed-coupled chaotic maps [8]. Masoller and Zanette analytically studied the stability properties of the synchronized states. Since time delays in maps are discrete, the dimensionality of the problem remains finite, whereas ordinary differential equations with finite time delays mathematically constitute an infinite-dimensional system. Depending on the parameters, the maps may present AS or delayed synchronization (the usual retarded or lag synchronization). Hernández-García et al. [9] studied two types of coupled chaotic maps, 1D Bernoulli-like maps and 2D Baker maps, in which an analytic treatment of the stability of the AS regime was possible. They also showed that the numerical simulations were in good agreement with the analytic predictions.

The first experimental observations of AS was done by Sivaprakasam et al. [10]. They handled two diode lasers as transmitter and receiver. The master laser was rendered chaotic by the application of an optical feedback from an external-cavity. This experimental verification of anticipating chaotic synchronization unveiled great opportunities for application in optical communications, information processing, and in controlling delay induced instabilities in a wide class of nonlinear systems.

Other experiments with unidirectionally coupled lasers reported anticipated and delayed synchronization (DS) regimes, depending on the difference between the transmission time and



the feedback delay time [11, 12]. The two regimes were observed to have the same stability of the synchronization manifold in the presence of small perturbations due to noise or parameter mismatches [12].

AS was also verified in experiments with electronic circuits [13, 14, 15, 16]. The electronic circuits allow for a real-time anticipation of even strongly irregular signals. It was found that synchronization of the driven circuit with chaotic future states of the driving circuit is insensitive to signal and system perturbations. [13, 14]. Moreover, a transition from AS to DS through zero-lag synchronization with excitatory and inhibitory couplings, as a function of the coupling delay, was reported in [17, 18].

A simple linear analysis was employed by Calvo et al. [19] to show the minimal requirements necessary to reproduce AS. Numerically, AS was observed in two dissipative deterministic ratchets driven externally by a common periodic force [20], in unidirectionally coupled ring and linear arrays of chaotic systems [21, 22], in a single system having two different time delays (the feedback and coupling delay [23]), and in a new coupling scheme with varying time delay [24]. Moreover, AS has been used as a mechanism to estimate the parameters of chaotic systems [25], to predict [26] and to control chaotic trajectories [27, 28].

An algorithm of coupling design for a long-term anticipation time was proposed by [29]. Its efficacy was demonstrated for the Rössler system, the double-scroll Chua circuit, and the Lorenz system. The algorithm is based on phase-lag compensation in the time-delay feedback term of the slave system. The maximum prediction time attained with this algorithm is larger than that obtained with the diagonal coupling usually used in the literature.

A new method for achieving AS without the time delay in unidirectionally coupled chaotic oscillators was proposed in 2005 [30]. The method uses a specific parameter mismatch between the drive and response that is a first-order approximation to true time delay coupling. The stability analysis, numerical results and an experimental observation of the effect in radio-frequency electronic oscillators was presented [30].

### 1.1.2 Biological systems

After several works in physical systems, a reasonable question arises whether AS can appear in natural (not man-made) systems. In his first paper about AS, Voss already proposed the investigation of physiological systems: “Since the underlying mechanisms are so simple, it should be worth searching for synchronization in physiological systems, where delayed feedback dynamics seem to play a crucial role [31]. In particular, arrays of phase-locked oscillators are suspected to be important for an understanding of neuronal information processing, and the introduction of a physiologically motivated time delay may improve such models [32].”

The first attempt to find AS in biological inspired systems was done by Cizak et al. [33]. They studied two unidirectionally coupled FitzHugh-Nagumo neuron models in the presence of negative delayed self-feedback in the slave (see Fig. 1.1). They showed that AS occurs in this non-autonomous dynamical system, driven by white noise [33, 34, 35]. In such models, even when the neurons were tuned to the excitable regime, the slave neuron was able to anticipate the spikes of the master neuron, working as a predictor [14].

In 2013 Pyragienė and Pyragas [36] investigated AS in nonidentical chaotic neuronal models unidirectionally coupled in a master-slave configuration without a time delay feedback.

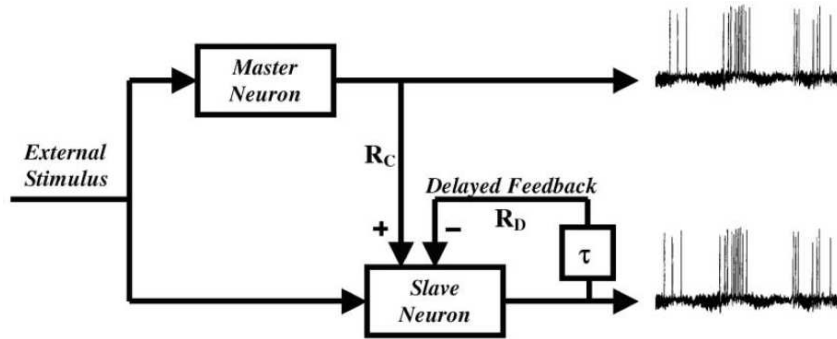


Figure 1.1: Schematic representation of two model neurons coupled in a master-slave configuration, with a negative delayed self-feedback loop (characterized by the delay time  $t_d = \tau$  in Eq. 1.1) in the slave neuron. Reproduced from Cizak et al. [33].

Based on the modified scheme proposed in [30], they replaced the feedback term  $K(x(t) - y(t - t_d))$  in Eq. 1.1 by the simpler coupling without a time delay:  $K(x(t) - y(t))$ . They showed that if the parameters of chaotic master and slave systems are mismatched in such a way that the mean frequency of a free slave system is greater than the mean frequency of a master system, then both the AS and DS regimes can be achieved. In fact, the slave neuron anticipates the chaotic spikes of the master neuron for coupled Rössler systems as well as for two different neuron models: the Hindmarsh-Rose and the adaptive exponential integrate-and-fire neurons [36].

#### 1.1.2.1 The inhibitory feedback loop

Though potentially interesting for neuroscience, it is not trivial to compare these theoretical results with real neuronal data. The main difficulty lies in requiring that the membrane potentials of the involved neurons be diffusively coupled. While a master-slave coupling of the membrane potentials could in principle be conceived by means of electrical synapses (via gap junctions) [37] or ephaptic interactions [38], no biophysical mechanism has been proposed to account for the delayed inhibitory self-coupling of the slave membrane potential employed by Cizak et al. [33, 34, 14].

In the brain, the vast majority of neurons are coupled via chemical synapses, which can be excitatory or inhibitory. In both cases, the coupling is directional and highly nonlinear, typically requiring a suprathreshold activation (e.g. a spike) of the pre-synaptic neuron to trigger the release of neurotransmitters. These neurotransmitters then need to diffuse through the synaptic cleft and bind to receptors in the membrane of the post-synaptic neuron. Binding leads to the opening of specific channels, allowing ionic currents to change the post-synaptic membrane potential [37]. This means that not only the membrane potentials are not directly coupled, but the synapses themselves are dynamical systems.

We proposed to bridge this gap investigating whether AS can occur in biophysically plausible model neurons coupled via chemical synapses. More interesting, we replaced the self-feedback loop by a dynamical inhibitory loop mediated by an interneuron [39]. Such inhibitory feedback loop is one of the most canonical neuronal motifs in the brain [40, 41]. It was found

to play several important roles, for instance, in the spinal cord [42], thalamus [43, 44], cortex, etc. Furthermore, we extend our results to population models in which the inhibitory loop is mediated by a pool of interneurons. The existence of AS mediated by a dynamical inhibition unveils several possibilities in the investigation of AS in other biological systems.

## 1.2 Brief computational neuroscience overview

The brain is a complex system whose components create networks that continually generate complex patterns. These brain networks span over multiple temporal and spatial scales. The notion that the brain can be fully reduced to the operation of neurons or, in the opposite view, that cognition can be understood without making reference to its biological substrates are exaggerated simplifications [45]. Although several brain regions show significant specialization, higher functions such as cross-modal information, integration, abstract reasoning and conscious awareness are viewed as emerging from interactions across distributed functional networks. Indeed, most brain functions are thought to rely on the interrelationship between segregation and integration. The coexistence of these two principles is considered the origin of neural complexity [45]

Once the cellular machinery for generating impulses and for transmitting them rapidly between cells had evolved, connectivity became a way by which neurons could generate diverse patterns of response and mutual statistical dependence. Connectivity allows neurons to act both independently and collectively. In this sense, the brain function is fundamentally integrative; it requires that components and elementary processes work together giving rise to complex patterns. Connectivity is essential for integrating the actions of (segregated) individual neurons and thus for enabling cognitive processes such as perception, attention, and memory. Connectivity translates unitary events at the cellular scale into large scale patterns.

### 1.2.1 Neuronal level

Neurons fire spikes and their main behaviors are described by their action potentials. Therefore, neurons can be classified by their firing patterns, for example, regular spiking (RS), intrinsically bursting (IB), chattering (CH), fast-spiking (FS), low-threshold spiking (LTS), thalamo-cortical (TC) or resonator (RZ) Typical responses of each of these classes to an external applied current  $I(t)$  are shown in Fig. 1.2.

The most simple models representing a minimal biophysical interpretation for an excitable neuron are the conductance-based models. The first model of spiking neurons was proposed by Alan Lloyd Hodgkin and Andrew Huxley in 1952 [46]. It describes the ionic mechanisms underlying the initiation and propagation of the action potentials in the squid giant axon. The precise mathematical description of the axon was possible due to two main features. First, this axon has a large length and diameter, which permitted electrophysiological intracellular recordings. Second, it has mainly two types of voltage gated ion channels. Since ion channels are selective to particular ionic species, such as sodium or potassium, they give rise to specific

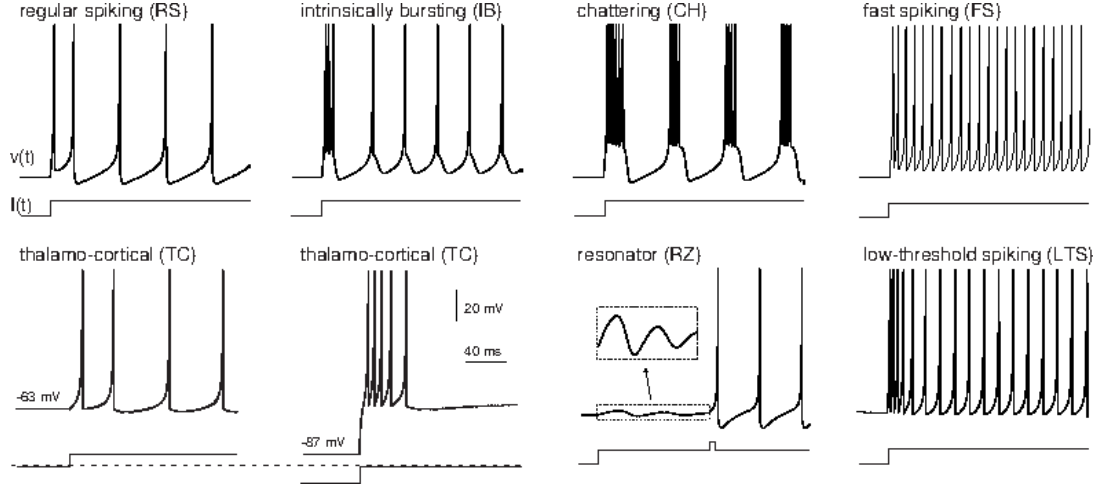


Figure 1.2: Examples of different firing patterns that neurons can exhibit. Electronic version of the figure and reproduction permissions are freely available at [www.izhikevich.org](http://www.izhikevich.org).

ionic currents. The capacitive current is equal to the sum of all ionic currents:

$$C_m \frac{dV}{dt} = \sum I_{ion} \quad (1.3)$$

where  $C_m$  is the membrane capacitance of the cell and the ionic current associated to ion  $x$  follows the Ohm's law:  $I_x = G_x(E_x - V)$ .  $E_x$  is the reversal potential of the ion and  $G_x$  is the channel conductance. It is proportional to the maximum conductance  $\bar{G}_x$  and the dynamical variables describing the activation or inactivation of the channels.

Therefore, the complete model consists of four coupled ordinary differential equations associated to the membrane potential  $V$  and the ionic currents flowing across the axonal membrane corresponding to the  $\text{Na}^+$ ,  $\text{K}^+$  and leakage currents. The gating variables for sodium are  $h$  and  $m$  and for potassium is  $n$ :

$$C_m \frac{dV}{dt} = \bar{G}_{Na} m^3 h (E_{Na} - V) + \bar{G}_K n^4 (E_K - V) + G_m (V_{rest} - V) + I + \sum I_{syn} \quad (1.4)$$

$$\frac{dx}{dt} = \alpha_x(V)(1-x) - \beta_x(V)x, \quad (1.5)$$

where  $x \in \{h, m, n\}$ . The voltage dependent rates  $\alpha_x$  and  $\beta_x$  were fitted experimentally in the seminal work of Hodgkin and Huxley [46].

In its simplest version, the Hodgkin-Huxley (HH) model represents a neuron by a single isopotential electrical compartment, neglects ion movements between subcellular compartments, and represents only ion movements between the inside and outside of the cell. There are several more detailed models, called multi-compartmental models [47, 48, 49], which take into account, for example, neuronal morphology and spatial distribution of ion channels. In the opposite direction, several reduced models [50, 51, 52] are available in order to describe with

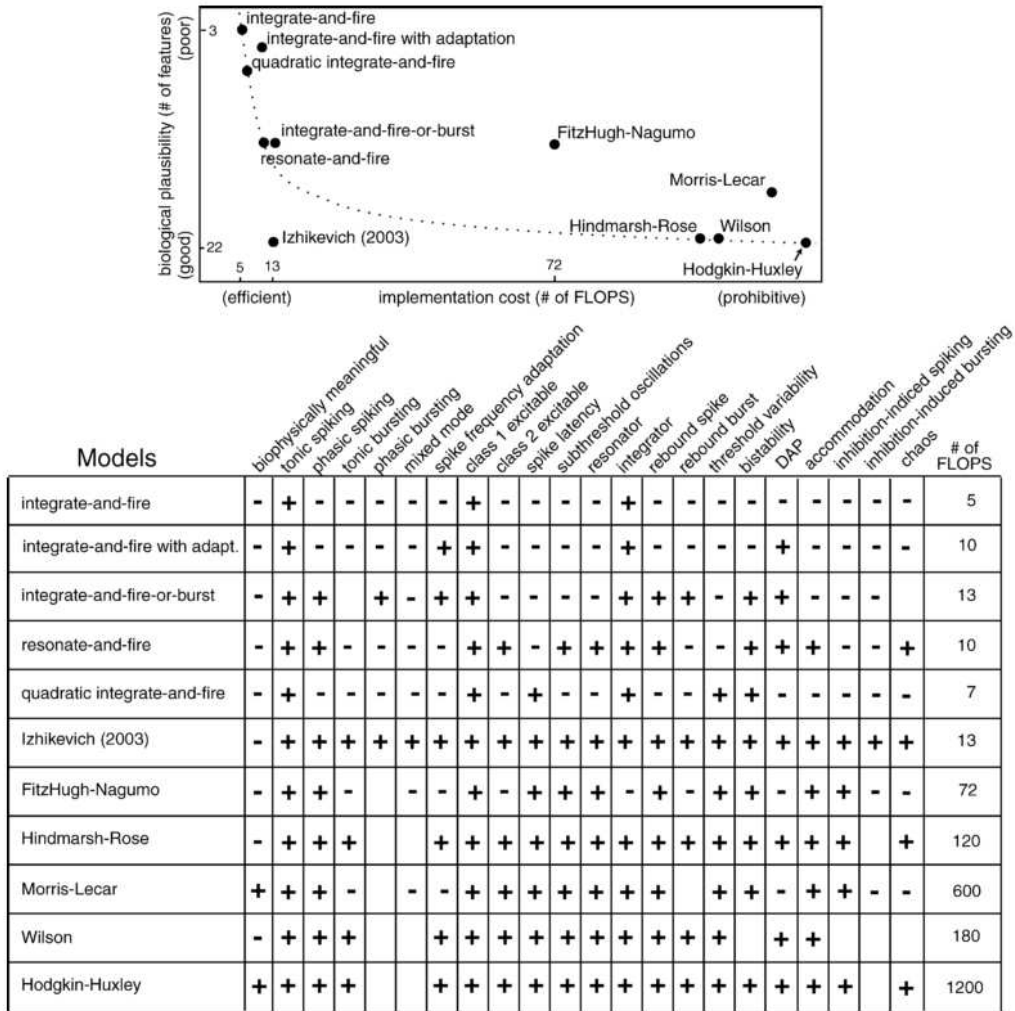


Figure 1.3: Comparing biological plausibility and implementation cost among different neuron models. Figure extracted from Izhikevich’s paper [53].

minimal ingredients specific dynamical features of real neurons. In particular, these simplified model are useful in analytical studies and large-scale computations.

The choice of the best model depends on the questions one is interested to answer. This choice is also restricted by the available computational power. Izhikevich tried to answer this question and to show why his own model is useful in a paper entitled “Which model to use for cortical spiking neurons?” [53]. In his work, he showed a detailed comparison of the neuro-computational properties of spiking and bursting models. The main results are summarized in Fig. 1.3. Along this Thesis we use conductance-based model such as HH and also simplified models, for example, the Izhikevich [51], Morris-Lecar [54] and Integrate-and-Fire [55] models. Each employed model is described in detail when necessary.

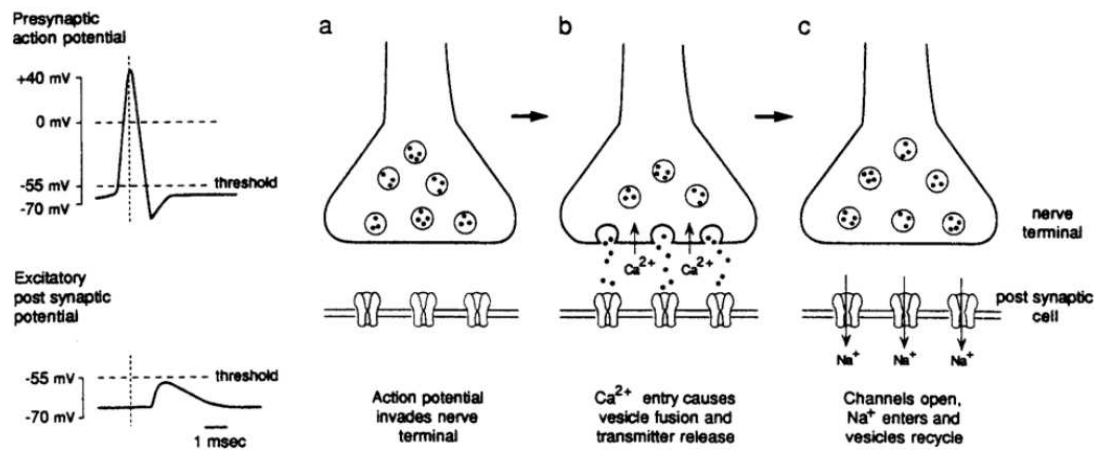


Figure 1.4: Standard model of chemical synaptic transmission [54]. (a) A presynaptic action potential propagates down the axon and reaches the nerve terminal. (b) Depolarization of the nerve terminal activates voltage-gated  $\text{Ca}^{2+}$  channels in the presynaptic membrane. The increasing of the intracellular concentration of  $\text{Ca}^{2+}$  promotes the neurotransmitter release. (c) The neurotransmitters in the synaptic cleft activate ligand-gated ion channels on the postsynaptic membrane, permitting the entry of the specific ions ( $\text{Na}^+$  in this example) and leading to an excitatory postsynaptic potential. Reproduced from Jessell and Kandel [56].

## 1.2.2 Chemical synapses

Spikes are generally not directly transmitted between neurons. Communication between neurons requires the exchange of electrical or chemical signals. These connections, called synapses, are the dynamical links of our neuronal networks. Depending on the transmission mechanisms, they can be divided into chemical or electrical synapses. In electrical synapses the membranes of the two communicating neurons come extremely close at the synapse and are actually linked together by an intercellular specialization called a gap junction [57]. In chemical synapses, the electrical activity in the presynaptic neuron induces (via the activation of voltage-gated calcium channels) the release of neurotransmitters that bind to receptors located in the postsynaptic cell. The neurotransmitter may initiate an electrical response (postsynaptic potential) or a secondary messenger pathway that may either excite or inhibit the postsynaptic neuron (see Fig. 1.4). Here we will use mainly chemical synapses.

In the brain, synaptic transmission is usually mediated by excitatory (depolarize) and inhibitory (hyperpolarize) amino acid neurotransmitters, glutamate and GABA, respectively. Glutamate activates AMPA/kainate receptors associated to fast transmission, and NMDA receptors associated to slow transmission and synaptic plasticity. It is worth mentioning that there is a plethora of physiological subtypes within a given receptor class. In addition, its properties are known to vary depending on the particular subunits that make a receptor. Typically an excitatory (inhibitory) synaptic current facilitates (hampers) the firing of the postsynaptic neuron. Moreover, one specific neuron can only excite or inhibit the others, not both. Hence, neurons can also be labeled as excitatory or inhibitory neurons [58].

The macroscopic behavior of synaptic currents can be described by kinetic models. It means the synaptic current is described by Ohm's law:

$$I^{(i)} = g_i r^{(i)} (V - E_i), \quad (1.6)$$

where  $V$  is the postsynaptic potential,  $g_i$  the maximal conductance,  $E_i$  the reversal potential, and the fraction  $r^{(i)}$  ( $i = \text{AMPA, NMDA, GABA}_A, \text{GABA}_B$ ) of bound synaptic receptors is modeled by a first-order kinetic dynamics:

$$\frac{dr^{(i)}}{dt} = \alpha_i [T] (1 - r^{(i)}) - \beta_i r^{(i)}. \quad (1.7)$$

$[T]$  is the neurotransmitter concentration in the synaptic cleft and the values of the rate constants  $\alpha_A$ ,  $\beta_A$ ,  $\alpha_G$ , and  $\beta_G$  are known to depend on a number of different factors and vary significantly [59, 60, 61]. Simple kinetic models may not adequately simulate the fine details of synaptic currents, but they provide a good approximation to some features such as rise, decay, voltage dependence and summation of currents. They are useful for describing general behavior of small microcircuits. Also important, they maintain computational efficiency in simulations of larger neuronal networks.

### 1.2.3 Neuronal populations

Neuronal networks exhibit complex spatial and temporal patterns even in the absence of external input. Specific cognitive tasks require the activation of different brain regions and patterns. Therefore, neuronal population models should encompass two main aspects. First, capture the large-scale interareal behavior at multiple temporal scales as well as neuronal scale features. Second, relate the activity patterns during different situations to the underlying anatomical connectivity of the brain.

In a neuronal population model we know the structural connectivity (i.e. anatomical) and we can explore the functional and effective connectivity (related to correlation and direction of the information flux respectively) under distinct constraints [62]. This can provide useful insights to the reversal problem. Typically we can extract functional and effective relations between distinct brain regions from experimental data, but we do not know the anatomical connectivity.

Usually, biophysically plausible populations models are networks of spiking neurons models linked via chemical synapses. Cortical-like models typically consider the proportion of excitatory and inhibitory neurons as 80% to 20% in the cortex and sparse connectivity between neurons [45]. In addition, experimental data suggest that cortical regions exhibit small-worlds properties, which is hypothesized to promote economy and efficiency during the information transmission. Nevertheless, several studies propose different topologies to brain networks, such as randomly, hierarchical, all-to-all connections, or a mixture of them.

### 1.2.4 Synchronization in the brain

It is widely recognized that the brain's ability to generate and sense temporal information is a prerequisite for both action and cognition. Synchronous rhythms represent a core mechanism

for temporal coordination of neuronal activity. In the last decades, theoretical and experimental studies have made significant advances to comprehend the cellular and circuit basis of these oscillations [63]. A major breakthrough was the realization that synaptic inhibition plays a fundamental role in the rhythmogenesis. It is important to note that neuronal correlation implies synchronization in some time scale, which can occur with or without oscillations. However, abnormal neural synchronization is tightly related to mental disorders like schizophrenia and autism [64]. Altogether, it is not well known if synchronization emerges as an epiphenomenon or what is its functional significance.

How information from distinct neuronal regions is exchanged is a major question underlying the binding problem. In other words, how objects, colors, sounds, background and abstract or emotional features are combined into a single experience? In the absence of a coordinating center, the binding by synchrony hypothesis [65] was spread (but not completely accepted) within the scientific community. It suggests that synchronization works as a coordinator to select and route signals and bind together spatially segregated regions.

More recently, another hypothesis gained several endorsers, the communication-through-coherence [66]. Fries proposed that activated neuronal oscillation and rhythmic excitability fluctuations produce temporal windows for communication. Only coherently oscillating neuronal groups can interact effectively, because their communication windows for input and for output are open at the same times. Thus, a flexible pattern of coherence defines a flexible communication structure, which subserves our cognitive flexibility.

### 1.3 Experimental considerations

In neuroscience, electrophysiology is the study of the electrical properties of neurons and tissues. It involves measurements of voltage changes and electric currents on a wide variety of scales, from single ion channel proteins to large-scale electric signals in the nervous system. Intracellular recording involves measuring voltage and/or current across the neuronal membrane, whereas extracellular field potentials recordings are related to local current sinks or sources that are generated by the collective activity of many cells. We describe below some techniques that could facilitate the investigation of anticipated synchronization in neuronal networks.

Dynamic clamp is an electrophysiological method that uses a real-time interface between one or several living cells and a computer to simulate dynamic processes such as membrane potential or synaptic currents. Each living cell is impaled by one or more sharp or patch micropipette electrodes and its membrane potential is amplified and fed into the dynamic clamp machine. The dynamic clamp system contains a model of the membrane or synaptic conductance to be inserted in the living cells. It computes the currents generated by the modeled conductances and outputs it in real-time. That current is injected into the living cell, which therefore receives the same current as if it contained the membrane or synaptic conductance modeled with the dynamic clamp [67]. A hybrid patch clamp setup [68], similar to this, is described in Chapter 2 in a proposed experiment to investigate AS between a master and a slave neuron in the presence of an inhibitory feedback loop.

The hypothesis that neural assemblies form the basic functional unit of operation of the mammalian central nervous system was originally proposed by Donald Hebb [69] more than



60 years ago. Since then, several neurophysiologists have attempted to design electrophysiological methods capable of testing the principles governing the operation of dynamic distributed neural systems. In this sense, the development of multi-electrode recordings was the major breakthrough in the field. In particular, the local field potential (LFP) refers to the electric potential in the extracellular space around neurons, which can be recorded using multi-electrode arrays. It consists in an invasive technique, recorded in depth from within the cortical tissue or other deep brain structures, in alert or anesthetized subjects. Since LFPs are generated by synchronized synaptic currents arising on cortical neurons, they represent one of the best type of signals to investigate time differences between synchronized cortical regions. In fact, in Chapter 5, we propose that some counter intuitive phenomena reported in LFP data [70, 71] are evidences of anticipated synchronization in the cortex.

Less direct observations of electrical brain activity involve the recording of electromagnetic potentials generated by combined electrical currents of large neuronal populations. Electroencephalography (EEG) and magnetoencephalography (MEG) techniques are noninvasive recordings, made through groups of sensors placed on, or near, the surface of the head. EEG and MEG directly record signals generated directly from neuronal activity and consequently have a high temporal resolution. Although the spatial resolution is poor compared to the LFP, intracellular recordings from cortical neurons exhibit a close correspondence between EEG/LFP activity and synaptic potentials [72]. Therefore, we expect that the existence of AS in the brain can also be verified through EEG measures. Indeed this would open new possibilities in the study of AS in humans.

Since AS has not been reported in any biological system and in particular in any neuronal systems, we investigate the existence of AS in several biophysically inspired models that could be potentially tested. Our main concern was to employ biologically plausible features in order to be able to propose experimental setups in which AS could be verified. We investigated AS in two scales: neuronal level and large-scale populations. Firstly, intracellular recordings such as dynamic clamp, which allows the measure of spike timing of connected single cells, could be useful to verify the results presented in Chapter 2 and 3 for neuronal microcircuits. Secondly, multi-electrode arrays recordings provide data that can be compared to the results of neuronal populations model described in Chapter 4. Therefore, in Chapter 5 we analyze cortical data from LFP recordings and compare them to our models. Finally, in Chapter 6 we show results of spike-timing dependent plasticity in neuronal networks which exhibits AS that could be experimentally tested in both neuronal and populational scales.



## Anticipated synchronization in microcircuits

Small networks that can be represented by low dimensional systems have attracted a lot of attention from neuroscientists along decades. Synchronization properties of a few coupled neurons have been exhaustively studied analytically, numerically and experimentally. Despite the abundant literature on synchronization of neuronal motifs, the first attempt to find anticipated synchronization in a biologically plausible model [39] which can be experimentally tested is, as far as we know, the one we describe in this chapter. Since neuron models are good candidates to represent the master and slave systems, AS means that the slave (postsynaptic) neuron could fire a spike right before the master (presynaptic) neuron does [33]. However, the delayed self-feedback on the slave, suggested by Voss to attain AS, is unrealistic in neuronal circuitry. Therefore, we propose to bridge this gap by replacing the delayed self-feedback term by an inhibitory feedback loop mediated by chemical synapses and an interneuron [39].

### 2.1 Master-Slave-Interneuron: the 3-neuron motif

We start by mimicking the original master-slave circuit (described by eqs. (1.1)) with a unidirectional excitatory chemical synapse ( $M \rightarrow S$  in Fig. 2.1(a)). In a scenario with standard biophysical models, the inhibitory feedback we propose is given by an interneuron (I) driven by the slave neuron, which projects back an inhibitory chemical synapse to the slave neuron (see Fig. 2.1(a)). So the time-delayed negative feedback is accounted for by a chemical inhibition which impinges on the slave neuron some time after it has spiked, simply because synapses have characteristic time scales. Such inhibitory feedback loop is one of the most canonical neuronal microcircuits found in the nervous system, as for instance, in the spinal cord [42], cortex [42], thalamus [43, 44] and nuclei involved with song production in the bird brain [73]. For simplicity, we will henceforth refer to the 3-neuron motif [40, 41] of Fig. 2.1(a) as a Master-Slave-Interneuron (MSI) system.

As we will show below, whether or not the MSI circuit can exhibit AS depends, among other factors, on the excitability of the three neurons. In the MSI, this is controlled by a constant applied current (see section 2.1). To test the robustness of the results (and at the same time improve the realism and complexity of the model), in section 2.4 we study the four-neuron motif depicted in Fig. 2.1(b), where the excitability of the MSI network is chemically modulated via synapses projected from a global driver ( $D$ ). From now on, we refer to the 4-neuron motif as a Driver-Master-Slave-Interneuron (DMSI) microcircuit.

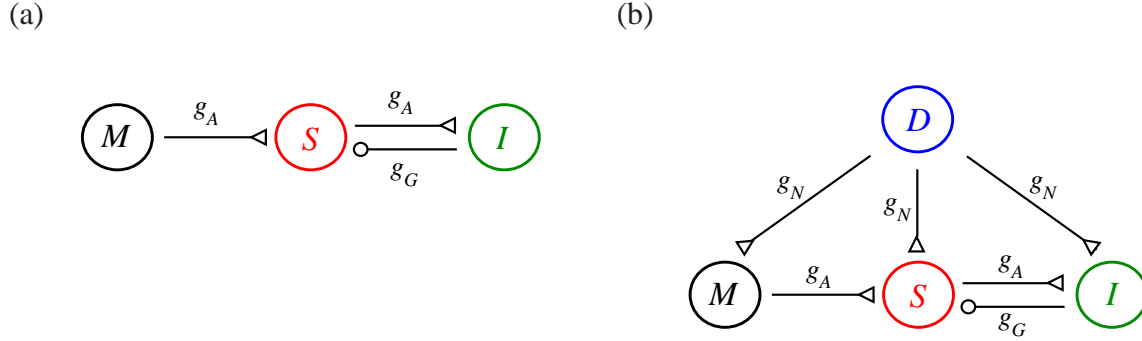


Figure 2.1: (a) Three neurons coupled by chemical synapses in the master-slave-interneuron (MSI) configuration : excitatory AMPA synapses (with maximal conductance  $g_A$ ) couple master (M) to slave (S) and slave to interneuron (I), whereas an inhibitory GABA<sub>A</sub> synapse (with maximal conductance  $g_G$ ) couples interneuron to slave. (b) Same as (a), except that all three neurons of the MSI circuit receive excitatory (NMDA) synapses from a driver neuron (D).

### 2.1.1 Neuron model

In the above networks, each node is described by a Hodgkin-Huxley (HH) model neuron [46], consisting of four coupled ordinary differential equations associated to the membrane potential  $V$  and the ionic currents flowing across the axonal membrane corresponding to the Na<sup>+</sup>, K<sup>+</sup> and leakage currents. The gating variables for sodium are  $h$  and  $m$  and for the potassium is  $n$ . The equations read [54]:

$$C_m \frac{dV}{dt} = \bar{G}_{Na} m^3 h (E_{Na} - V) + \bar{G}_K n^4 (E_K - V) + G_m (V_{rest} - V) + I + \sum I_{syn} \quad (2.1)$$

$$\frac{dx}{dt} = \alpha_x(V)(1-x) - \beta_x(V)x, \quad (2.2)$$

where  $x \in \{h, m, n\}$ ,  $C_m = 9\pi \mu\text{F}$  is the membrane capacitance of a  $30 \times 30 \times \pi \mu\text{m}^2$  equipotential patch of membrane [54],  $I$  is a constant current which sets the neuron excitability and  $\sum I_{syn}$  accounts for the interaction with other neurons. The reversal potentials are  $E_{Na} = 115 \text{ mV}$ ,  $E_K = -12 \text{ mV}$  and  $V_{rest} = 10.6 \text{ mV}$ , which correspond to maximal conductances  $\bar{G}_{Na} = 1080\pi \text{ mS}$ ,  $\bar{G}_K = 324\pi \text{ mS}$  and  $G_m = 2.7\pi \text{ mS}$ , respectively. The voltage dependent activation and inacti-

vation rates in the Hodgkin-Huxley model have the form:

$$\alpha_n(V) = \frac{10 - V}{100(e^{(10-V)/10} - 1)}, \quad (2.3)$$

$$\beta_n(V) = 0.125e^{-V/80}, \quad (2.4)$$

$$\alpha_m(V) = \frac{25 - V}{10(e^{(25-V)/10} - 1)}, \quad (2.5)$$

$$\beta_m(V) = 4e^{-V/18}, \quad (2.6)$$

$$\alpha_h(V) = 0.07e^{-V/20}, \quad (2.7)$$

$$\beta_h(V) = \frac{1}{(e^{(30-V)/10} + 1)}. \quad (2.8)$$

Note that all voltages are expressed relative to the resting potential of the model at  $I = 0$  [54].

According to Rinzel and Miller [74], in the absence of synaptic currents the only attractor of the system of equations 2.1-2.8 for  $I \lesssim 177.13$  pA is a stable fixed point, which loses stability via a subcritical Hopf bifurcation at  $I \simeq 276.51$  pA. For  $177.13$  pA  $\lesssim I \lesssim 276.51$  pA, the stable fixed point coexists with a stable limit cycle.

### 2.1.2 Synaptic coupling

AMPA (A) and GABA<sub>A</sub> (G) are the fast excitatory and inhibitory synapses in our model [see Fig. 2.1(a)]. Following Destexhe et al [58], the fraction  $r^{(i)}$  ( $i = A, G$ ) of bound (i.e. open) synaptic receptors is modeled by a first-order kinetic dynamics:

$$\frac{dr^{(i)}}{dt} = \alpha_i[T](1 - r^{(i)}) - \beta_i r^{(i)}, \quad (2.9)$$

where  $\alpha_i$  and  $\beta_i$  are rate constants and  $[T]$  is the neurotransmitter concentration in the synaptic cleft. For simplicity, we assume  $[T]$  to be an instantaneous function of the presynaptic potential  $V_{pre}$ :

$$[T](V_{pre}) = \frac{T_{max}}{1 + e^{[-(V_{pre} - V_p)/K_p]}}, \quad (2.10)$$

where  $T_{max} = 1$  mM<sup>-1</sup> is the maximal value of  $[T]$ ,  $K_p = 5$  mV gives the steepness of the sigmoid and  $V_p = 62$  mV sets the value at which the function is half-activated [58].

The synaptic current at each synapse is given by

$$I^{(i)} = g_i r^{(i)} (V - E_i), \quad (2.11)$$

where  $V$  is the postsynaptic potential,  $g_i$  the maximal conductance and  $E_i$  the reversal potential. We use  $E_A = 60$  mV and  $E_G = -20$  mV.

The values of the rate constants  $\alpha_A$ ,  $\beta_A$ ,  $\alpha_G$ , and  $\beta_G$  are known to depend on a number of different factors and significantly vary [59, 60, 61]. To exemplify some of our results, we initially fix some parameters, which are set to the values of Table 2.1 unless otherwise stated (section 2.2). Then we allow these parameters (as well as the synaptic conductances) to vary

	<i>MSI</i>	<i>DMSI</i>
$\alpha_A$ (mM <sup>-1</sup> ms <sup>-1</sup> )	1.1	1.1
$\beta_A$ (ms <sup>-1</sup> )	0.19	0.19
$\alpha_G$ (mM <sup>-1</sup> ms <sup>-1</sup> )	5.0	5.0
$\beta_G$ (ms <sup>-1</sup> )	0.30	0.60
$\alpha_N$ (mM <sup>-1</sup> ms <sup>-1</sup> )	—	0.072
$\beta_N$ (ms <sup>-1</sup> )	—	0.0066
$g_A$ (nS)	10	10
$I$ (pA)	280	160

Table 2.1: Standard values employed in the model. See text for details.

within physiological range when exploring different synchronization regimes (see sections 2.3 and 2.4).

The slow excitatory synapse is NMDA (N) and its synaptic current is given by:

$$I^{(N)} = g_N B(V) r^{(N)} (V - E_N), \quad (2.12)$$

where  $E_N = 60$  mV. The dynamics of the variable  $r^{(N)}$  is similar to eq. (2.9) with  $\alpha_N = 0.072$  mM<sup>-1</sup>ms<sup>-1</sup> and  $\beta_N = 0.0066$  ms<sup>-1</sup>. The magnesium block of the NMDA receptor channel can be modeled as a function of postsynaptic voltage  $V$ :

$$B(V) = \frac{1}{1 + e^{(-0.062V)[\text{Mg}^{2+}]_o/3.57}}, \quad (2.13)$$

where  $[\text{Mg}^{2+}]_o = 1$  mM is the physiological extracellular magnesium concentration.

In what follows, we will drop the neurotransmitter superscripts  $A$ ,  $G$  and  $N$  from the synaptic variables  $r$  and  $I$ . Instead we use double subscripts to denote the referred pre- and postsynaptic neurons. For instance, the synaptic current in the slave neuron due to the interneuron (the only inhibitory synapse in our models) will be denoted as  $I_{IS}$ , and so forth.

## 2.2 Three dynamical regimes

### 2.2.1 Phase-locking: delayed and anticipated synchronization

Initially, we describe results for the scenario where all neurons receive a constant current  $I \geq 280$  pA. This corresponds to a situation in which the fixed points are unstable and, when isolated, all neurons spike periodically. All other parameters are as in Table 2.1. For different sets of the inhibitory conductance  $g_G$  our system can exhibit three different behaviors. To characterize them, we define  $t_i^M$  as the time the membrane potential of the master neuron is at its maximum value in the  $i$ -th cycle (i.e. its  $i$ -th spike time), and  $t_i^S$  as the spike time of the slave neuron which is nearest to  $t_i^M$ .

The delay  $\tau_i$  is defined as the difference (see Fig. 2.2):

$$\tau_i \equiv t_i^S - t_i^M. \quad (2.14)$$

Initial conditions were randomly chosen for each computed time series. When  $\tau_i$  converges to a constant value  $\tau$ , a phase-locked regime is reached [75]. If  $\tau > 0$  (“master neuron spikes first”) we say that the system exhibits delayed synchronization (DS) [Fig. 2.2(a)]. If  $\tau < 0$  (“slave neuron spikes first”), we say that anticipated synchronization (AS) occurs [Fig. 2.2(b)]. If  $\tau$  does not converge to a fixed value, the system is in a phase drift (PD) regime [75]. The extent to which the AS regime can be legitimately considered “anticipated” in a periodic system will be discussed below.

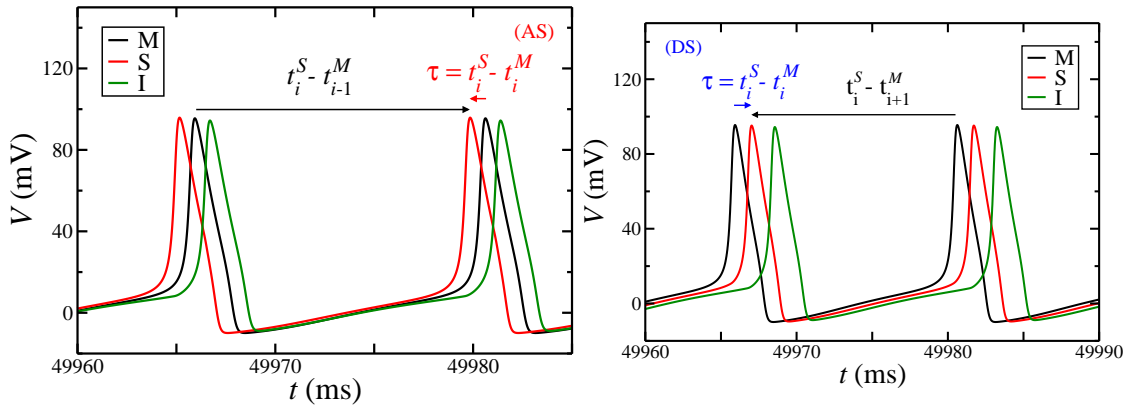


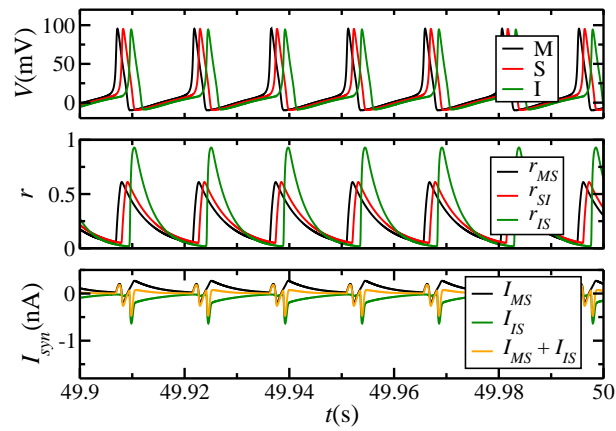
Figure 2.2: Membrane potential  $V$  as a function of time for an external current  $I = 280$  pA in the master (M), slave (S), and interneuron (I) neurons. The plot illustrates two regimes: (a)  $g_G = 20$  nS leads to delayed synchronization (DS), where  $\tau > 0$ , and (b)  $g_G = 40$  nS leads to anticipated synchronization (AS), where  $\tau < 0$ . Other parameters as in Table 2.1.

In Figure 2.3 we show examples of time series in the three different regimes (DS, AS and PD). The different panels correspond to the membrane potential, fraction of activated receptors for each synapse, and synaptic current in the slave neuron. For a relatively small value of the inhibitory coupling [ $g_G = 20$  nS, Fig. 2.3(a)] the slave neuron lags behind the master, characterizing DS. In Fig. 2.3(b), we observe that by increasing the value of the inhibitory coupling ( $g_G = 40$  nS) we reach an AS regime. Finally, for strong enough inhibition [ $g_G = 60$  nS, Fig. 2.3(c)] the PD regime ensues.

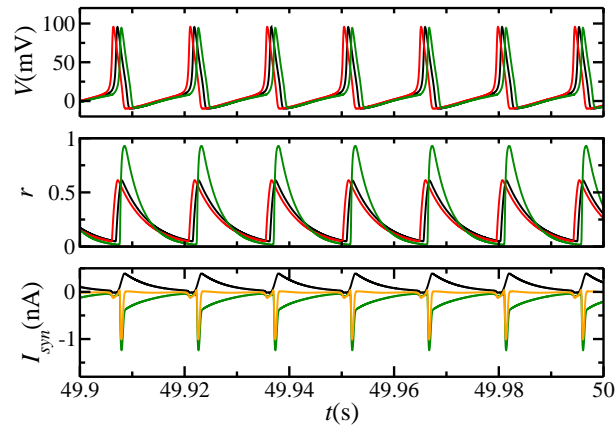
### 2.2.2 Phase-drift

In the DS and AS regimes the master and slave neurons spike at the same frequency. However, when the system reaches the PD regime the mean firing rate of the slave neuron becomes higher than that of the master. The counterintuitive result shown in Fig. 2.4(a) emerges: the mean firing rate of the slave neuron *increases* while increasing the conductance of the *inhibitory* synapse projected from the interneuron. For the particular combination of parameters used in Fig. 2.4(a), the transition turns out to be reentrant, i.e., the system returns to the DS regime for sufficiently strong inhibition (a more detailed exploration of parameter space will be pre-

(a) DS



(b) AS



(c) PD

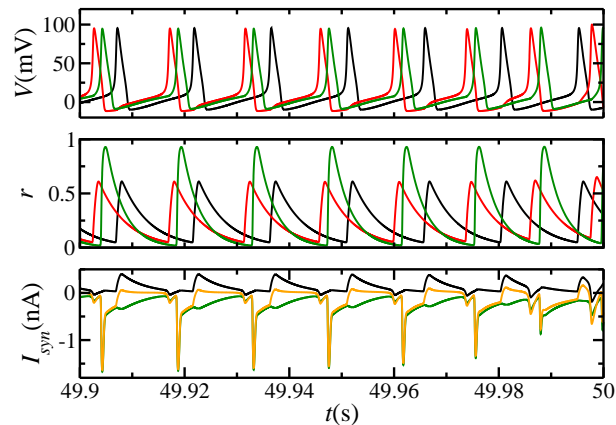


Figure 2.3: Time series of the membrane potentials ( $V$ ), bound receptors ( $r$ ) and synaptic currents ( $I$ ), with model parameters as in Table 2.1 for the MSI motif. Note that the system is periodic in the DS and AS regimes [(a) and (b) respectively], but not in the PD regime (c).



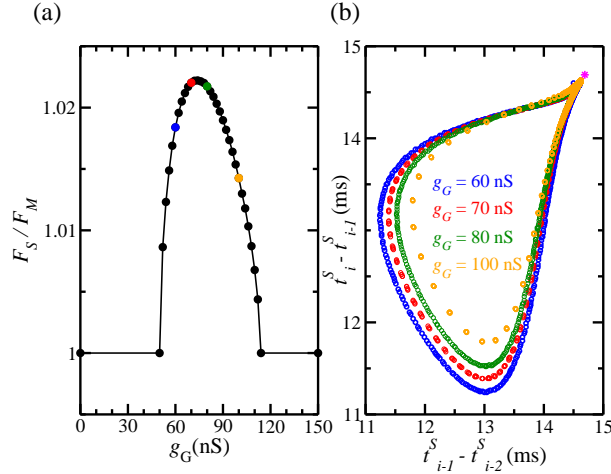


Figure 2.4: (a) The mean firing rate of the slave ( $F_S$ ) coincides with the mean firing rate of the master ( $F_M$ ) for DS and AS regimes, but it is larger for PD. (b) In PD, the return map of the interspike interval of the slave is consistent with a quasi-periodic system (the pink star shows the return map of the master).

sented below). Figure 2.4(b) shows the return map of the interspike interval (ISI) of the slave, which forms a closed curve (touching the trivial single-point return map of the master). This is consistent with a quasi-periodic phase-drift regime.

## 2.3 Scanning parameter space

Note that in this simple scenario  $g_G$  plays an analogous role to that of  $K$  in Eq. 1.1, for which AS is stable only when  $K > K_c$  (eventually with reentrances) [76]. Moreover, the behavior of the synaptic current in the slave neuron is particularly revealing: in the DS regime [Fig. 2.3(a)], it has a positive peak prior to the slave spike, which drives the firing in the slave neuron. In the AS regime [Fig. 2.3(b)], however, there is no significant resulting current, except when the slave neuron is already suprathreshold. In this case, the current has essentially no effect upon the slave dynamics. This situation is similar to the stable anticipated solution of Eq. 1.1, when the coupling term vanishes.

The dependence of the time delay  $\tau$  on  $g_G$  is shown in Fig. 2.5 for different values of the external current  $I$  and maximal excitatory conductance  $g_A$ . Several features in those curves are worth emphasizing. First, unlike previous studies on AS, where the anticipation time was hardwired via the delay parameter  $t_d$  [see eq.(1.1)], in our case the anticipation time  $\tau$  is a result of the dynamics. Note that  $g_G$  (the parameter varied in Fig. 2.5) does not change the time scales of the synaptic dynamical variables ( $r$ ), only the synaptic strength.

Secondly,  $\tau$  varies smoothly with  $g_G$ . This continuity somehow allows us to interpret  $\tau < 0$  as a legitimately anticipated regime. The reasoning is as follows. For  $g_G = 0$ , we simply have a master-slave configuration in which the two neurons spike periodically. Due to the excitatory coupling, the slave's spike is always closer to the master's spike which precedes it than to the

master's spike which succeeds it [as in e.g. Fig. (2.2)(a)]. Moreover, the time difference is approximately 1.5 ms, which is comparable to the characteristic times of the synapse. In that case, despite the formal ambiguity implicit in the periodicity of the time series, the dynamical regime is usually understood as “delayed synchronization”. We interpret it in the following sense: the system is phase-locked at a phase difference with a well defined sign [75]. Increasing  $g_G$ , the time difference between the master's and the slave's spikes eventually changes sign [as in e.g. Fig. (2.2)(b)]. Even though the ambiguity in principle remains, there is no reason why we should not call this regime “anticipated synchronization” (again a phase-locked regime, but with a phase difference of opposite sign). In fact, we have not found any parameter change which would take the model from the situation in Fig. (2.2)(a) to that of Fig. (2.2)(b) by gradually *increasing* the lag of the slave spike until it approached the next master spike. If that ever happened,  $\tau$  would change discontinuously (by its definition). Therefore, the term “anticipated synchronization” by no means implies violation of causality and should just be interpreted with caution. As we will discuss later, the relative timing between pre- and postsynaptic neurons turns out to be extremely relevant for real neurons.

Third, it is interesting to note that the largest anticipation time can be longer (up to 3 ms, i.e. about 20% of the interspike interval) than the largest time for the delayed synchronization ( $\approx 1.5$  ms). If one increases  $g_G$  further in an attempt to obtain even larger values of  $\tau$ , however, the system undergoes a bifurcation to a regime with phase drift (which marks the end of the curves in Fig. 2.5).

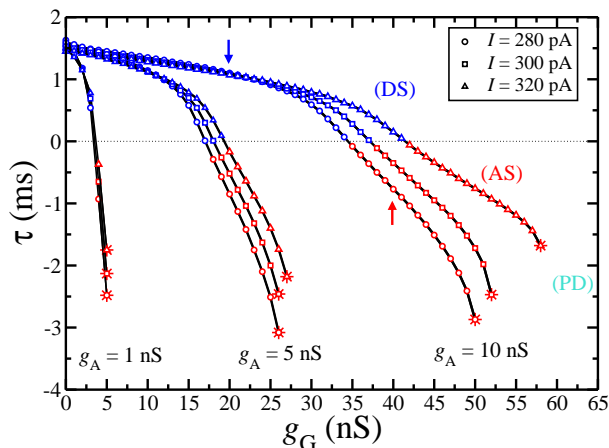


Figure 2.5: Dependence of the time delay  $\tau$  with the maximal conductance  $g_G$  for different values of the applied current  $I$  and  $g_A$ . The end of each curve (stars) marks the critical value of  $g_G$ , above which the system changes from AS to PD.

The number of parameters in our model is very large. The number of dynamical regimes which a system of coupled nonlinear oscillators can present is also very large. Notably  $p/q$ -subharmonic locking structured in Arnold tongues usually occur [77]. These occur in our model as well, but not in the parameter region we are considering. In this context, an attempt to map all the dynamical possibilities in parameter space would be extremely difficult and, most important, unproductive for our purposes. We therefore focus on addressing the main question of this work, which is whether or not AS can be stable in a biophysically plausible model.

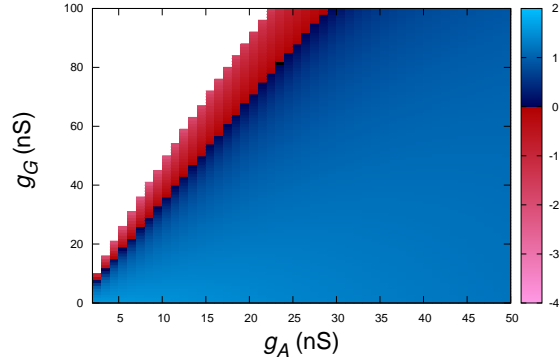


Figure 2.6: Time delay  $\tau$  (right bar) in the  $(g_A, g_G)$  projection of parameter space: DS (blue, right), AS (red, middle) and PD (white, left — meaning that no stationary value of  $\tau$  was found).

In Fig. 2.6 we display a two-dimensional projection of the phase diagram of our model. We employ the values in Table 2.1, except for  $g_A$ , which is varied along the horizontal axis. Note that each black curve with circles in Fig. 2.5 corresponds to a different vertical cut of Fig. 2.6, along which  $g_G$  changes. We observe that the three different regimes are distributed in large continuous regions, having a clear transition between them. Moreover the transition from the DS to the AS phase can be well approximated by a linear relation  $g_G/g_A \approx 3.5$  in a large portion of the diagram.

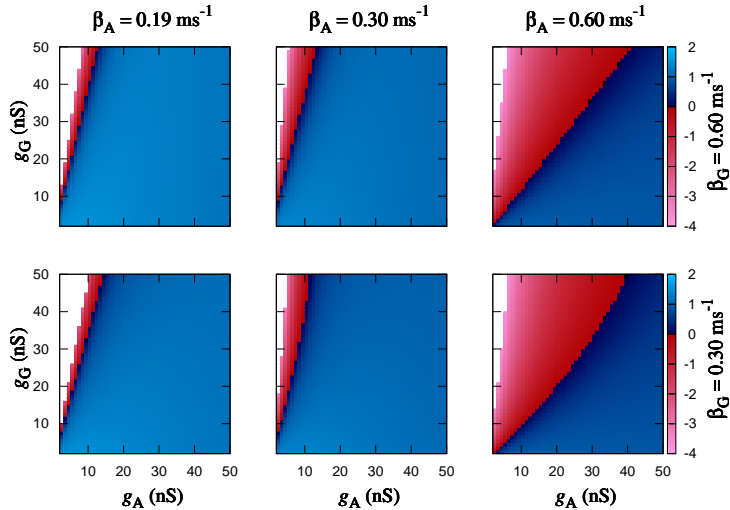


Figure 2.7: Time delay  $\tau$  (right bar) in the  $(g_A, g_G)$  projection of parameter space for different combinations of  $\beta_A$  and  $\beta_G$ . From left to right we have respectively PD, AS and DS regimes, as in Fig. 2.6.

Linearity, however, breaks down as parameters are further varied. This can be seen e.g. in Fig. 2.7, which displays the same projection as Fig. 2.6, but for different combinations of  $\beta_G$

and  $\beta_A$ . We observe that AS remains stable in a finite region of the parameter space, and this region increases as excitatory synapses become faster.

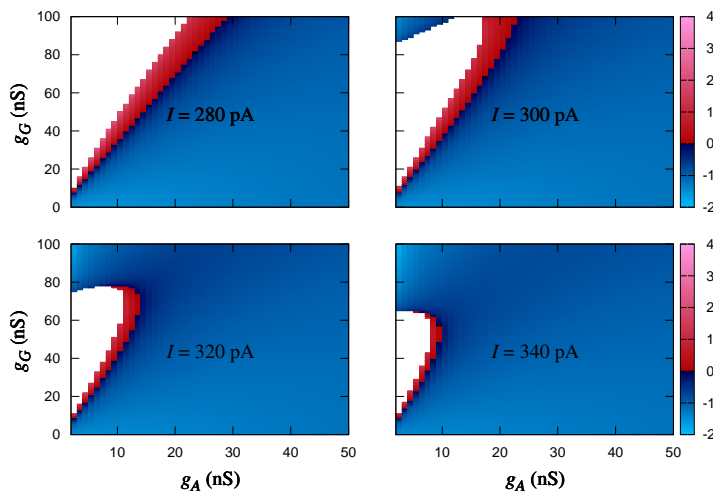


Figure 2.8: Time delay  $\tau$  (right bar) in the  $(g_A, g_G)$  projection of parameter space for different values of  $I$ . PD, AS and DS regimes as in Fig. 2.6.

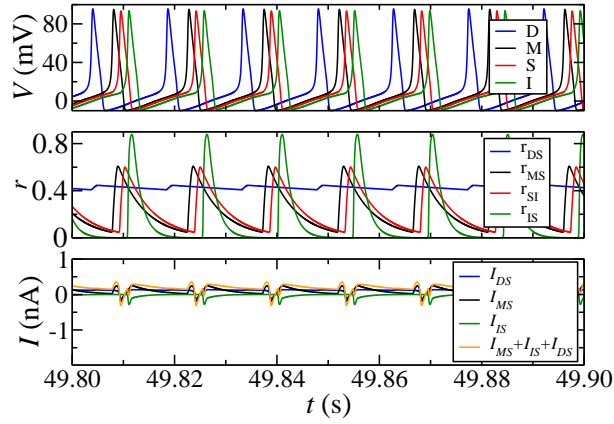
Figure 2.5 suggests that larger values of the input current  $I$  eventually lead to a transition from AS to DS. This effect is better depicted in Fig. 2.8, where the DS region increases in size as  $I$  (and therefore the firing rate) increases. Figures 2.8(b)-(d) also show that the system can exhibit reentrant transitions as  $g_G$  is varied. Most importantly, however, it can be seen in Figs. 2.7 and 2.8 that there is always an AS region in parameter space, as synaptic and intrinsic parameters are varied.

As we will discuss later, the possibility of controlling the transition between AS and DS is in principle extremely appealing to the study of plasticity in neuroscience. However, in a biological network, the input current would not be exactly constant, but rather be modulated by other neurons. In the following, we test the robustness of AS in this more involved scenario, therefore moving one step ahead in biological plausibility.

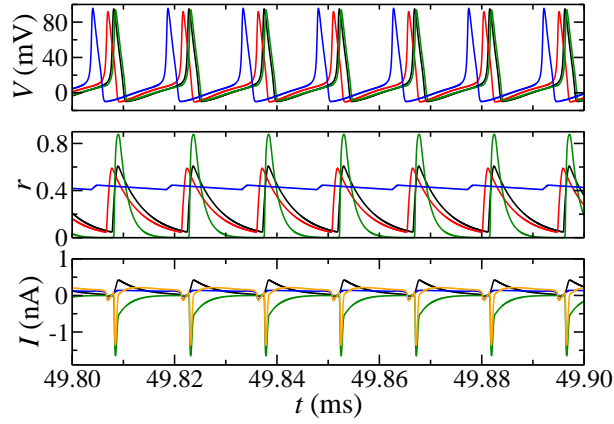
## 2.4 The effect of a common Driver

Let us consider the MSI circuit under a constant input current  $I = 160$  pA. This is below the Hopf bifurcation [74], i.e. none of the three neurons spikes tonically. Their activity will now be controlled by the driver neuron (D), which projects excitatory synapses onto the MSI circuit [see Fig. 2.1(b)]. We chose to replace the constant input current by a slowly varying current, so that the synapses projecting from the driver neuron are of the NMDA type. The driver neuron receives a current  $I_D = 280$  pA, so it spikes tonically. All remaining parameters are as in the second column of Table 2.1. The interest in this case is to verify whether AS holds when the excitability of the MSI circuit is modulated by a non-stationary current.

(a) DS



(b) AS



(c) PD

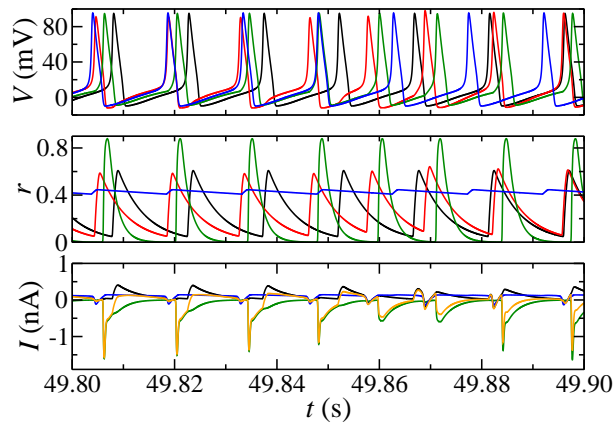


Figure 2.9: Time series of the membrane potentials ( $V$ ), bound receptors ( $r$ ) and synaptic currents ( $I$ ), with model parameters as in Table 2.1 for DMSI. All the excitatory synaptic conductances are  $g_N = g_A = 10$  nS while the inhibitory conductance is (a)  $g_G = 10$  nS, (b)  $g_G = 60$  nS and (c)  $g_G = 80$  nS

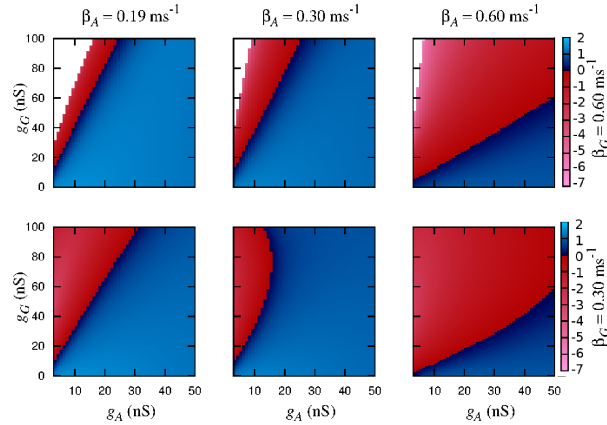


Figure 2.10: DMSI circuit (see Fig. 2.1(b)). Delay  $\tau$  (right bar) in the  $(g_A, g_G)$  projection of parameter space for different combinations of  $\beta_A$  and  $\beta_G$ . PD, AS and DS regimes as in Fig. 2.6.

As shown in Fig. 2.9 and 2.10, we found in this new scenario a similar route from DS to AS, and then the PD regime (compare with Fig. 2.3 and 2.7). Note that the characteristic time ( $\beta_N = 6.6 \text{ s}^{-1}$ ) for the unbinding of the NMDA receptors is about ten times larger than the interspike interval (ISI) of the driver neuron (which spikes at  $\approx 67 \text{ Hz}$ ). As a consequence,  $r_{DM}$ ,  $r_{DS}$ ,  $r_{DI}$  are kept at nearly constant values (with variations of  $\approx 10\%$  around a mean value see Fig. 2.9(b)). The variations in the NMDA synaptic current are also small, which in principle should make the system behave in an apparently similar way to the previous MSI circuit. However, these small variations are important enough to increase the AS domain in parameter space, in some cases even eliminating the PD region (see e.g. Fig. 2.10 for  $\beta_G = 0.30 \text{ ms}^{-1}$ ). Therefore, at least in this case, the use of more biological plausible parameters does not destroy AS, but rather enhances it.

In fact, the three regions in the MSI diagrams seem to retain their main features in the DMSI circuit. When PD occurs, for example, the slave again spikes faster than the master (see Fig. 2.11(a)), like in the MSI circuit (compare with Fig. 2.4(a)). Another signature of the robustness of the PD phase against the replacement of a constant by a slowly-varying synaptic current appears in the return map shown in Fig. 2.11(b). It can be seen that it has the same structure of its three-neuron counterpart shown in Fig. 2.4(b).

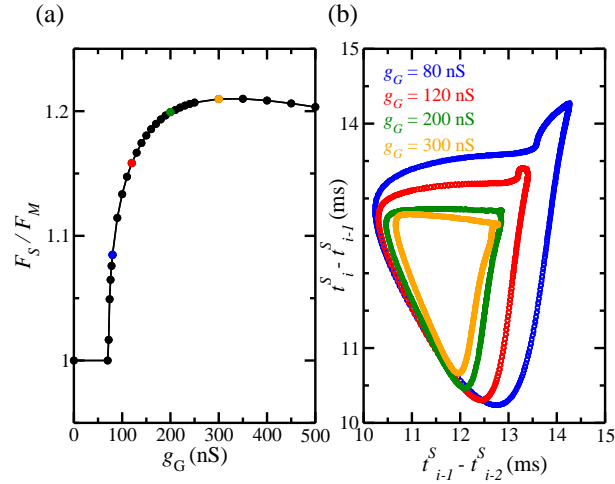


Figure 2.11: DMSI circuit (see Fig. 2.1(b)). (a) The mean firing rate of the slave ( $F_S$ ) coincides with the mean firing rate of the master ( $F_M$ ) for DS and AS regimes, but it is larger for PD. (b) In PD, the return map of the interspike interval of the slave is consistent with a quasi-periodic system.

## 2.5 Neuronal chain networks

The brain exhibits well defined sequences of neuronal processes during complex behaviors, such as cognitive tasks, motor sequences execution and recognition. One well known model that reproduces multiple observations of precisely repeating firing patterns is the synfire-chain [78, 79]. However, a lot of other networks can produce precise firing patterns and generate sequences. For example, the execution and recognition of actions can be achieved through the propagation of activity bursts along a biologically inspired neuronal chain [80], a chain network can propagate stable activity with temporal precision in songbirds [81] and a chain of chaotic slaves can exhibit AS [26].

We wondered if it is possible to control the temporal precision between spikes of different neurons in a chain of slaves and interneurons (see Fig. 2.12). Particularly, we are interested to know whether this chain can exhibit AS. It is shown in Fig. 2.13 that a chain of coupled standard HH neurons driven by a constant current can provide a mechanism for obtaining larger anticipation and delay times between the first master and the last slave than the 3-neuron motif. Furthermore, the chain network motif has precise time differences among the spikes that depend on the synaptic conductances and the external current.

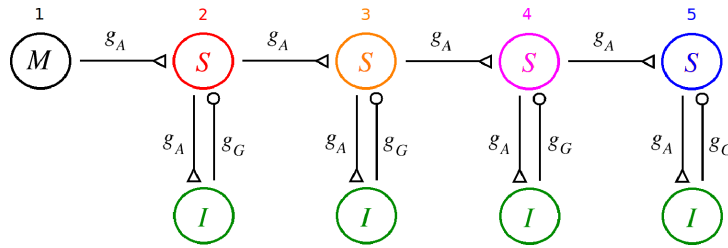


Figure 2.12: Chain of master (M), slaves (S) and interneurons (I). All parameters as in Table 2.1 for the MSI circuit.

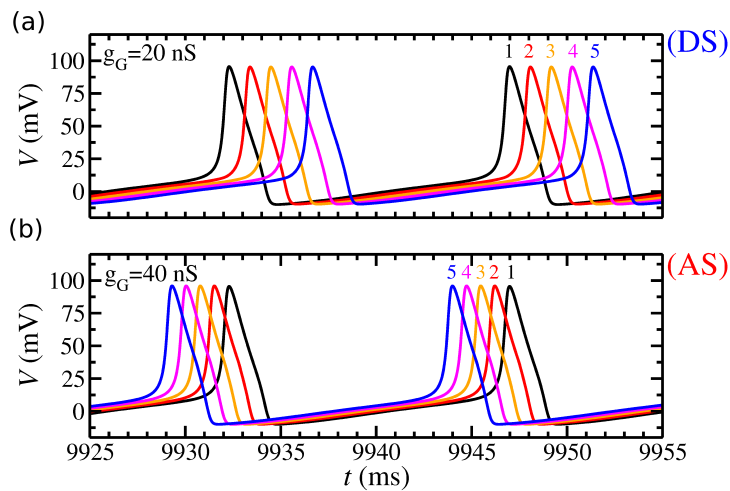


Figure 2.13: Membrane potential of each numbered neuron shown in Fig. 2.12. The chain exhibits (a) DS for weak inhibitory synaptic conductances  $g_{IS} = 20$  nS and (b) AS for stronger inhibition  $g_{IS} = 40$  nS. Note that the largest anticipation (and delay) time is between neurons 1 and 5.

## 2.6 Proposed experiment

### 2.6.1 The hybrid patch clamp setup

The 3-neuron motif shown in Fig. 2.1 can be experimentally reproduced in a hybrid patch clamp setup. It means that AS could be tested *in vitro*. The required setup consists in three steps. First, it is necessary to patch a real neuron (that would be our slave). Second, through a dynamic clamp procedure, one excitatory and one inhibitory synapses are generated (from simulated master and interneuron respectively). These generated synaptic currents are injected through the intracellular recording pipette. Finally, the simulated interneuron receives, in real-time, excitatory synapses that were generated by each spike of the slave.

Such setup has been used by Le Masson et al. [68] to study how an inhibitory feedback loop controls spike transfer in thalamic circuits. They have verified that, depending on the value of the inhibition, the slave and the interneuron exhibit coherent oscillations. This coherent behavior was characterized by a peak in the cross-correlation function, which is defined by



comparing the activity profiles of the two neurons across different time delays [82]. The peak in the cross-correlation is a measure of the level of synchrony between the two neurons, whereas the time delay in which the peak occurs is the time lag of the synchronized regime, i.e. the equivalent of  $\tau$  in our model.

Le Masson et al. [68] have reported that the positive correlation peak decreases for large inhibition. However, they have not verified any increase in the negative correlation between the master and the slave. One possibility for the absence of the AS regime is due to the fact that the simulated retina cell activity (master) and the patched thalamocortical neuron (slave) present very different dynamics.

We suggest that the AS regime could be verified in the hybrid setup if the simulated master cell have similar dynamical properties as the biological patched neuron. To test this hypothesis it is necessary to make our previous 3-neuron motif even more realistic. In this section, we use a single-compartment modified Hodgkin-Huxley neuron model designed according to Pospischil et al. [83] which is based on previous thalamocortical models [84, 85]. This model was obtained from ModelDB [86]. It is well suited for simulating motifs in which the effect of neuromodulators or pharmacological agents on identified conductances can be tested.

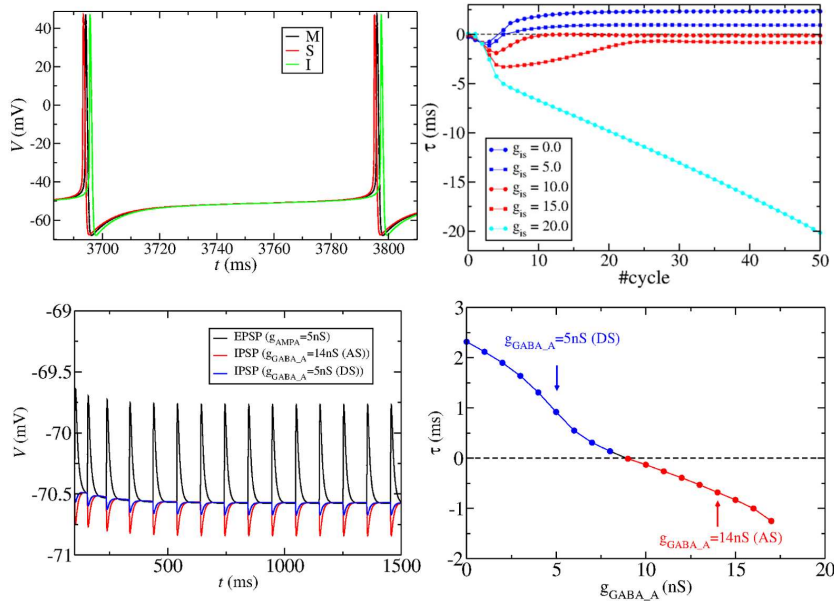


Figure 2.14: Characterizing the modified HH model. (a) Example of the membrane potential of each neuron in the AS regime. The spiking frequency is smaller than in the standard HH. (b) Excitatory and inhibitory post synaptic potential EPSP and IPSP generated by the AMPA and the  $GABA_A$  synapses employed in our model. (c) Time delay  $\tau_i$  in each cycle, characterizing DS (blue), AS (red) and PD (cyan) regimes. (d)  $\tau$  as a function of  $g_G$ . Similar to what happens in the standard HH, here there is a smooth and continuous transition from DS to AS.

### 2.6.2 Modified Hodgkin-Huxley model

Each neuron is now described by:

$$C_m \frac{dV}{dt} = \bar{G}_{Na} m^3 h (E_{Na} - V) + \bar{G}_K n^4 (E_K - V) + \bar{G}_M p^4 (E_K - V) + G_m (V_{rest} - V) + I + \sum I_{syn} \quad (2.15)$$

where  $G_{Na} = 50$  mS/cm<sup>2</sup>,  $G_K = 5$  mS/cm<sup>2</sup>,  $G_M = 0.07$  mS/cm<sup>2</sup>,  $G_m = 0.1$  mS/cm<sup>2</sup>,  $E_{Na} = 50$  mV,  $E_K = -100$  mV. The three voltage-dependent currents are the sodium and potassium currents that generate action potentials and the extra “delayed-rectifier”  $K+$  current (represented by the term  $\bar{G}_M p^4 (E_K - V)$  in Eq. 2.16). This slow  $K+$  current is responsible for spike-frequency adaptation firing rate and the afterhyperpolarization (AHP) of cortical pyramidal cells. The gating variables  $x = m, n, h$  are described as before:

$$\frac{dx}{dt} = \alpha_x(V)(1 - x) - \beta_x(V). \quad (2.16)$$

The steady-state activation and the time constant are, respectively, given by  $x_\infty = \alpha_x / (\alpha_x + \beta_x)$  and  $\tau_x = 1 / (\alpha_x + \beta_x)$ , where:

$$\begin{aligned} \alpha_m &= \frac{-0.32(V - V_T - 13)}{e^{-(V - V_T - 13)/4} - 1} \\ \beta_m &= \frac{0.28(V - V_T - 40)}{e^{(V - V_T - 40)/5} - 1} \\ \alpha_h &= 0.128 e^{-(V - V_T - 17)/18} \\ \beta_h &= \frac{4}{1 + e^{-(V - V_T - 40)/5}} \\ \alpha_n &= \frac{-0.032(V - V_T - 15)}{e^{-(V - V_T - 15)/5} - 1} \\ \beta_n &= 0.5 e^{-(V - V_T - 10)/40} - 1. \end{aligned} \quad (2.17)$$

We use  $V_T = 55$  mV.

The gating variable  $p$  obeys the following equations:

$$\begin{aligned} \frac{dp}{dt} &= (p_\infty(V) - p) / \tau_M(V) \\ p_\infty(V) &= \frac{1}{1 + e^{-(V+35)/10}} \\ \tau_M(V) &= \frac{\tau_{max}}{3.3 e^{(V+35)/20} + e^{-(V+35)/20}}, \end{aligned} \quad (2.18)$$

where  $\tau_{max} = 1$  s. We can also take into account the effect of temperature ( $T$  in Celsius) dividing  $\tau_{max}$  by  $2.3^{(T-36)/10}$ , but here we consider  $T = 36$  °C.

The model described by Eq. 2.16 can reproduce different electrophysiological results from the rat somatosensory cortex and thalamus *in vitro* [83]. It is also good to represent both

excitatory and inhibitory cortex cells (see an example of the mean membrane potential of M, S and I in Fig 2.14(a)). Depending on the parameters it fits different neuron types as regular spiking, fast spiking, low-threshold spikes. Adding two more currents to Eq. 2.16 (one for high and other for low threshold  $\text{Ca}^{2+}$ ) it can also generate bursts. By far the largest cell class in neocortex is the so-called regular-spiking (RS) neuron, which is in general excitatory and most often correlates with a spiny pyramidal-cell morphology. The typical response of RS cells to depolarizing current pulses are trains of spikes with adaptation.

The model claims to represent one of the many possible compromises between simplicity and biological realism. It is more complex than nonlinear integrate-and-fire models [87, 53, 88], but it is also more realistic because the ionic currents are identified and can be adjusted to physiological measurements such as voltage-clamp data if needed. In order to mimic real synapses it is also important to obtain realistic excitatory (inhibitory) post synaptic potentials EPSP (IPSP). Both EPSP and IPSP of our model are shown in Fig 2.14(b). The synapses are AMPA and  $\text{GABA}_A$  as described in section 2.1.

In this section we use this modified HH model to built-in the MSI motif illustrated in Fig. 2.1 and to look for anticipated synchronization. Once again, controlling the synaptic conductances we can find DS, AS and PD regimes. These regimes can be characterized by the sign of the curve  $\tau_i(\#cycle)$  in Fig 2.14(c). Like in previous sections, the time delay in the transition from DS to AS is a continuous and smooth function of the inhibitory synaptic conductance (see Fig 2.14(d)).

### 2.6.3 AS in the presence of noise

Here, we use experimental data from a patched neuron <sup>1</sup> to improve our model and explore the parameters in which the 3-neurons model of modified HH presents AS. The real cell patched during the experiments fires spikes due to the injection of a noisy current, as we can see in Fig. 2.15 To mimic the membrane potential shown in this figure we have added noise to the constant external current in our model. Then, the interspike interval is not constant, as can be observed in Fig. 2.16(a). The time delay  $\tau$  between the master and the slave also varies in each cycle. However,  $\tau$  maintains a well defined sign, as shown in Fig. 2.16(b) and the system presents both DS and AS regimes depending on the strengths  $g_{IS}$  of the inhibitory synapse (see Fig. 2.17). The mean value of  $\tau$  is a well behaved function of  $g_{IS}$  (as in the case without noise).

---

<sup>1</sup>Experiments were performed by Dr. Marylka Yoe Uusisaari, at the Theoretical and Experimental Neurobiology Unit in the Okinawa Institute of Science and Technology, Japan.

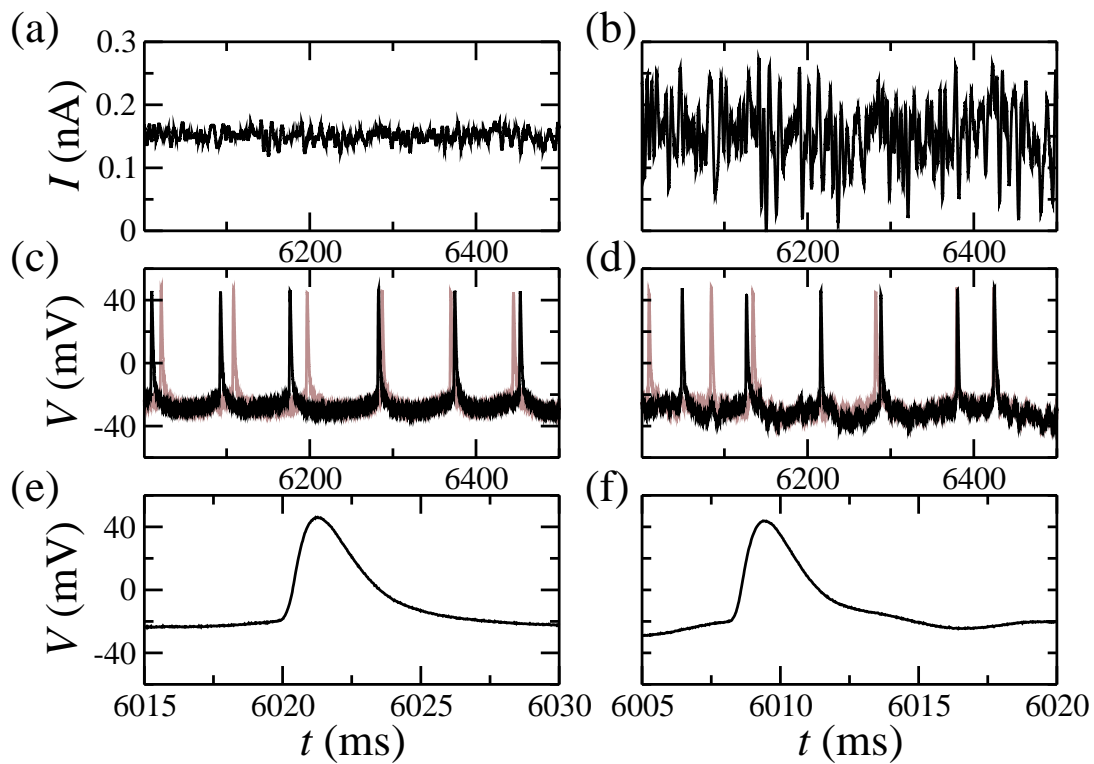


Figure 2.15: Experimental data from a patch clamp recording of cells in sliced tissues. (a) and (b) Injected current in each recording. (c) and (d) Membrane potential of the same cell in two different trials (corresponding to the two colors in each graph) repeating the same noise (respectively (a) and (b)). (e) and (f) Example of an action potential zoomed in from (c) and (d). Data were kindly provided by Dr. Marylka Yoe Uusisaari and Dr. Klaus Stiefel (Okinawa Institute of Science and Technology, Japan).

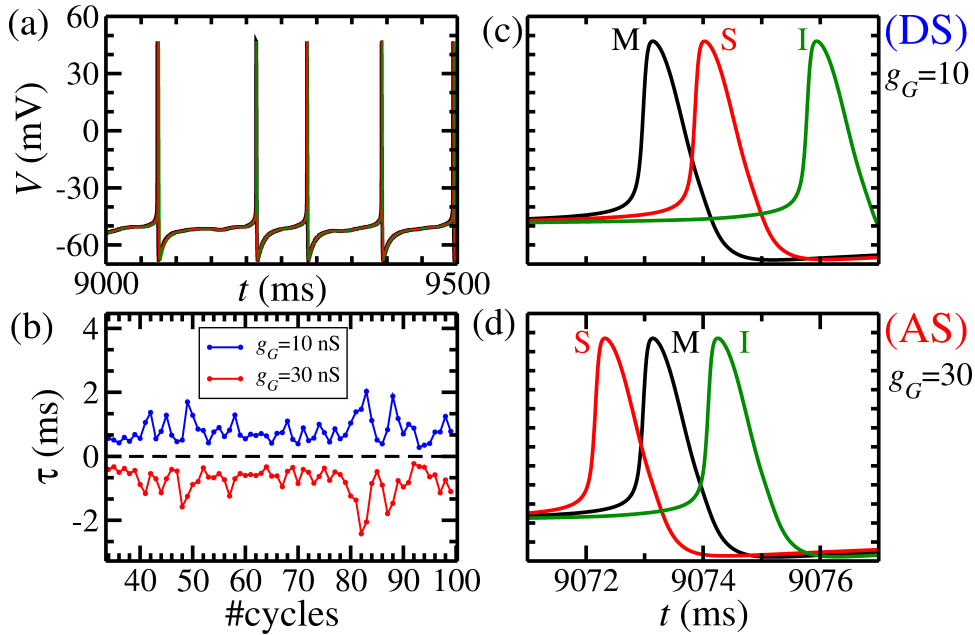


Figure 2.16: Characterizing DS and AS regimes in the presence of noise. (a) With colored noise added to the input current, spiking is not periodic. (b) Under noisy dynamics, the time delay  $\tau$  in each cycle fluctuates around a mean with a well-defined sign (for the DS and AS regimes) (c) and (d) Zoom of two different time series.  $g_G$  controls the relative timing of the master and slave spikes, leading to DS or AS.

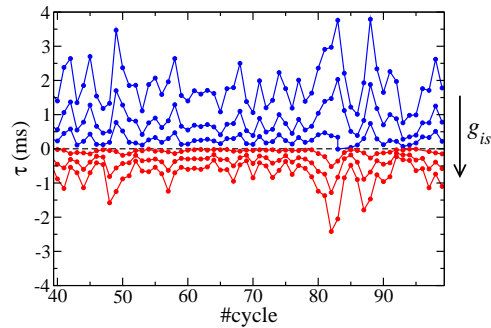


Figure 2.17: Time delay in each period for different values of inhibitory conductances.  $g_G$  increases from top to bottom:  $g_G = 0, 10, 15, 20, 30, 40$  nS.

## 2.7 Other motifs

### 2.7.1 Bidirectional coupling

One practical application of anticipated synchronization is to use the prediction of the slave to prevent or stimulate a certain response in the master. In artificial intelligence an intelligent system should be able to predict and act consequently. It means that if a system which exhibits anticipated synchronization has an internal control system, it could, in principle, act before a

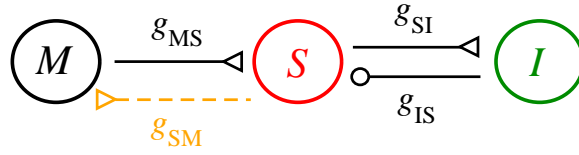


Figure 2.18: Modified MSI motif. We incorporate the effect of a small excitatory feedback from the slave to the master. How does the system go from a unidirectional to a bidirectional coupling?

specific event and avoid undesired behaviors.

Here we are interested in studying the biologically plausible counterpart of two dynamical systems coupled as follows:

$$\begin{aligned}\dot{x} &= f(x(t)) + h(x(t), y(t - t_2)), \\ \dot{y} &= f(y(t)) + K[x(t) - y(t - t_d)].\end{aligned}\tag{2.19}$$

where  $h(x(t), y(t - t_2))$  is an arbitrary coupling function of  $x$  and/or  $y$ . In physical systems, typical couplings are the direct:  $h = y(t - t_2)$  and the diffusive:  $h = y(t - t_2) - x(t)$ . In our biologically inspired model we propose to add an excitatory chemical synapse from the slave to the master to mimic  $h(x(t), y(t - t_2))$ . Compared to Eq. 1.1 the extra term in Eq. 2.19 is an attempt to study the effect of an internal control system. Moreover, in neuroscience the reciprocal connection is of great importance and abundant in the brain. Indeed, bidirectional connections are more than two times as frequent than predicted by chance [89].

Therefore, we investigate the existence of AS regime in the modified 3-neuron motif shown in Fig. 2.18, which has an extra excitatory synapse from the slave neuron to the master. We use the standard HH model and chemical synapses with time decays as in Table 2.1. Each neuron receives an external constant current  $I = 200$  pA, which implies the coexistence of a stable fixed point and a stable limit cycle. In order to mimic the noise, each neuron also receives a square pulsed current. The pulses obeys a Poisson distribution with rate parameter  $R = 200$  Hz. Each pulse has 1 ms width and 200 pA height. Moreover, the master neuron receives an extra Poisson input with  $R = 50$  Hz. Fig. 2.19 shows that the time series from the master and the slave are different, as well as their interspike intervals (ISI). Like before, we define the time delay  $\tau$  as the mean value of the time delay in each period.

Aiming to understand the effect of the excitatory feedback from the slave to the master, we have fixed the conductances constituting the inhibitory loop ( $g_{SI} = g_{IS} = 10$  nS). We start from  $g_{MS} = 10$  nS and  $g_{SM} = 0$  nS, i.e. a unidirectional coupling. Similar to previous results for this canonical master-slave configuration, depending on the inhibitory conductance the system can present both DS ( $g_{IS} = 10$  nS) or AS ( $g_{IS} = 80$  nS) regime. Then we increase the conductances of the reciprocal coupling ( $g_{MS}$  and  $g_{SM}$ ). We have attached the value of  $g_{MS}$  with the  $g_{SM}$  in the following way:  $g_{MS} = g_{SI} + g_{SM}$ , which ensures that  $g_{MS}$  is always larger than  $g_{SM}$ .

The effect of the reciprocal coupling in the AS and DS regimes is shown in Fig. 2.20 by the red and blue dots respectively. If we start in the DS regime ( $g_{IS} = 10$  nS), the time delay almost does not change with the excitatory feedback  $g_{SM}$  ( $\tau \simeq 0.8$  ms). On the other hand, if

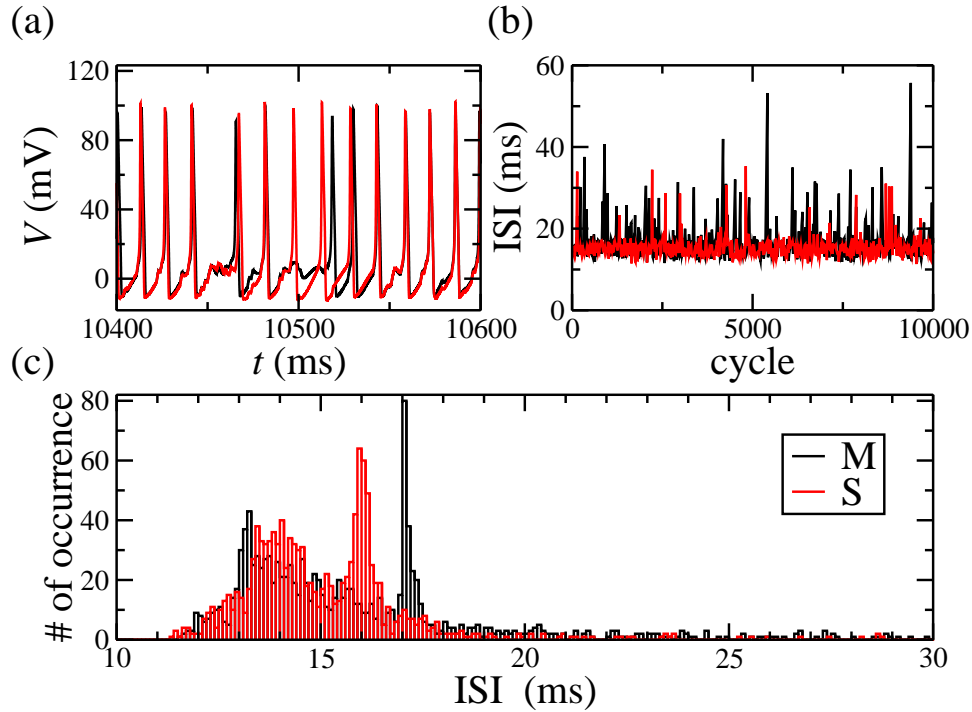


Figure 2.19: Characterizing the standard HH model in the presence of a Poisson input. (a) Time series of the master (black) and the slave (red). (b) Interspike interval (ISI) in each cycle of M and S. (c) Histogram of ISI.

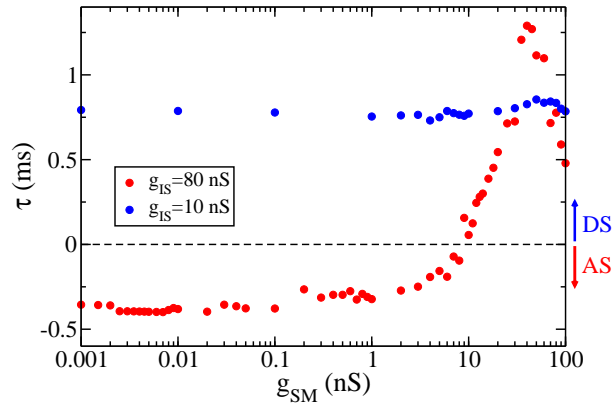


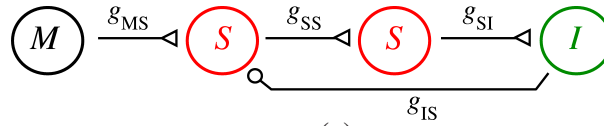
Figure 2.20: Time delay  $\tau$  as a function of the excitatory conductance  $g_{SM}$  from the slave to the master. For  $g_{IS} = 10$  nS (blue dots)  $\tau$  is almost constant and the system exhibits only DS ( $\tau > 0$ ). For  $g_{IS} = 80$  nS (red dots) the system exhibits both AS ( $\tau < 0$  for  $g_{SM} < 10$  nS) and DS ( $\tau > 0$  for  $g_{SM} > 10$  nS).

we start in the AS regime ( $g_{IS} = 80$  nS, represented by the red dots in Fig. 2.20), the time delay persists almost unchanged for small values of  $g_{SM}$  ( $\tau \simeq -0.4$  ms). If we increase  $g_{SM}$  by more than 10% of  $g_{MS}$ ,  $\tau$  increases and the system moves to the DS regime (red dots with  $\tau > 0$  in Fig. 2.20).

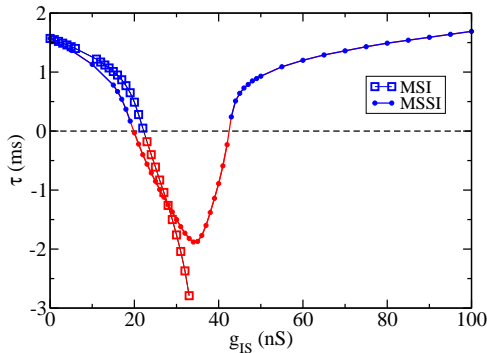
### 2.7.2 An extra slave

It is also possible to find other motifs, with more neurons, that can also exhibit AS. For example, the presence of a second slave as shown in Fig. 2.21(a) may enlarge the set of parameters in which AS occurs. We call this motif master-slave-slave-interneuron (MSSI). The excitatory synapses are mediated by AMPA while the inhibitory is mediated by GABA<sub>A</sub>. In Fig. 2.21(b) and (c) we compare  $\tau$  versus the inhibitory conductance  $g_{IS}$  for the MSI (shown in Fig. 2.1) and the MSSI motifs. In the MSSI configuration the time delay is defined as the time difference between the first slave and the master. The inhibitory synapse  $g_{IS}$  is from the interneuron to the first slave. In Fig. 2.21(b) the synaptic conductances are  $g_A = g_{MS} = g_{SS} = g_{IS} = 6.5$  nS whereas in Fig. 2.21(c)  $g_A = g_{MS} = g_{SS} = g_{IS} = 20$  nS and the synaptic time decays are  $\beta_A = \beta_G = 0.6$  ms<sup>-1</sup>. All other parameters are in the first column of Table 2.1. In Fig. 2.21(b) the extra slave prevents the system to go to the PD regime (stabilizing the phase-locking), while in Fig. 2.21(c) the extra slave increases the anticipation time (i.e. increases the modulus of the time delay  $|\tau|$ ).

(a)



(b)



(c)

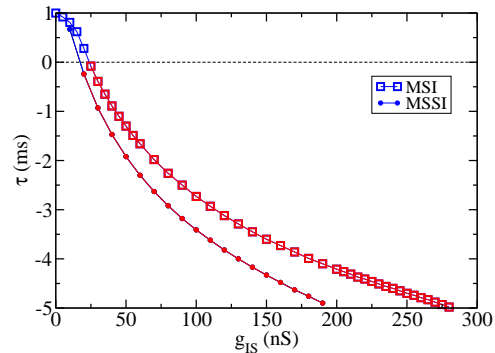


Figure 2.21: Example of a master-slave-slave-interneuron (MSSI) motif. (a) Schematic representation of MSSI. (b) and (c)  $\tau$  as a function of  $g_{IS} = g_G$  for both MSSI and MSI motifs. (b) The excitatory conductance are  $g_A = g_{MS} = g_{SS} = g_{IS} = 6.5$  nS, other parameters as in Table 2.1. (c)  $g_A = g_{MS} = g_{SS} = g_{IS} = 20$  nS and the synaptic time decays are  $\beta_A = \beta_G = 0.6$  ms<sup>-1</sup>.

### 2.7.3 Motor circuit in the spinal cord

Motor behavior can be considered as the ultimate output of the nervous system and is mediated by local spinal circuits [91]. The spinal cord has three major functions: as a conduit for motor information, which travels down the spinal cord; as a conduit for sensory information in the reverse direction; and finally as a center for independently control numerous reflexes and



central pattern generators. The interplay between motor neurons and interneurons results in the appropriate sequence of muscle contractions. Renshaw cells [37, 92] are inhibitory interneurons found in the gray matter of the spinal cord, and are associated in two ways with an alpha motor neuron (see Fig. 2.22). (i) They receive an excitatory collateral from the alpha neuron's axon as they emerge from the motor root, and are thus "kept informed" of how vigorously that neuron is firing. (ii) They send an inhibitory synapse to alpha motor neuron of the same motor pool. In this way, Renshaw cell inhibition represents a negative feedback mechanism.

Since we are interested in inhibitory feedbacks, we simulated a very simple motif to represent the motor circuit in the spinal cord shown in Fig. 2.22. Each label in Fig. 2.23, represents a neuron or types of neurons: (1) agonist alpha motor neuron, (2) Renshaw cell, (3) agonist muscle spindles (sensory receptors), (4) 1a inhibitory neuron (responsible for inhibiting antagonist motor neuron and activated by 1a spindle afferents), (5) antagonist motor neuron, (6) antagonist muscle spindles (sensory receptors), (7) interneuron activated by antagonist muscle spindles which inhibits 1a inhibitory neuron. The synaptic conductance  $g_{IS}$  of this inhibitory synapse is our control parameter.

Each cell was described by a modified Morris-Lecar neuron model, which allows arbitrarily small frequencies [54]:

$$C_m \frac{dV}{dt} = \bar{G}_{Ca} m_\infty(V)(E_{Ca} - V) + \bar{G}_K w(E_K - V) + G_m(V_{rest} - V) + I + \sum I_{syn} \quad (2.20)$$

$$\frac{dw}{dt} = \frac{w_\infty(V) - w}{\tau_\infty(V)}; \quad (2.21)$$

where  $C_m = 1 \mu\text{F}/\text{cm}^2$ ,  $G_{Ca} = 1 \text{ mS}/\text{cm}^2$ ,  $G_K = 2 \text{ mS}/\text{cm}^2$ ,  $G_m = 0.5 \text{ mS}/\text{cm}^2$ ,  $E_{Ca} = 100 \text{ mV}$ ,  $E_K = -70 \text{ mV}$ ,  $V_{rest} = -50 \text{ mV}$  and

$$w_\infty(V) = 0.5 \left( 1 + \tanh \left( \frac{V_m - 10}{14.5} \right) \right) \\ \tau_w(V) = \frac{w_3}{\cosh \left( \frac{V_m - 10}{29} \right)}. \quad (2.22)$$

Synapses were mediated by AMPA and GABA<sub>A</sub> as described previously. All conductances are fixed at  $g = 10 \text{ nS}$  except  $g_{IS}$  which may vary from 5 to 40 nS. The period of each neuron is  $T \approx 16 \text{ ms}$ .

Depending on the values of  $g_{IS}$ , the mean time delay between the agonist and antagonist muscle spindles (neurons 3 and 6 in Fig. 2.23(a)) can be positive or negative. Differently from previous section,  $\tau_i = t_i^6 - t_i^3$  in each cycle oscillates periodically around its mean value (see Fig. 2.23(b)). In this case, AS could be a mechanism to facilitate the activation of the antagonist muscle spindle before the agonist. Since we did not account for conduction delays in this model, the existence of AS regime in this simple situation could at least decrease time delays between spikes in presence of real conduction delays.

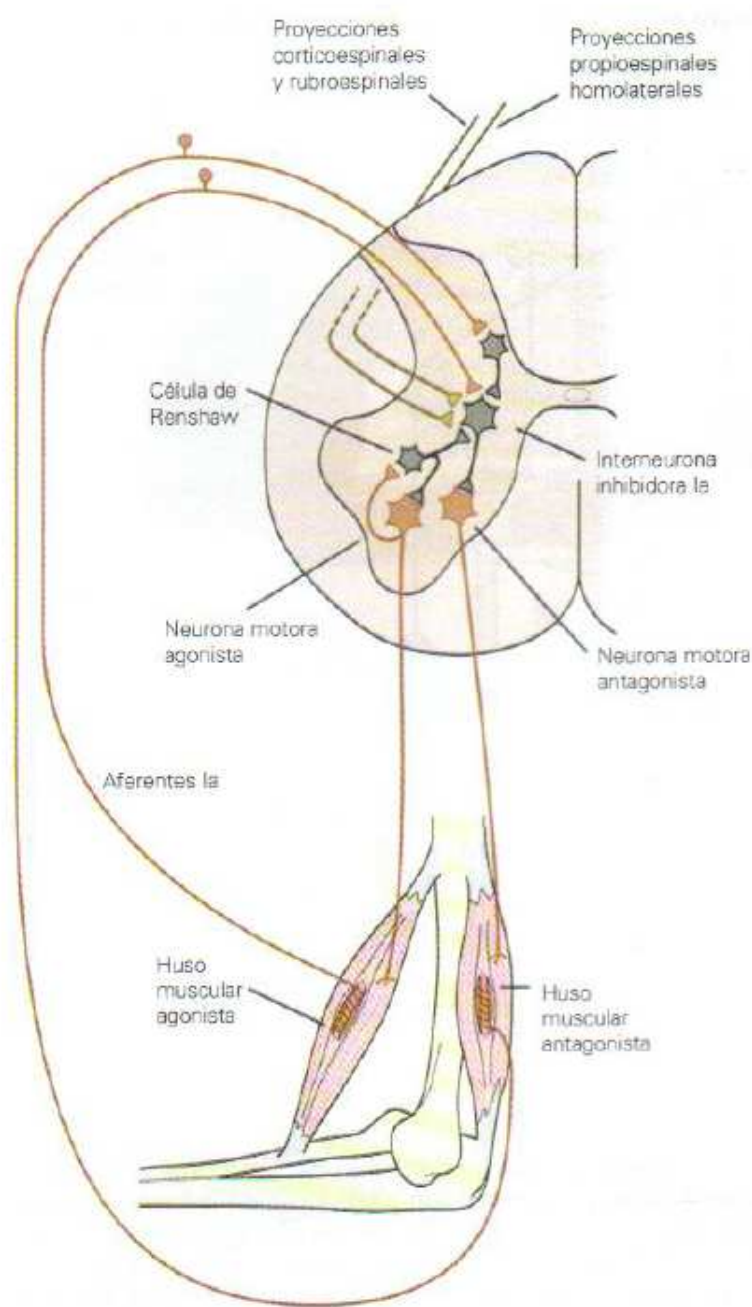
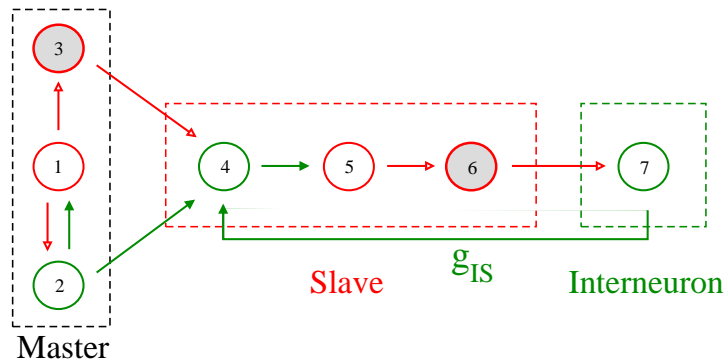


Figure 2.22: Illustration of the motor circuit. There are two inhibitory loops in this circuit. The agonist motor neuron (*Neurona motora agonista*) sends an excitatory synapse to the Renshaw cell (*Célula de Renshaw*), which sends back an inhibitory synapse. The antagonist muscle spindle (*Huso muscular agonista*) excites an interneuron, which inhibits the 1a inhibitory neuron (*Interneurona inhibidora 1a*). The latter inhibits the antagonist motor neuron (*Neurona motora antagonista*), which excites the antagonist muscle spindle closing the inhibitory loop. Moreover the 1a inhibitory neuron receives an excitatory synapse from the agonist muscle spindles (*Neurona motora agonista*) and an inhibitory synapse from the Renshaw cell. Reproduced from Kandel et al. [90].

(a)



(b)

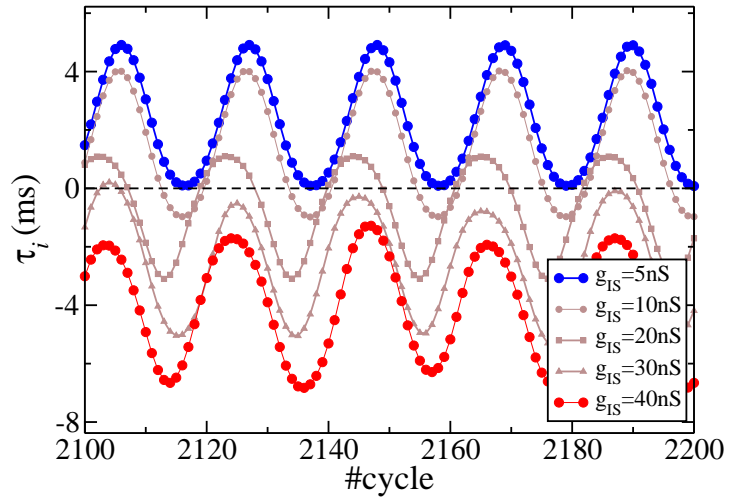


Figure 2.23: Muscle circuit (a) Schematic representation of the circuit shown in Fig. 2.22. (b) Time delay  $\tau_i$  between neurons 3 and 6 in each cycle.  $\tau_i$  oscillates, but for  $g_{IS} = 5$  nS it is always positive indicating a DS regime, whereas for  $g_{IS} = 40$  nS,  $\tau_i < 0$  which characterizes an AS regime.



## Phase response curve

### 3.1 What is it and why is it useful?

Self-sustained oscillatory patterns are well spread in biological systems. The rhythmic activity of populations of fireflies, cardiac pacemak cells and neuronal circuits are just a few examples. All these biological oscillations can be described mathematically by limit cycle attractors which are responsible for periodicity in dynamical systems. However, the complete understanding of the mechanistic bases of synchronization is a current challenge in the interface of physics and biology [93].

Here we are interested in the relation between the synchronization of a few coupled neurons and their intrinsic dynamics [94]. Phase response curves (PRCs) are one the main tools to characterize the effects of a perturbation applied to limit cycles and may predict qualitative features of a particular oscillation subjected to perturbations. Therefore, it is useful for linking the response of individual neurons to perturbations and the dynamics of the entire neuronal network.

Let  $t_0$  be an arbitrary point on a periodic orbit of a nonlinear system, then any other point on the periodic orbit can be characterized by the time,  $\theta$ , since the last passing of  $t_0$ . The variable  $\theta$  is called phase of oscillation, and it is bounded by the period of oscillation  $T$  [95]. The phase response of a periodically spiking neuron (with period  $T$ ) represents the change in its phase due to a perturbation in a specific moment  $t$ . The magnitude of the phase shift in the spike train depends on the shape and the exact timing  $t$  of the stimulus. We numerically calculate the PRC sending the same stimulus at different times  $t$  and measuring the shift on the phase of oscillation  $PRC(t)$ . Typically we plot the PRC due to a square pulse current which arrives in a moment  $t$  and evokes a phase response  $PRC(t)$  in the next spike. For simplicity, unless otherwise stated, we convert the phase shifts to time delays and measure the PRC in seconds (not in radians). We arbitrarily choose  $t_0 = 0$  to correspond to the peak of each spike.

In Fig. 3.1(a) we show a qualitative example of an applied external current  $I(t)$  and its effect in the mean membrane potential of a neuron (dashed line represents the undisturbed or free-running trajectory). We define  $PRC(t) = t_{spike}^{free} - t_{spike}^{disturbed}$  (see Fig. 3.1(a)), where  $t_{spike}^{free}$  is the spike timing of the free-running neuron and  $t_{spike}^{disturbed}$  is the spike timing of the disturbed neuron. By our convention,  $PRC(t) > 0$  if the next spike is advanced. It means that the disturbed neuron fires before it would do in the absence of the stimulus. On the other hand,  $PRC(t) < 0$  if the next spike is delayed. In Fig. 3.1(b) we show the PRC of an Hodgking-Huxley neuron due to a small current pulse: with height  $H = 1$  nA and width  $L = 0.01$  ms. Exactly the same curve is obtained for a different small pulse with the same area:  $H = 10$  nA and  $L = 0.001$  ms.

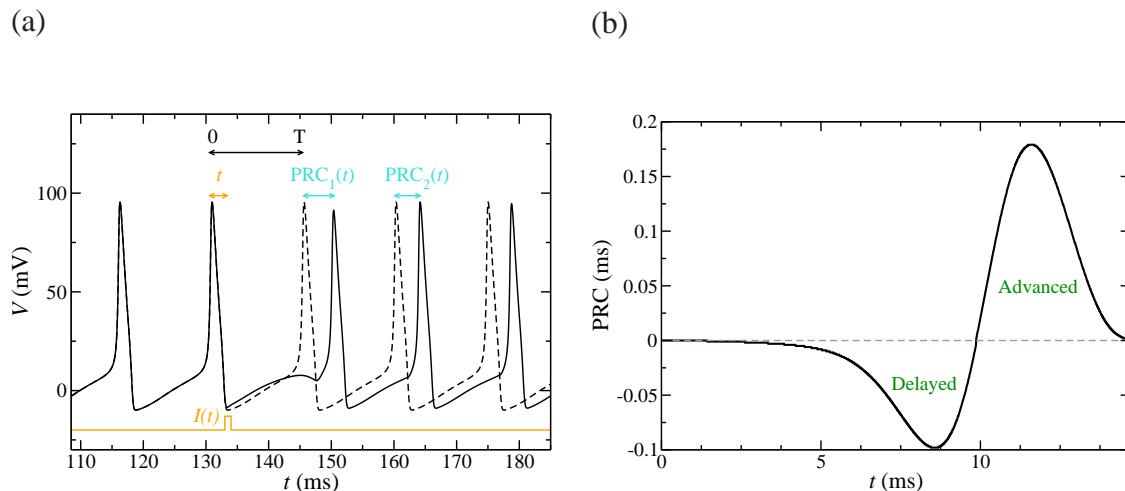


Figure 3.1: Definition of phase response curve (PRC) (a) Example of an applied external current  $I(t)$  and its effect in the mean membrane potential of a neuron. Dashed line represents the free-running trajectory (in the absence of  $I(t)$ ). We define  $PRC(t) = t_{spike}^{free} - t_{spike}^{disturbed}$  as the effect of  $I(t)$  in the next spike of the neuron. In this example, the stimulus was applied at a time  $t = 2$  ms after the spike. The subsequent spike of the perturbed neuron was delayed by 4.7 ms, in comparison with the free-running neuron, hence  $PRC(2 \text{ ms}) = -4.7 \text{ ms} < 0$ . (b) PRC as a function of the time  $t$  in which an infinitesimal square pulse current  $I(t)$  was applied.

We also define  $PRC_1(t)$  as the phase shift in the first spike after the perturbation while  $PRC_2(t)$  is the phase shift in the second spike. It is also possible to define the  $PRC_3(t)$  and so on. If the perturbation is sufficient small, one expects and verifies that  $PRC_1(t) = PRC_2(t) \equiv PRC(t)$ . It is worth to mention that the PRC can be calculated for an arbitrary stimulus, not necessarily weak or brief. The only condition to do it correctly is to wait enough time to ensure that  $PRC_i(t) = PRC_{i-1}(t)$ . However, this become a limiting factor when we use PRC to study synchronization of periodic coupled oscillators as we will do in the following sections.

There are two main types of neurons in respect to the sign of their PRC. When small depolarizations produced by excitatory postsynaptic potentials only produce advances in the phase of the neuron, the phase response is a non-negative curve and we call it a Type-I neuron. In Type-II neurons both positive or negative PRC can be produced, depending upon the timing of the excitatory stimulus (as shown in Fig. 3.1(b)). For infinitesimal perturbations this classification of PRC [96] is closely related to the classification of excitable membranes in respect to the applied depolarizing currents. However, it is more accurate to relate the type of the PRC to the existence of subthreshold oscillations [97].

Class-I excitable membranes can fire arbitrarily slowly near the onset of firing (may oscillate with arbitrarily small frequency), whereas Class-II excitable membranes have an abrupt onset of repetitive firing at a threshold frequency, and cannot be induced to fire at any frequency below the threshold frequency. Class-I membrane excitability is typically exhibited by models near a saddle-node on invariant circle bifurcation, and Class-II near an Andronov-Hopf bifurcation [98] (which is the case of the HH model). Then, Ermentrout [96] has concluded that

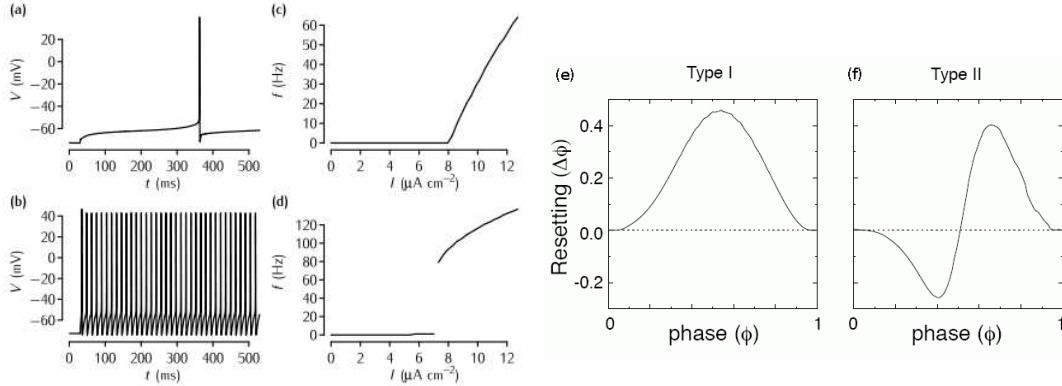


Figure 3.2: Two types of neurons based on membrane excitability and PRC. In (a),(c) and (e) we show an example of a Type-I neuron, whereas in (b),(d) and (f) we show an example of a Type-II neuron. Figure adapted from Sterratt et al. [99] and Canavier [97].

Type-I PRC is associated with Class-I excitability and Type-II PRC with Class-II excitability. For example, this relation is valid for the HH model, which is a Type II PRC and a Class-II excitability. In Fig. 3.2 we show examples of Class-I and II excitability and Type-I and Type-II PRC.

However, more recently, an abrupt onset of firing (Class-II excitability) may also be observed in the case of a saddle-node bifurcation away from the limit cycle [94]. Therefore, Izhikevich has proposed to classify the neurons accordingly to both bifurcation and resting state. By his definition, a neuron is a resonator if exhibits subthreshold oscillations and as integrator if there are no subthreshold oscillations. All resonators are Class-II, but the integrators can be both Class-I or Class-II. In this sense, it was verified that Type-I PRC is better associated to an integrator and Type-II PRC with a resonator [97].

In the theory of weakly coupled oscillators the  $PRC_{inf}$  generated by an infinitesimal stimulus is called linear response function, infinitesimal PRC, kernel, or Green's function. This function can be convolved with the actual input received by each oscillator (usually a synaptic conductance  $I(t)$ ) in order to compute the total  $PRC_I(t)$  of the oscillator received over one cycle of the network oscillation:

$$PRC_I(t) = \frac{1}{C} \int_0^T PRC_{inf}(\tau) I(t + \tau) d\tau. \quad (3.1)$$

It is also possible to measure the spike time response curve (STRC) as the PRCs generated by an action potential to drive the change in postsynaptic conductance. In all cases we can just refer the function as PRC but it is necessary to specify which stimulus has generated it.

## 3.2 Master-Slave: two unidirectionally coupled oscillators

### 3.2.1 Poincaré phase map

Several mathematical formulations allow the time evolution of coupled oscillators to be described by a map from one cycle to the next. For example the class of pulse coupled methods [100] and weak coupling methods [95, 101, 102] make use of the PRC to calculate Poincaré phase maps. While in the weak coupling method we convolve a perturbation with  $PRC_{inf}$ , in the pulse coupled method we simply use the perturbation itself to generate the PRC (or STRC). If the coupling is not sufficiently weak but is pulsatile in nature, the method of pulse coupled oscillators should be utilized. Although the PRC can be calculated for any input, both methods require that the timing of each spike is affected by only presynaptic spikes within one period. In other words, it is necessary that there is no second or higher order effects of the PRC.

These ideas have been employed to study the response of a neuron to a periodic stimulus such as synaptic inputs from a periodic pre-synaptic neuron. In particular, we are interested in the synchronization between two unidirectionally coupled neurons: the master and the slave (MS motif). Once we know the PRC of the slave due to the synaptic stimulus and the time delay between the two neurons in one cycle, we can predict the time delay in the following cycle. Fig. 3.3(a) illustrates spikes of the master and its effect (through the synapse) in the spikes of the slave according to the PRC. The time since the first spike of the slave until the second spike of the master can be geometrically obtained by two different sums (see Fig. 3.3(a)), which give us the following relation:

$$\theta_0 + T_M = T_S - PRC(\theta_0) + \theta_1. \quad (3.2)$$

Generalizing it for any period, we find the Poincaré phase map [94]:

$$\theta_{n+1} = \theta_n + PRC(\theta_n) + T_M - T_S, \quad (3.3)$$

where  $\theta_n$  is the time between the  $n$ -th spike of the slave and the  $n$ -th spike of the master,  $T_M$  and  $T_S$  are the periods of the master and the slave.

If the system goes to a phase-locking regime, the time delay between consecutive spikes of the master and the slave will be the same in each period. Thus  $\theta_{n+1} = \theta_n \equiv \theta^*$  and consequently  $PRC(\theta^*) = T_S - T_M$ . We say  $\theta^*$  is a fixed point that could be stable or unstable depending on the slope of the curve as a function of  $\theta^*$ . In the particular case of  $T_S = T_M$ ,  $PRC(\theta^*) = 0$ , which means that the synapse from the master always arrive in the slave membrane potential in the exactly time in which it causes no effect in the next spike.  $\theta^*$  is stable if  $|1 + PRC'(\theta^*)| < 1$ , which ensures that a positive slope indicates unstable fixed point. By no means we are limiting the coupling to be excitatory. If the synaptic current is too large, the first order of the phase response,  $PRC_1$ , is very different from higher orders of the PRC and Eq. 3.3 could be inappropriate to describe the synchronization of a master-slave system.

## 3.3 Slave-Interneuron: bidirectional coupling

The next level of complexity is two reciprocally coupled neurons. Mirollo and Strogatz [103] formulated the general map for any two coupled oscillators in which the state variable (i.e. the



membrane potential  $V$ ) is a smooth monotonically increasing and concave down function of the time, (for example the leaky integrator). For identical oscillators in which the coupling term is zero at a phase of both 0 and  $T$ , synchrony with zero lag is always a solution. However, other solutions are possible. For systems in which the PRC does not disappear at 0 and  $T$  synchrony may not be a solution. Therefore criteria are required for both existence and stability, as we will show [100].

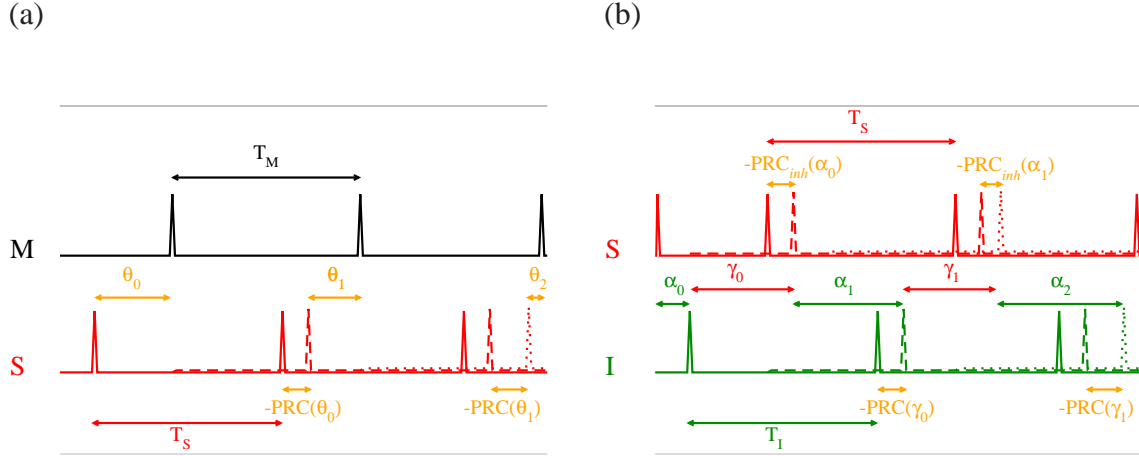


Figure 3.3: Illustration of the temporal trace of a neuron and the effect of the synaptic current between coupled neurons on their following spikes. Differently from Fig. 3.1, the solid line represents the free-running trajectory and the dashed line the spike due to the presynaptic currents in that cycle. (a) Two neurons coupled in a master-slave configuration (MS, unidirectional coupling). Each spike of the slave (S) is perturbed by the synaptic current from the master (M). By definition, the perturbation is the  $PRC(t)$  (b) Two neurons coupled in a slave-interneuron configuration (SI, bidirectional coupling). Each spike of the slave (S) is perturbed by the synaptic current from the interneuron (I), whereas each spike of the interneuron is perturbed by the synaptic current from the slave.

First we define  $\gamma_n$  as the time difference between the  $n - th$  consecutive spikes of the slave  $t_n^S$  and the interneuron  $t_n^I$  and the opposite order for  $\alpha_n$  we have:

$$\begin{aligned}\gamma_n &= t_n^S - t_n^I \\ \alpha_n &= t_n^I - t_{n-1}^S\end{aligned}\quad (3.4)$$

Then, the map based on the PRCs for two pulse coupled oscillators is generated as follows. By Fig. 3.3(b) it is possible to geometrically define  $\alpha_1$  as a function of  $\gamma_0$  and  $PRC(\gamma_0)$ , where  $\gamma_0$  is a function of  $\alpha_0$  and  $PRC_{inh}(\alpha_0)$  and generalize the relation to each period  $n$ :

$$\gamma_n = -\alpha_n - PRC_{inh}(\alpha_n) + T_S \quad (3.5)$$

$$\alpha_{n+1} = -\gamma_n - PRC(\gamma_n) + T_I. \quad (3.6)$$

Therefore, it is possible to represent this map by just one equation:

$$\alpha_{n+1} = \alpha_n + PRC_{inh}(\alpha_n) - PRC(\gamma_n) + T_I - T_S. \quad (3.7)$$

This result is in agreement to the one obtained for pulse coupled oscillators [100]. In our particular case of the SI motif, in the phase-locking regime  $\alpha_{n+1} = \alpha_n$ ,  $T_I = T_S$  and  $\alpha^* = T - \gamma^*$ . Then, the map can be reduced to the following condition:

$$PRC_{inh}(T - \gamma^*) = PRC(\gamma^*), \quad (3.8)$$

where  $T$  is the period of the phase-locking, which can be equal to  $T_S$  and  $T_I$  or not.

### 3.3.1 Stability analysis

Linearizing around the fixed point  $\theta^*$ :

$$PRC(\theta_n) = PRC(\theta^*) + PRC'(\theta^*)\Delta\theta_n \quad (3.9)$$

$$\Delta\theta_n = \theta_n - \theta^* \quad (3.10)$$

where  $\theta = \alpha$  or  $\gamma$ , in Eq. 3.7, we obtain the following approximated map in the neighborhood of the stationary solution:

$$\Delta\alpha_{n+1} = [(PRC'_{inh}(\alpha^*) + 1)(PRC'(\gamma^*) + 1)]\Delta\alpha_n. \quad (3.11)$$

If  $|(PRC'_{inh}(\alpha^*) + 1)(PRC'(\gamma^*) + 1)| < 1$ , then  $\Delta\alpha_{n+1}$  goes to zero and the locking at  $(\alpha, \gamma)$  is stable.

It is important to notice that  $PRC_{inh}(\alpha)$  does not necessarily comes from an inhibitory pulse. We use this notation just because we are interested in comparing our results to the Slave-Interneuron motif. The results obtained here are sufficiently general to describe any kind of bidirectional coupling between two neurons (mutually excitatory, mutually inhibitory, excitatory-inhibitory...) and it does not requires that the oscillators are equal. However, like in the previous section, this map is correct only if the first order PRC is sufficiently greater than the others. Moreover, the cells should alternate in firing (i. e., S - I - S - I...).

## 3.4 Master-Slave-Interneuron coupling

To the best of our knowledge, the Poincaré map of this motif (represented in Fig. 2.1(a)) has not been reported. Similar to what we did before, we can define the time differences between neurons as:

$$\begin{aligned} \beta_n &= t_n^M - t_n^S \\ \gamma_n &= t_n^S - t_n^I \\ \alpha_n &= t_n^I - t_{n-1}^S \end{aligned} \quad (3.12)$$

and define the return map based on geometrical features. Calculating the time difference between the second spike of the master and the first spike of the slave:

$$\beta_0 + T_M = T_S + (-PRC(\beta_0) - PRC_{inh}(\alpha_0)) + \beta_1. \quad (3.13)$$

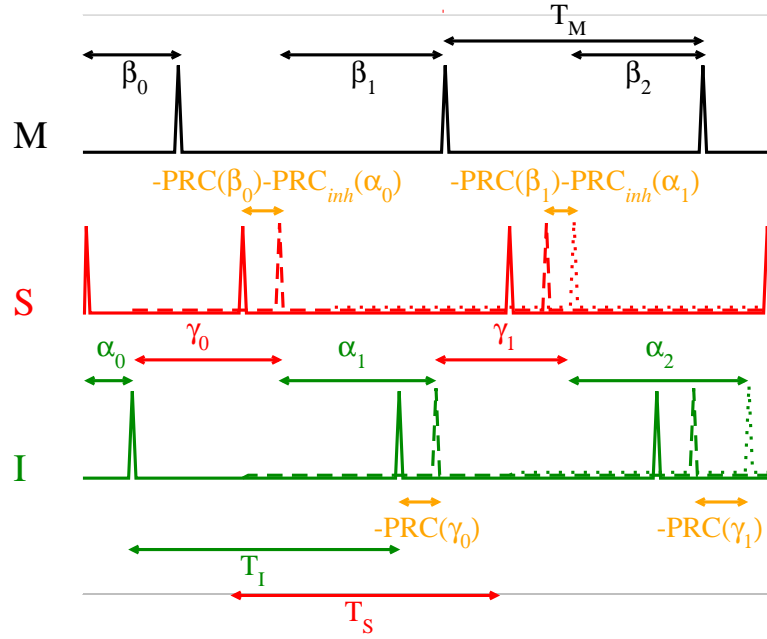


Figure 3.4: Three coupled neurons in a master-slave-interneuron configuration (MSI). Each spike of the slave (S) is perturbed by the synaptic current from the master (M) and the interneuron (I), whereas each spike of the interneuron is perturbed by the synaptic current from the slave. The Poincaré map of this configuration provides the time differences between the three neurons in the phase-locking regime.

Measuring the time since the first spike of the slave until its second spike and looking just to S and I we find:

$$\alpha_0 + \gamma_0 = T_S + (-PRC(\beta_0) - PRC_{inh}(\alpha_0)). \quad (3.14)$$

The time between the first and second spike of the interneuron gives us:

$$T_I + (-PRC(\gamma_0)) = \gamma_0 + \alpha_1, \quad (3.15)$$

where  $\gamma_0 = T_S - PRC(\beta_0) - PRC_{inh}(\alpha_0) - \alpha_0$ . Generalizing the three equations above and rewriting the terms we obtain the desired map:

$$\beta_{n+1} = \beta_n + PRC(\beta_n) + PRC_{inh}(\alpha_n) + T_M - T_S \quad (3.16)$$

$$\gamma_n = -\alpha_n - PRC(\beta_n) - PRC_{inh}(\alpha_n) + T_S \quad (3.17)$$

$$\alpha_{n+1} = \alpha_n + PRC(\beta_n) + PRC_{inh}(\alpha_n) - PRC(\gamma_n) + T_I - T_S. \quad (3.18)$$

Since according to Eq. 3.16 and 3.17,  $\gamma_n = \gamma_n(\alpha_n, \beta_n)$ , this is in fact a two-dimensional map, which means that one of the equations can be suppressed. However, this is a more didactic way to represent it.

Two important assumptions were done here. First, we assumed that the effect of two different stimulus is the sum of each one separately. Second, we considered that the three neurons

fire in each cycle. The order of the fire does not matter (M - S - I; S - I - M; or S - M - I), but it should not change along the numerical calculation. Furthermore,  $PRC(\beta)$  and  $PRC(\gamma)$  are independent functions.

### 3.4.1 Particular case

In the special case in which the slave and the interneuron are described by the same equations and the excitatory synapses MS and SI are equal, we have:

$$PRC(\beta) = PRC(\gamma), \quad \forall \beta = \gamma. \quad (3.19)$$

Moreover, if the free-running period of the three neurons are the same, then  $T_M = T_S = T_I \equiv T$ . In the stationary situation  $\beta_{n+1} = \beta_n = \beta^*$  and Eqs. 3.16, 3.17 and 3.18 reduce to:

$$PRC(\beta^*) + PRC_{inh}(\alpha^*) = 0 \quad (3.20)$$

$$PRC(\beta^*) + PRC_{inh}(\alpha^*) - PRC(\gamma^*) = 0. \quad (3.21)$$

In the phase-locking regime:

$$\gamma_n = \gamma^* \Rightarrow PRC(\gamma^*) = 0 \quad (3.22)$$

$$PRC(\beta^*) = -PRC_{inh}(T - \gamma^*). \quad (3.23)$$

By our own definition of the time delay in the previous chapter:  $\beta^* = t^M - t^S \equiv -\tau \pmod{T}$ . In other words, in AS we have:  $\beta^* = -\tau$  whereas in DS we have:  $\beta_n = T - \tau$ . Then we expect small  $\beta^*$  in the AS regime, and large  $\beta^*$  for DS regimes. This analysis, together with the shapes of the PRC for the HH, gives us a good intuition about the necessary conditions for the existence of AS.

For example, since we know that in all examples of AS and DS the Interneuron fires right after the Slave, we expect  $\gamma^* > T/2$  (see e.g. Fig. 2.2). So  $PRC(\gamma^*)$  should cross the axis with negative slope in the second half of the period, like in Fig. 3.5(a) and (c). Moreover,  $\gamma^* > T/2 \Rightarrow \alpha^* < T/2$ . If  $PRC(\beta) = PRC(\gamma) = -PRC_{inh}(\alpha)$ ,  $\forall \beta, \alpha$  and  $\gamma$ , then  $\beta^* = \alpha^*$ . That means  $\beta^* < T/2$ , which implies  $\tau < 0$  and hence that AS is a solution. In addition, the Interneuron and the Master fire at the same moment.

### 3.4.2 Stability Analysis

Similarly to what we did in the stability analysis for the SI case, we write:

$$PRC(\theta_n) = PRC(\theta^*) + PRC'(\theta^*)\Delta\theta_n \quad (3.24)$$

$$\Delta\theta_n = \theta_n - \theta^* \quad (3.25)$$

where  $\theta = \alpha, \beta$ , or  $\gamma$ . Using the equations above,  $T = \alpha^* + \gamma^*$ , and the following relations:

$$T_S - PRC(\beta^*) - PRC(\alpha^*) = T_I - PRC(\gamma^*) \equiv T \quad (3.26)$$

$$(3.27)$$

in the maps 3.16- 3.18, we find:

$$\Delta\alpha_{n+1} = \Delta\alpha_n + PRC'(\alpha^*)\Delta\alpha_n + PRC'(\beta^*)\Delta\beta_n - PRC'(\gamma^*)\Delta\gamma_n \quad (3.28)$$

$$\Delta\gamma_n = -\Delta\alpha_n - PRC'_{inh}(\alpha^*)\Delta\alpha_n - PRC'(\beta^*)\Delta\beta_n \quad (3.29)$$

$$\Delta\beta_{n+1} = \Delta\beta_n + PRC'(\beta^*)\Delta\beta_n + PRC'_{inh}(\alpha^*)\Delta\alpha_n. \quad (3.30)$$

Then, the stability condition can be written as follows:

$$\begin{aligned} \Delta\alpha_{n+1} &= [1 + PRC'_{inh}(\alpha^*) + PRC'(\gamma^*)PRC'_{inh}(\alpha^*)PRC'(\gamma^*)]\Delta\alpha_n \\ &\quad + [PRC'(\beta^*) + PRC'(\beta^*)PRC'(\gamma^*)]\Delta\beta_n \end{aligned} \quad (3.31)$$

$$\Delta\beta_{n+1} = [PRC'_{inh}(\alpha^*)]\Delta\alpha_n + [1 + PRC'(\beta^*)]\Delta\beta_n \quad (3.32)$$

This relation can be written in a matrix representation as:

$$\begin{pmatrix} \Delta\alpha_{n+1} \\ \Delta\beta_{n+1} \end{pmatrix} = \begin{pmatrix} A & B \\ C & D \end{pmatrix} \begin{pmatrix} \Delta\alpha_n \\ \Delta\beta_n \end{pmatrix}$$

where A,B,C,D are the terms between square brackets in Eqs. 3.31 and 3.32. The stability condition requires that the eigenvalues of the square matrix  $\lambda_1$  and  $\lambda_2 \in (-1,1)$ .

### 3.4.3 Phase model

Coupled oscillators interact via mutual adjustment of their amplitudes and phases. For weak couplings, amplitudes are relatively constant and the interactions could be described by phase models [52, 95]. In such approach our MSI motif would be described by the following differential equations:

$$\begin{aligned} \dot{\theta}_M &= \omega_M \\ \dot{\theta}_S &= \omega_S + f(\theta_M - \theta_S) + g(\theta_I - \theta_S) \\ \dot{\theta}_I &= \omega_S + h(\theta_S - \theta_I). \end{aligned} \quad (3.33)$$

Redefining the variables as:

$$\begin{aligned} \varphi &\equiv \theta_S - \theta_M \\ \psi &\equiv \theta_S - \theta_I, \end{aligned} \quad (3.34)$$

we can reduce our problem to two ODE's:

$$\begin{aligned} \dot{\varphi} &= \omega_S - \omega_M + f(-\varphi) + g(-\psi) \\ \dot{\psi} &= \omega_S - \omega_I - h(\psi) + f(-\varphi) + g(-\psi). \end{aligned} \quad (3.35)$$

These equations are related to the map in Eqs. 3.16- 3.18 replacing  $\varphi$  by  $-\beta$ ,  $\psi$  by  $\alpha$ ,  $f, g$  and  $h$  by  $PRC(\beta), PRC_{inh}(\alpha)$  and  $PRC(\gamma)$  respectively. The phase model is often employed in analytical calculations. Particularly when the PRC can be approximated by simple functions as sines, cosines or piecewise-like functions.

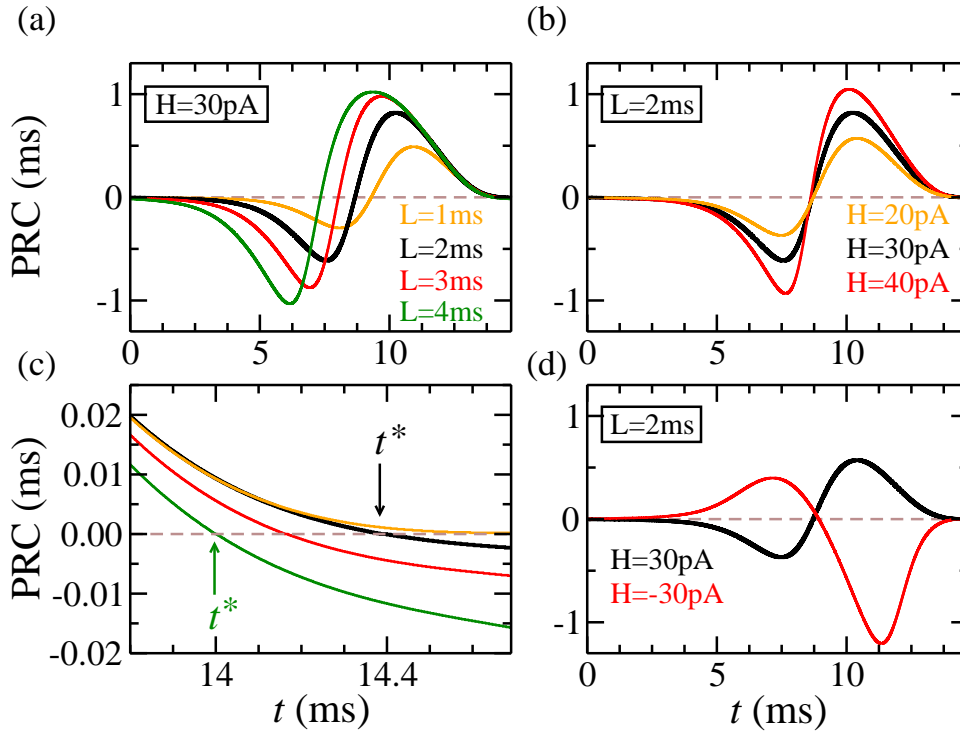


Figure 3.5: Phase response curve of a quadratic current pulse with width  $L$  and height  $H$ . (a)  $H = 30$  pA and different values of  $L$ . (b) Fixed  $L = 2$  ms and varying  $H$ . (c) the same plot as in (a) with a zoom in the region close to the fixed point  $PRC(t^*) = 0$ . (d) The effect of negative  $H = -30$  pA in the quadratic pulse simplification, which is the analogous of an inhibitory synaptic current.

### 3.5 Numerical results

The phase responses curves of a Type-II neuron generated by different pulses are shown in Fig. 3.5. We choose the PRC produced by a pulse with height  $H = 30$  pA and width  $L = 2$  ms as the standard curve (black lines) and compare it to PRCs yielded by different heights and widths. Firstly, in Fig. 3.5(a) we fixed  $H$  and changed  $L$ . Fig. 3.5(c) exhibits the same plot with a zoom in the region close to the fixed point  $PRC(t^*) = 0$ . Secondly, we fixed  $L$  and vary  $H$ , which is shown in Fig. 3.5(b). Finally, we compared the effect of a negative pulse on the PRC, which is the equivalent of an inhibitory coupling in our simplified model of quadratic synaptic pulse (see Fig. 3.5(d)). We emphasize that, for these HH neurons, even in this simple approach excitation and inhibition are *not* simply the reflection of one another around the axis  $PRC = 0$ .

Using quadratic pulses as the synaptic current from the master to the slave, we compare the time delay  $\tau$  between the two neurons obtained from two different methods. First we simulate the MS motif of HH neuron as we did in Chapter 2, replacing the chemical synapses by quadratic pulsed with height  $H = 30$  pA. The black dots in Fig. 3.6(a) represent  $\tau$  as a function of the width  $L$  of the synapse. Second, for each value of  $L$  we numerically calculate the respective PRC and use the map represented by Eq. 3.3 to calculate  $\theta^*$ . Then we obtain  $\tau$

using the following relations: if  $\theta > T/2 \Rightarrow \tau = T - \theta$ , otherwise  $\tau = -\theta$  (see orange dots in Fig. 3.6(a)). Although results are in a good agreement, for  $L > 6$  ms there is a distinguishable difference between the values of  $\tau$  obtained with each methods. It is worth mentioning that  $\theta^*$  is almost constant for fixed  $L = 2$  ms and different values of  $H$ .

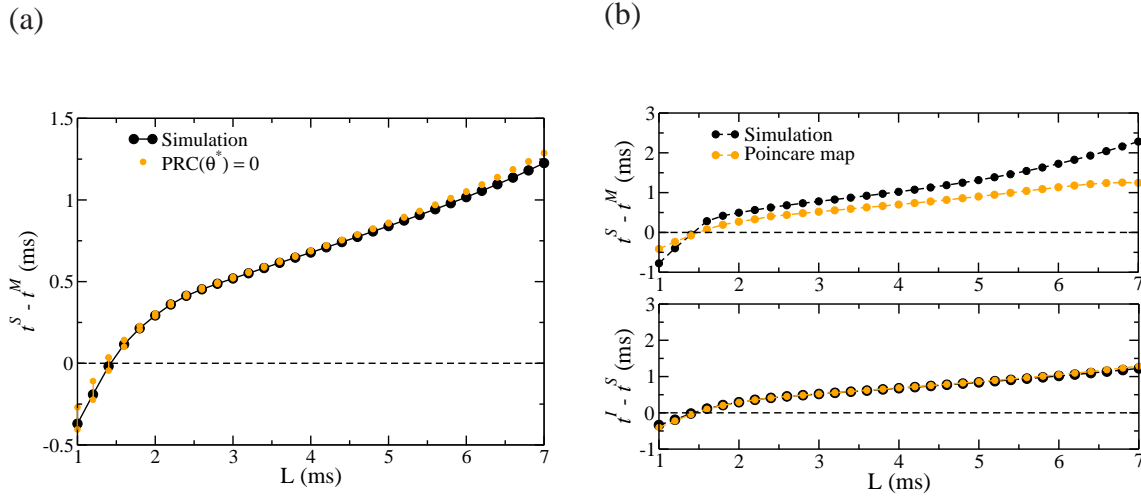


Figure 3.6: Comparison of the time delay between neurons using the Poincaré map (orange) and the simulations results for two motifs. (a) The unidirectionally coupled master-slave motif. (b) The 3-neuron motif MSI.

We repeat the same procedure in order to compare both methods for the MSI motif. In the simulation of the 3-neuron circuit, the inhibitory synapse has  $H_{IS} = -30$  pA, the excitatory synapses have  $H_{MS} = H_{SI} = 30$  pA and we vary the width of the three synapses together:  $L_{MS} = L_{SI} = L_{IS} = L$  (from 1 to 7 ms). The time difference between the master and the slave as a function of  $L$  is represented by the black dots in Fig. 3.6(b). Then, we calculated the numerical  $PRC(\beta)$  and  $PRC(\gamma)$  using a quadratic pulse of  $H = 30$  pA, and the  $PRC_{inh}(\gamma)$  using a quadratic pulse of  $H = -30$  pA. Finally, we use the phase response functions in the Eq. 3.18 to calculate  $\beta^*$  and  $\alpha^*$  for each set of widths. These results are represented by the orange dots in Fig. 3.6(b). The two methods provide coincident values of  $\alpha^* = t^I - t^S$  and the same sign of  $\tau$ , but not coincident values. It suggests the assumption of weak coupling may not apply here.

The spike time response curve  $STRC_{AMPA}$  for the HH neuron produced by the first order AMPA synapse used in Chapter 2 is shown in Fig. 3.7(a). If we use the map in Eq. 3.3 and the fact that this curve crosses the axis in  $t = T$  with negative slope we would expect that two undirected coupled neuron with AMPA synapse synchronize with zero lag. However, we have shown in Chapter 2 that they synchronize with  $\tau = 1.5$  ms (see Fig. 2.5). It suggests that chemical synapses are too large comparable to the period of the HH model to use even the simplest map of two unidirectionally coupled neurons. Indeed, in Fig. 3.7(a) we compare the  $STRC_{AMPA}$  with the PRC generated by a quadratic pulse of  $H = 30$  pA and  $L = 2$  ms. and the  $STRC_{AMPA}$  is almost 6 times larger than the PRC.

One possibility to achieve the weak coupling requirement in order to reconcile the values of  $\tau$  obtained from the simulations and from the PRC map is to use other neuron models that

can present larger periods. For example, we can try the modified HH presented in Sec. 2.6 (see Eq. 2.16). Fig. 3.7(b) shows the PRC of this model for a quadratic pulse with  $L = 2$  ms and  $H = 30$  pA (black circles) and  $H = -30$  pA (orange circles). Preliminary results suggest that the weak coupling approximation is more appropriate for this modified HH model than for the standard HH model. The possibility of gaining analytical insight into the mechanisms underlying AS is worth pursuing and remains under investigation.

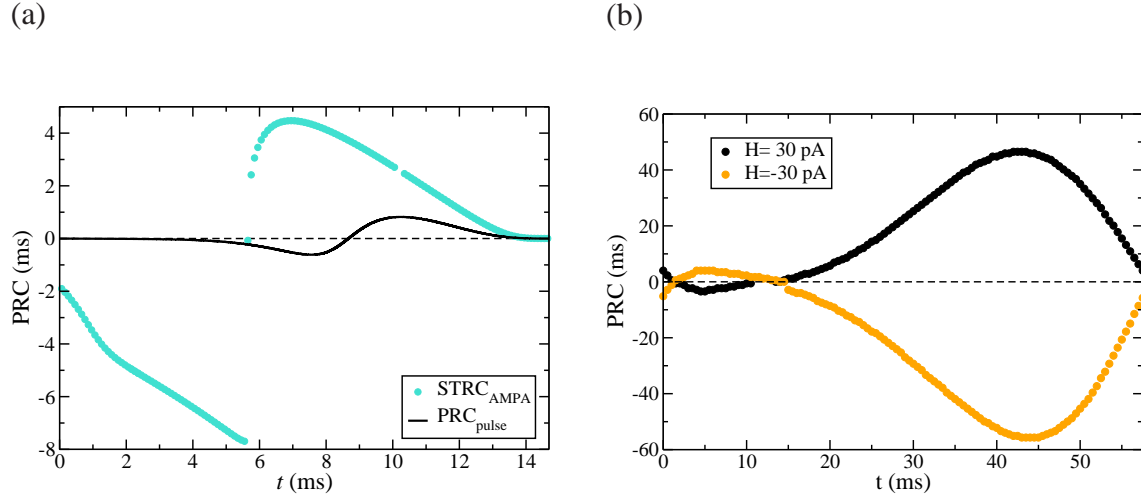


Figure 3.7: Other phase response curves. (a) Spike time repose curve  $STRC_{AMPA}$  for the standard HH model with AMPA synapse ( $g_{MS} = 10$  nS) and PRC calculated using a quadratic pulse of  $H = 30$  pA and  $L = 2$  ms. (b) Phase response curve  $PRC_{pulse}$  for the modified HH receiving quadratic pulse stimulus:  $L = 2$  ms and  $H = 30$  pA (black circles) and  $H = -30$  pA (orange circles).



## Neuronal populations

Synchronization by neural oscillation has been extensively studied along the years. It has been hypothesized to be relevant to issues such as the binding problem [65], temporal coding [104], deployment of spatial attention [105], higher cognitive functions [63], and many others (for a recent review, see [106]). Particularly, coherent oscillations are also useful to infer the functional connection between different areas in the cortex during multisensory integration, sensorymotor decision-making, and top-down visual attention [107].

A canonical mechanism to generate oscillatory activity in neuronal networks with chemical synapses is the feedback loop through excitatory-inhibitory connections [63]. We were wondering if the inhibitory feedback loop can regulate the time delay between the oscillations leading the system to an anticipated synchronization regime. In other words, is it possible that a model of synchronized neuronal population exhibits AS? Are the results from 3-neuron motifs extensible to much larger neuronal networks? In order to address these questions we investigate *in silico* the emergence of AS between neuronal populations.

We take into account realistic brain features, such as the proportion of excitatory and inhibitory neurons, variability in the neuronal dynamics (spiking, bursting etc), noise, baseline firing rates and global topological motifs, with parameters chosen so as to mimic cortical sub-networks. To simplify the modeling of the asymmetry necessary in previous studies of AS and the delayed feedback, our model focuses on cortico-cortical couplings in a Master-Slave-Interneuron (MSI) configuration. As shown in Fig. 4.1, each node is a population of neurons: the Master population (M), the Slave population (S) and the Interneuron population (I). By construction the S neuronal population exerts no influence on M. As we will show, however, the inhibitory loop mediated by the interneurons in I can suffice to make M lag behind S, indicating the existence of an AS regime. All the links in Fig. 4.1 are unidirectional chemical synapses.

### 4.1 Modeling collective oscillations in large-scale systems

Our populations are composed of Izhikevich neurons [51] whose parameters are chosen randomly from a predefined ranged and then kept constant throughout the simulations. The parameters of the model are chosen so as to reproduce typical firing patterns observed in different types of neuron in the cortex. Each excitatory neuron can belong to one of the following classes: regular spikes, bursting or chattering, with a well-defined probability. Similarly, inhibitory neurons can be fast-spiking or low-threshold spiking. Altogether the neuronal population described here reproduces electrophysiological results both at the neuronal scale and for large-scale networks [94].

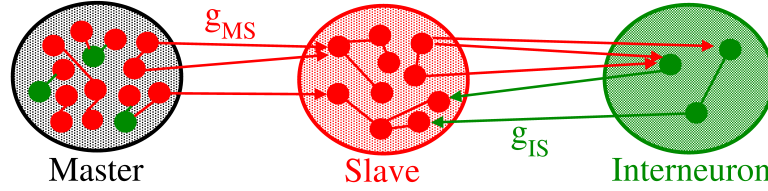


Figure 4.1: Three large-scale networks coupled in a Master-Slave-Interneuron (MSI) configuration. Excitatory (inhibitory) neurons represented by red (green) units. Two of the networks are coupled in a master-slave configuration, with an inhibitory feedback loop mediated by the interneuron network. Besides the excitatory synapses from neurons belonging to the Master (M) population, the neurons from the Slave (S) population also receive an inhibitory synapses from the neurons in the interneuron population (I). All synapses are unidirectional.

Each neuron receives an independent Poisson train of excitatory post-synaptic currents to mimic the activity of all other neurons in the brain that we are not modeling. Excitatory (inhibitory) neurons send excitatory (inhibitory) synapses mediated by AMPA ( $GABA_A$ ), both modeled by first-order kinetics [58]. In each population the neurons are synaptically connected with 10% of randomly selected neurons of the same population (sparse connectivity).

#### 4.1.1 Cortico-cortical network

In order to investigate the synchronization properties between populations representing cortical regions we build 3 populations composed of hundreds of neurons described by the following equations [51]:

$$\frac{dv}{dt} = 0.04v^2 + 5v + 140 - u + \sum_x I_x, \quad (4.1)$$

$$\frac{du}{dt} = a(bv - u), \quad (4.2)$$

where  $v$  is the membrane potential and  $u$  the recovery variable which accounts for activation (inactivation) of  $K^+$  ( $Na^+$ ) ionic currents.  $I_x$  are the currents provided by the interaction with other neurons and external inputs. If  $v \geq 30$  mV, then  $v$  is reset to  $c$  and  $u$  to  $u + d$ . For each excitatory neuron the dimensionless parameters are:  $(a,b) = (0.02,0.2)$  and  $(c,d) = (-65,8) + (15, -6)\sigma^2$ . Similarly for each inhibitory neuron:  $(a,b) = (0.02,0.25) + (0.08, -0.05)\sigma$  and  $(c,d) = (-65,2)$ , where  $\sigma$  is a random variable uniformly distributed on the interval  $[0,1]$ .

The connections between neurons are assumed to be fast unidirectional excitatory and inhibitory chemical synapses mediated by AMPA (A) and  $GABA_A$  (G). The synaptic currents are given by

$$I_x = g_x r_x (v - E_x), \quad (4.3)$$

where  $x = A, G$ ,  $E_A = 0$  mV,  $E_G = -65$  mV and  $r_x$  is the fraction of bound synaptic receptors

whose dynamics is given by:

$$\tau_x \frac{dr_x}{dt} = -r_x + \sum_k \delta(t - t_k), \quad (4.4)$$

where the summation over  $k$  stands for presynaptic spikes at times  $t_k$ . Moreover, the time decays are  $\tau_A = 5.26$  ms,  $\tau_G = 5.6$  ms [108]. Each neuron is subject to an independent noisy spike train described by a Poisson distribution with rate  $R$ . The input mimics excitatory synapses (each with conductance  $g_E = 0.5$  nS) from  $n$  pre synaptic neurons external to the population, each spiking with a Poisson rate  $R$  which, together with a constant external current  $I_c$ , determines the main frequency of mean membrane potential of each population. Unless otherwise stated, we have employed  $R = 2400$  Hz and  $I_c = 0$ . We use Euler's method for numerical integration with a time step of 0.05 ms.

The Master population is composed of 500 neurons (80% excitatory, 20% inhibitory), each one receiving 50 synapses (sparse connectivity) from randomly selected neighbors in the same population. The mean membrane potential  $\langle V \rangle$  (mV) of this population oscillates with a mean period  $T_M \approx 130$  ms which strongly depends on the Poisson rate  $R$ . In order to obtain higher oscillations frequency we increase the Poisson rate.

The Slave population is composed of 400 excitatory neurons, each one receiving 40 synapses from neighbor neurons belonging to the same population, 20 synapses from excitatory neurons from the Master population (which characterizes the master-slave configuration) and 10 synapses from the interneurons in the third population (which play the role of the delayed self-feedback responsible for AS). To close the inhibitory loop, the Interneuron population has 100 inhibitory neurons, each one receiving 10 synapses from randomly selected inhibitory neurons from I and 40 excitatory synapses from randomly selected neurons belonging to S.

Our main control parameters will be the following maximal synaptic conductances:  $g_{MS}$  in the excitatory M-S coupling and  $g_{IS}$  in the inhibitory I-S coupling (see Fig. 4.1). Unless otherwise stated, all other synaptic couplings remain fixed (see Table 4.1 for details).

We can regard the Slave and Interneuron populations as corresponding either to well separated regions (see Fig. 4.1) or to sub-populations of a larger network that is very similar to the Master population. To stress this possibility, in the modified motif shown in Fig. 4.9(a), described in the Section 4.4 everything remains as before but each neuron in the Interneuron population receives synapses from 10 randomly selected excitatory neurons in the Master population. To mimic the Slave-Interneuron population (SI) as a cortical region driven by the Master population, the conductance of the synapses from neurons in M to both excitatory and inhibitory neurons in SI are the same  $g_{MS}$ . The results obtained with both motifs are qualitative similar and the later motif will be useful to compare our model with experimental data in the next chapter.

### 4.1.2 Defining time delay in the model

Since the mean membrane potential  $\langle V \rangle$  is significantly noisy in time, it is hard to precisely determine its maximum value in each cycle. In order to solve this issue, we use a sliding window (typically  $\Delta t = 5$  ms) to calculate  $\langle \bar{V} \rangle$  from  $\langle V \rangle$  (see Fig. 4.3). It makes the signal

parameters	cortico-cortical	range varied
$n1$	500 (80% exc. / 20% inh.)	-
$n2$	400 (100% excitatory)	-
$n3$	100 (100% inhibitory)	-
$g_{MS}$	0.5	0 - 3
$g_{SI}$	0.5	-
$g_{IS}$	4(AS) / 8(DS)	0 - 25
$g_{SM}$	0.0	0 - 1
internal $g_{AMPA}$	0.5	-
internal $g_{GABA_A}$	4	7.5
external noise $g_{AMPA}$	0.5	-
Poisson rate (Hz) $R$	2400	2000 - 4800
# internal connections $M$	50	-
# internal connections $S$	40	-
# internal connections $I$	10	-
# external connections $MS$	20	5 - 20
# external connections $SI$	40	-
# external connections $IS$	10	-
# external connections $SM$	0	20

Table 4.1: The model parameters. Standard values employed in the MSI motif.

smooth enough that we can determine in each period the time  $t_i^x$  in which  $\langle \bar{V}^x \rangle$  has a maximum value ( $x = M, S, I$  indexes the population and  $i$  the period). Since each neuron is subjected to an independent Poisson input, the oscillation period of each population is not constant. Now we can define the period of a given population in each cycle:

$$T_i^x \equiv t_{i+1}^x - t_i^x. \quad (4.5)$$

For sufficiently long time series we calculate the mean period  $T_x$  and its standard deviation. The frequency of oscillation  $f_x$  can be calculated either by the inversion of the mean period or by the Fourier transform of  $\langle V^x \rangle$ . In a similar way we calculate the time delay in each cycle

$$\tau_i = t_i^S - t_i^M. \quad (4.6)$$

Then we calculate  $\tau$  as the mean value of  $\tau_i$  and  $\sigma_\tau$  as its standard deviation. It is also possible to plot the return map  $\tau_i$  versus  $\tau_{i-1}$  (see Fig. 4.5). In all those calculations we discard the transient time. If  $T_M \approx T_S$  and the  $\tau$  is independent of the initial conditions, the system is in a phase-locking regime. Another way to characterize the regime is by the cross-correlation function between the LFP of the M and S populations, shown in Fig. 4.6(a), which is calculated as:

$$C(V_M, V_S, t) = \frac{(\sum V_M^i - \bar{V}_M)(\sum V_S^{i+t} - \bar{V}_S)}{\sqrt{\sum (V_M^i - \bar{V}_M)^2 \sum (V_S^i - \bar{V}_S)^2}} \quad (4.7)$$

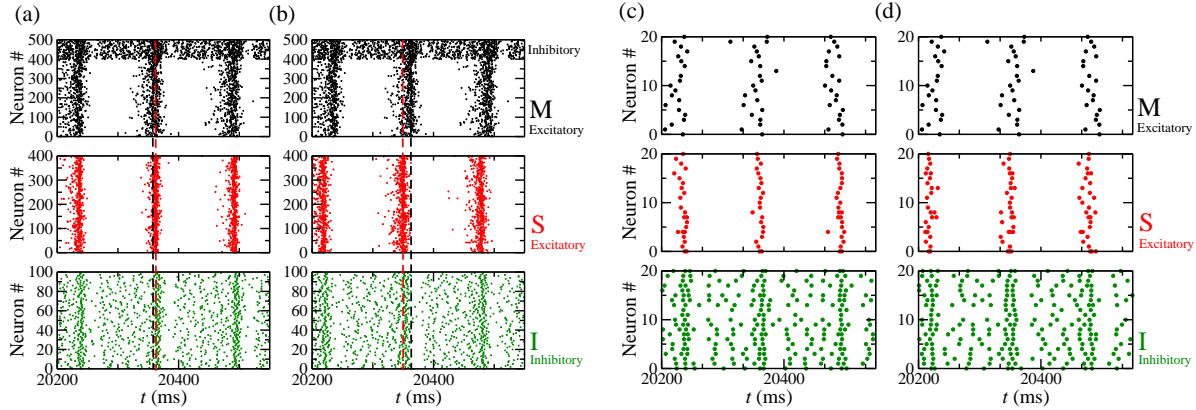


Figure 4.2: Raster plots of each population in delayed synchronization (DS) and anticipated synchronization (AS) regimes. The horizontal axis is time and the vertical axis is the index of the neurons in the Master (upper), Slave (middle) and Interneuron (lower) populations. Each point represents an action potential. The only difference between the two simulations is the maximal conductance  $g_{IS}$  of the (inhibitory) synapses from the Interneuron population to the Slave population:  $g_{IS} = 8$  nS [(a) and (c)] and  $g_{IS} = 4$  nS [(b) and (d)]. All neurons in the I population are inhibitory, as well as the last 100 neurons in the M population (index 400 to 499). All others are excitatory. (c) and (d) Zoom-in versions of (a) and (b), displaying the difference in the firing patterns of individual neurons in the DS and AS regimes.

## 4.2 How to characterize AS?

The raster plots in Figs. 4.2 show that the majority of spikes in each population happens in preferred time intervals. The recurrence of these time intervals (darker regions) is an evidence of the typical oscillatory behavior of the 3 coupled populations. Even though the inhibitory neurons individually fire with higher frequency than the excitatory ones, collectively they maintain the typical oscillatory pattern in which the density of spikes is larger in the preferred time intervals. Note that the darker region in the Interneuron population always occurs shortly after the one in the Slave population. Figures 4.2(c) and (d) show that, despite the collective oscillatory behavior, each neuron in a population can fire quite irregularly.

The set of parameters used in Fig. 4.2 are the typical ones, shown in Table 4.1, except that in Fig. 4.2(a) and (c)  $g_{IS} = 8$  nS while in Fig. 4.2(b) and (d)  $g_{IS} = 4$  nS. The main observable difference between the two situations is that the darker regions of the M population occur before (after) the ones in the S population in Fig. 4.2(a) (Fig. 4.2(b)). It means that in one case (Fig. 4.2(a)) almost all spikes in the S population occur right after almost all synaptic currents from the M population have arrived. This often leads to the S neurons spiking in a narrow interval, as shown in Fig. 4.2(c). As the inhibitory  $g_{IS}$  coupling is decreased (Fig. 4.2(b)), the S neurons mostly fire before the M neurons (and, as shown in Fig. 4.2(d), the deviation of the mean in the S firing is larger). In particular, each neuron from M and S may fire more than once in each collective oscillatory cycle, which occurs more often for neurons from S in the AS regime (see Fig. 4.2(d)). Altogether, the data provides a qualitative evidence of the existence of both DS and AS regimes in this system.

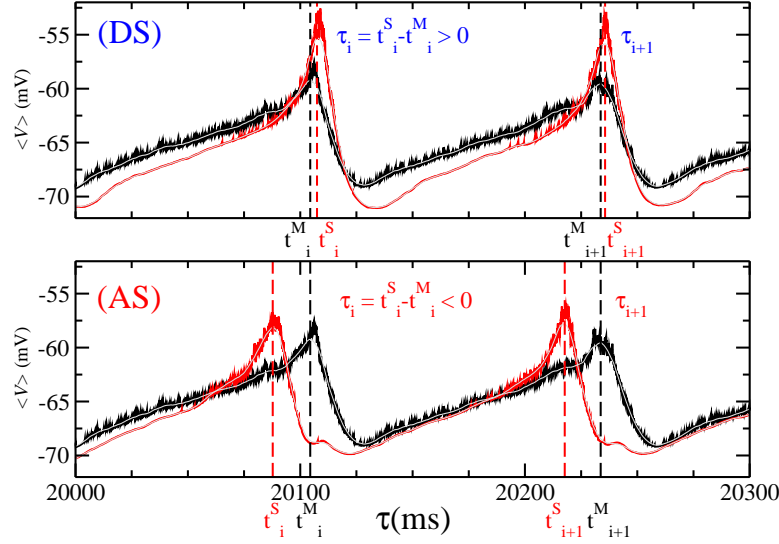


Figure 4.3: Mean membrane potential  $\langle V \rangle$  of the Master (black) and the Slave (red) populations in the DS (top) and AS (bottom) regimes. Gray lines are the filtered mean membrane potentials  $\langle V_x \rangle$ . Their local maximal values determine  $t_i^x$ ,  $x = M, S$  used to calculate the time delay  $\tau_i$  in the  $i$ -th cycle.

#### 4.2.1 LFP scale

In order to characterize the DS and AS regimes we need to quantify the relative spiking times of the M and S populations along a large time series for different parameter sets. A reasonable way to start this analysis is to plot the mean  $\langle V \rangle$  of the membrane potential of all neurons in each population as a function of time.  $\langle V \rangle$  can be thought of as a crude approximation of a local field potential (LFP) signal. As expected from the raster plots,  $\langle V \rangle$  oscillates and has sharp peaks, as shown in Fig. 4.3.

Using the previous definition of the time delay  $\tau$  and the mean period  $T_x$  we will focus on the wide regions of parameter space where the M and S populations have the same average period ( $T_M \simeq T_S$ ). In this case, the time delay fluctuates around a mean value  $\tau \equiv \langle \tau_i \rangle$ , which characterizes a phase-locking regime between the M and S populations. By definition, if  $\tau > 0$  the system is in the DS regime (see Fig. 4.3(a)), whereas if  $\tau < 0$  the system is in the AS regime (see Fig. 4.3(b)).  $\tau$  turns out to be a well behaved and often non-monotonic function of the inhibitory synaptic conductance  $g_{IS}$ , as shown in Fig. 4.4(a) and (b), as well as of the excitatory synaptic conductance  $g_{MS}$ , as shown in Fig. 4.4(c) and (d). The transition from DS to AS is smooth and continuous. When we reduce the number of external links from the Master to the Slave population (for example from 20 per neuron to 5) we observe qualitatively similar results but the interval of inhibitory conductances in which AS occurs decreases.

Moreover, we can use the return map  $\tau_i$  versus  $\tau_{i-1}$  to characterize different regimes. Fig. 4.5 shows that besides the DS and AS regimes, for small values of synaptic conductances the system may exhibit two other regimes. As in the 3-neuron case there is a phase-drift (PD)

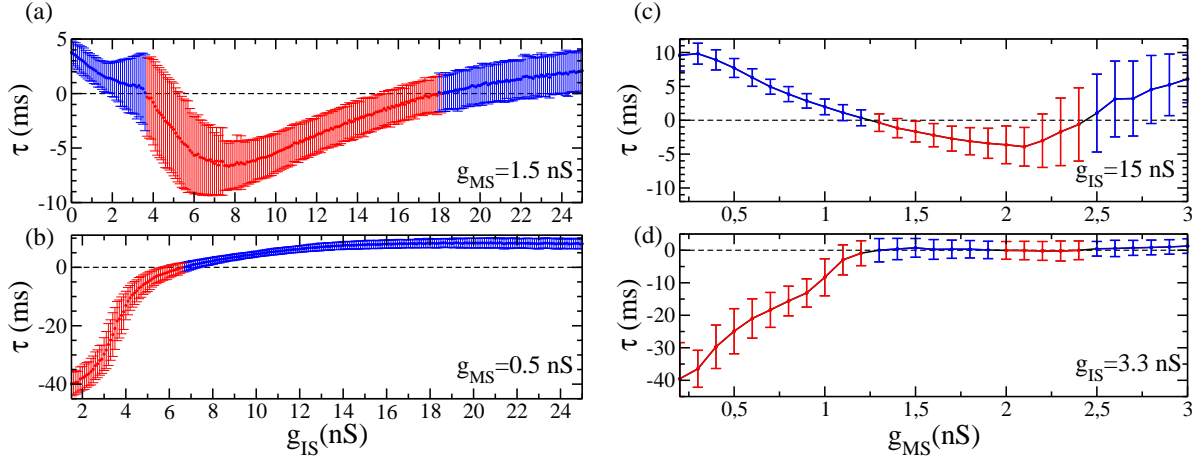


Figure 4.4: The mean time delay  $\tau$  versus the inhibitory synaptic conductances  $g_{IS}$  from I to S population.  $\tau = 0$  is where the transition from AS (red) to DS (blue) regime occurs. Depending on the strength of  $g_{MS}$  the system exhibits either DS or AS regimes.  $\tau$  as a function of  $g_{IS}$  for (a)  $g_{MS} = 1.5$  nS and (b)  $g_{MS} = 0.5$  nS.  $\tau$  as a function of  $g_{MS}$  for (c)  $g_{IS} = 15$  nS and (d)  $g_{IS} = 3.3$  nS.

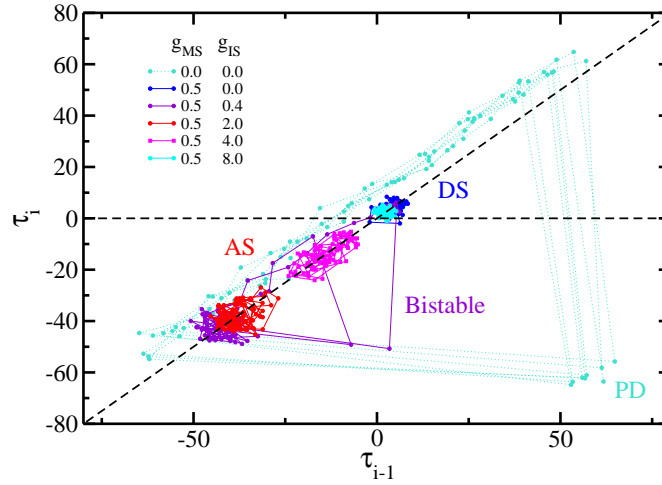


Figure 4.5: Return map  $\tau_i$  versus  $\tau_{i-1}$ . Four different regimes: AS, DS, phase drift (PD) and bistable regime (for small values of inhibitory conductances). The system alternates between AS and DS with a well defined value of  $\tau$ .

region in which it is senseless to determine the mean time delay. In this regime  $T_M \neq T_S$ . Since  $g_{MS} = g_{IS} = 0$ , the Slave population is totally isolated and there is no inhibition acting on it. Differently from what happens in the 3-neuron motif, for  $g_{IS} = 0$  the Master and the Slave are not identical. Besides, in the large-scale network, between the phase-drift and the phase-locking regimes there is a bistable regime. The bistability is characterized by the coexistence of well characterized DS and AS regimes which alternate from time to time (see Fig. 4.5). Several studies have suggested that multi-stability are very important in neural dynamics. It might

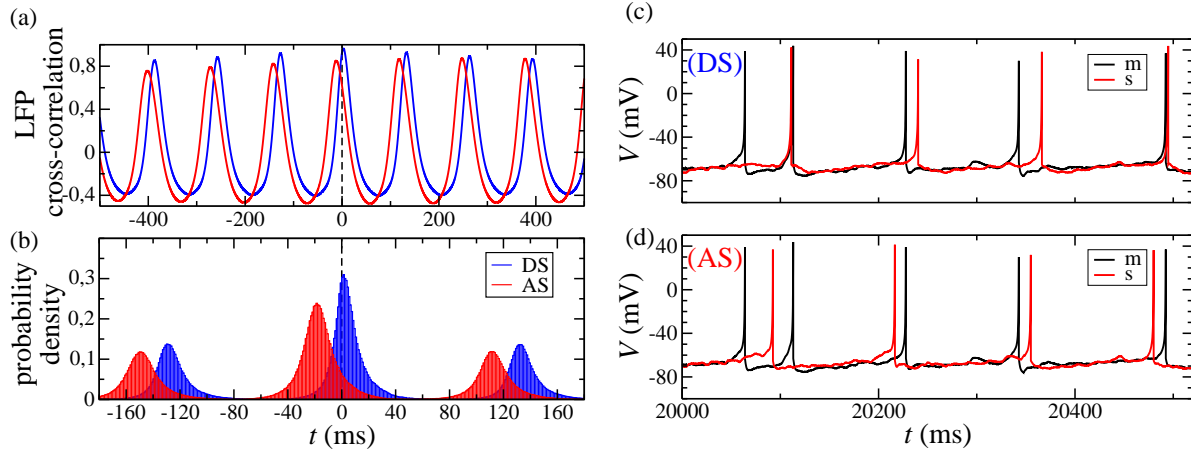


Figure 4.6: Characterizing AS in large and small scales. (a) Cross-correlation between the mean membrane potential  $\langle V \rangle$  of the Master and the Slave populations for different regimes. The time at which the cross-correlation function attains its maximum value is approximately the mean time delay  $\tau$  between the M and S populations. (b) Histogram of the time delay  $\tau^{MS}$  between the spikes of all coupled pairs whose presynaptic neurons are in the M population and postsynaptic neurons are in the S population. (c) and (d) Typical spiking activity of a presynaptic neuron from the M population (black) and a postsynaptic neuron from the S population (red) in two different regimes: DS (c) and AS (d).

underlie the switching between different perceptions or behaviors [109, 110, 111, 112, 113]. Transitions between many possible attractors of the neural circuits may occur, for example, under the influence of a cognitive driving [114, 115, 116]. However, from now on we will deal just with the regime where either AS or DS is stable.

Still at the LFP scale, another characterization of both the periodicity of oscillations and the existence of DS and AS can be made via the cross-correlation function between the mean membrane potentials of the M and S populations, respectively  $\langle V_M(t) \rangle$  and  $\langle V_S(t) \rangle$ . The correlation curves shown in Fig. 4.6(a) corroborate the results obtained by the direct measurement of  $\tau$ , displaying a peak with positive time delay in the DS regime and negative time delay in the AS regime. The cross-correlations were calculated using Eq. 4.7.

## 4.2.2 Neuronal scale

Although the phase-locking is a collective phenomenon, the DS and AS regimes are also evident at the neuronal scale. The histograms in Fig. 4.6(b) show the probability density of spike time intervals  $\tau^{MS}$  between a spike from neuron in S and its respective presynaptic spikes from neurons in M. Both the peak and the mean of the distribution have positive values in the DS regime, and negative values in the AS regime. The second peak of the histogram is comparatively smaller than the first. It means that in the synaptic scale, AS is a local and non-periodic phenomenon.



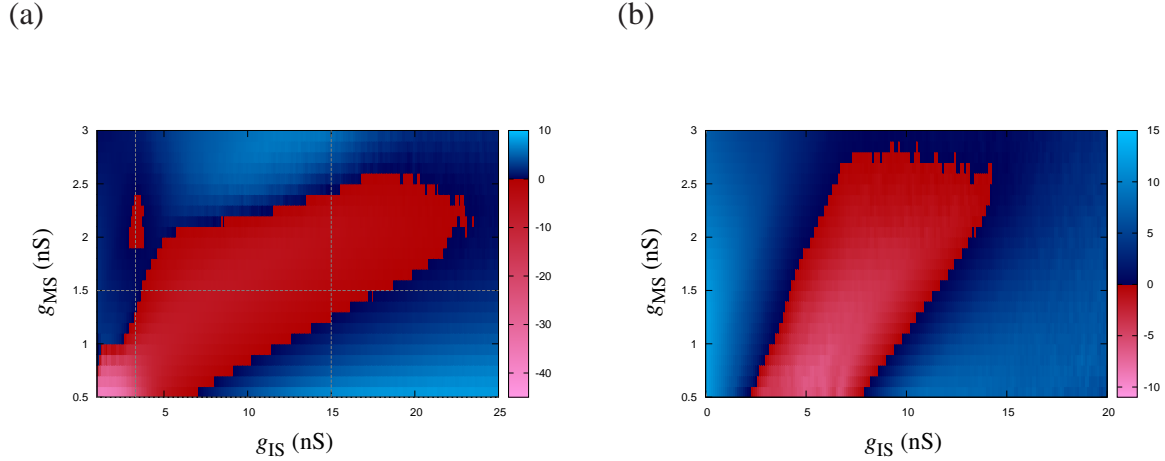


Figure 4.7: Mean time delay  $\tau$  (right bar) in the  $(g_{IS}, g_{MS})$  parameter space. The blue region corresponds to the DS regime and the red one to the AS. (a) The Poisson rate is  $R = 2400$  Hz and the population firing rates  $f_M \approx f_S \approx 7.7$  Hz. (b) The Poisson rate is  $R = 4800$  Hz and  $f_M \approx f_S \approx 14.7$  Hz. The horizontal (vertical) dashed lines in (a) corresponds to the  $t$  versus  $g_{IS}$  ( $g_{MS}$ ) curves shown in Fig. 4.4(a) and (b) (Fig. 4.4(c) and (d)).

Figures 4.6(c) and (d) show examples of spiking activity of neurons from the M and S populations. In both cases, we chose two neurons which are a pre-post synaptic pair. In both DS and AS regimes, pairs of coupled neurons do not maintain the same time delay between their spikes in every cycle. Even though the order of the spikes can change (pre-post to post-pre spikes), on average there are more pre-post spikes in DS and more post-pre spikes in AS. That is what allows us to characterize the AS and DS regimes looking at the peak of the histogram in Fig. 4.6(b).

### 4.3 Robustness in parameter space

Since we showed that the different ways to characterize the AS and DS are essentially equivalent, in the following we choose to employ  $\tau$  as our standard measure. To explore the parameter space, we used the values given in the first column of Table 4.1, except for  $g_{IS}$  and  $g_{MS}$ , which in Fig. 4.7 are varied along the horizontal and vertical axes respectively.

In Fig. 4.7(a) we display a two-dimensional projection of the parameter space of our model. The two different regimes (DS in blue and AS in red) are distributed in large contiguous regions of parameters. The transitions AS-DS are smooth. The horizontal (vertical) dashed lines in Fig. 4.7(a) corresponds to the  $\tau$  vs  $g_{IS}$  ( $g_{MS}$ ) curves shown in Fig. 4.4(a) and (b) (Fig. 4.4(c) and (d)). For the chosen parameters, the populations collective oscillate at an average frequency  $f \approx 7.7$  Hz ( $T_M \approx 130$  ms).

The results are also robust with respect to the baseline firing rate of the neurons. In Fig. 4.7(b) we show the results for a higher input Poisson rate ( $R = 4800$  Hz), which leads to higher network oscillation frequencies:  $f \approx 14.7$  Hz ( $T_M \approx 68$  ms). For this higher Poisson

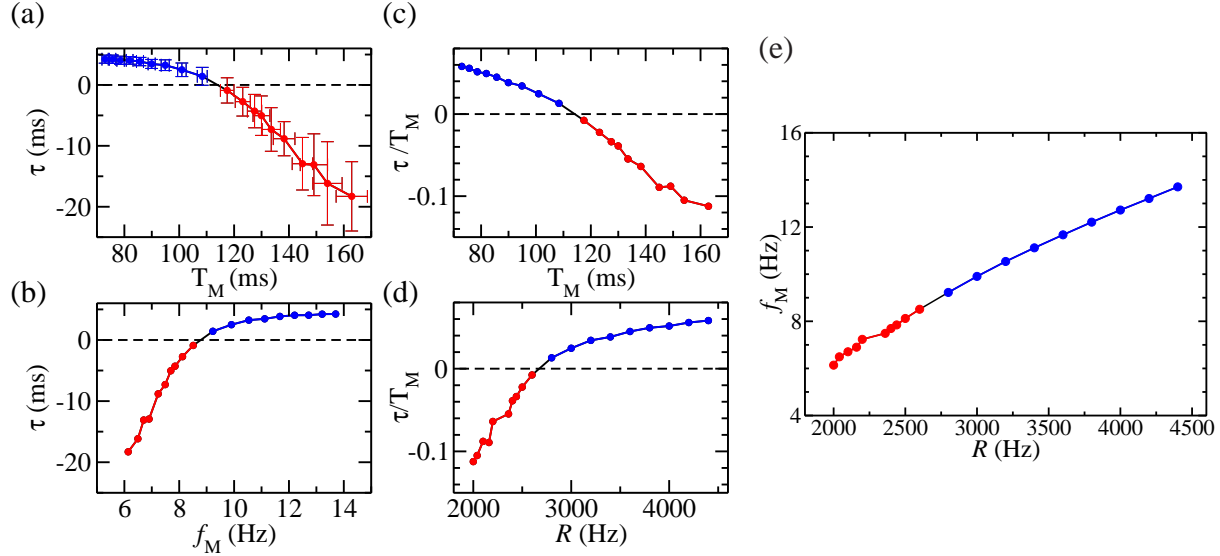


Figure 4.8:  $\tau$  is robust against noise. We choose an AS regime with all the parameters given in Table 4.1 (except  $g_{IS} = 5$  nS) and varied the Poisson rate  $R$ . As a consequence, the mean period (and frequency) of the Master also varied. We plot the same set of points in five different ways: (a)  $\tau$  as a function of the mean period of the Master  $T_M$  and (b) its mean frequency  $f_M = 1/T_M$ . (c)  $\tau$  normalized to  $T_M$  as a function  $T_M$  and (d) as a function of the Poisson rate  $R$ . (e) Measured mean frequency for each chosen Poisson rate.

rate, the inhibitory conductances inside each population needs to be greater (internal  $g_{GABA_A} > 6.5$  nS). The phase diagram in Fig. 4.7(b) is qualitatively the same as in Fig. 4.7(a) but  $g_{GABA_A} = 7.5$  nS. Since the period of the collective oscillations is shorter for Fig. 4.7(b), so it is the maximum absolute value of the anticipation time  $\tau$  (compare the color-coded values of  $\tau$ ).

Fig. 4.8 shows the time delay  $\tau$  and its normalized value  $\tau/T_M$  as the Poisson rate  $R$  is varied. Beginning from the AS regime ( $g_{MS} = 0.5$  and  $g_{IS} = 5$  nS in Fig. 4.7(a)),  $R$  is increased from 2000 Hz to 4400 Hz. All other parameters are in Table 4.1. It is worth mentioning that it is possible to find an AS regime for  $R > 2800$  Hz (an example is shown in Fig. 4.7(b)). However, it is necessary to change other parameters such as internal synaptic conductances.

## 4.4 Modified motifs

### 4.4.1 Slave-Interneuron as one cortical population

Our results are also robust with respect to changes in the topology of the system. In Fig. 4.9(a) we show a modified version of the MSI motif of Fig. 4.1, where the M population also projects its excitatory synapses onto the I population. Arguably, this could better mimic an asymmetrical mesoscale interaction between two cortical populations as the ones assessed in experiments with macaque-monkeys [70, 117] (more details in the next chapter). In the case of Fig. 4.9(a), the S and I populations can be considered as the excitatory and inhibitory sub-

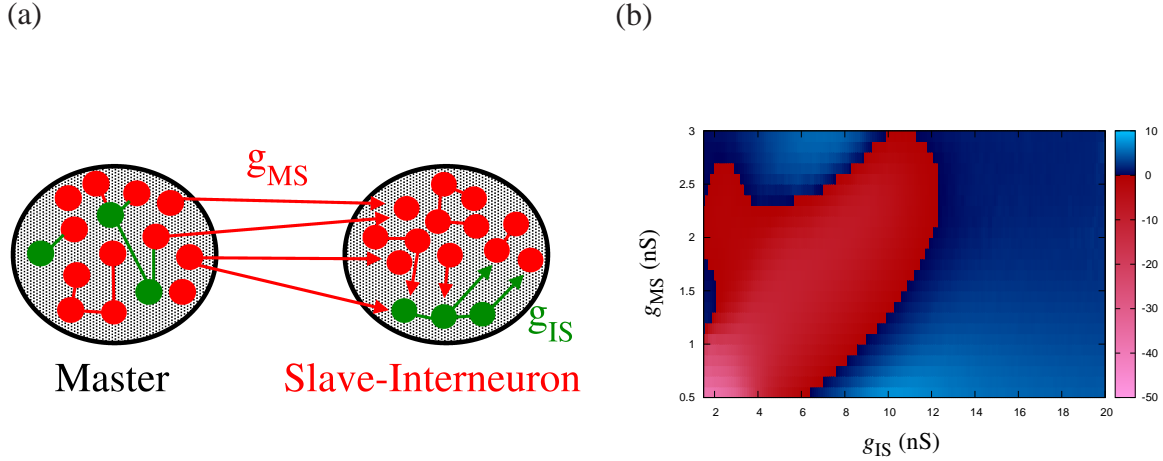


Figure 4.9: A modified MSI motif also exhibits DS and AS. a) Similar to the motif in Fig. 4.1 but with extra excitatory connections from neuron in the M populations to neurons in the I population. b) Mean time delay  $\tau$  (right bar) in the  $(g_{IS}, g_{MS})$  parameter space. The Poisson rate is  $R = 2400$  Hz and the population firing rates are  $f_M \approx f_S \approx 7.7$  Hz.

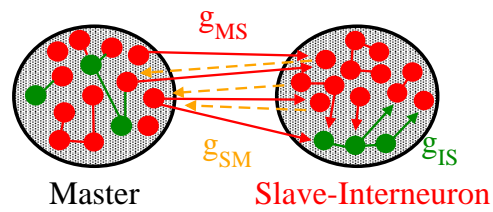
population of a larger Slave-Interneuron (SI) population that is very similar to M. Figure 4.9(b) shows a phase diagram for this situation which is similar to those of the preceding figures. The time delay in each cycle is defined as  $\tau_i = t_i^{SI} - t_i^M$ , where  $t_i^{SI}$  is the peak in the mean membrane potential of all neurons in the SI population.

#### 4.4.2 Bidirectional coupling

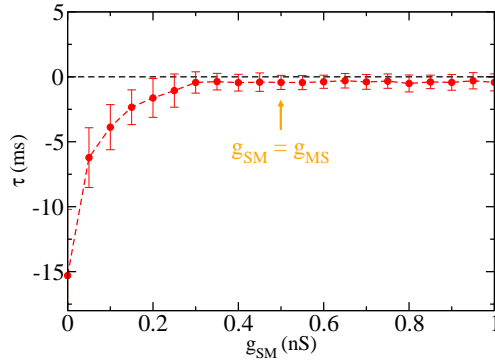
Although the structural (i.e. anatomical) connectivity between cortical areas is often bidirectional [117], brain functions typically require the control of inter-areal interactions on time-scales faster than synaptic changes. Particularly, functional and effective connectivity [62] must be reconfigurable even when the underlying structural connectivity is fixed. First, different tasks require the activation of different pathways. Second, we live in a changing environment. However, a complete understanding of how interareal phase coherence can be flexibly regulated at the circuit level is still unknown [109].

To ensure that the AS regime is not specific to cortical ensembles with unidirectional connections, we show its robustness in the presence of excitatory synaptic feedback from the Slave to the Master population. In this subsection, each neuron in the M population receives synapses from 20 randomly chosen excitatory neurons of the SI population. Fig. 4.10(a) shows this schematic configuration. All other parameters are in Table 4.1 and  $g_{MS} = 4$  nS to ensure that for  $g_{SM} = 0$  nS the system is in the AS regime. For small values of the excitatory feedback conductance,  $g_{SM} < g_{MS}/2$ , the AS regime persists (see Fig. 4.10(b)). The time delay between the two population increases with  $g_{SM}$  and the system eventually goes to a near zero-lag regime [108]. Moreover, the cross-correlation in Fig. 4.10(c) corroborates the existence of two different regimes.

(a)



(b)



(c)

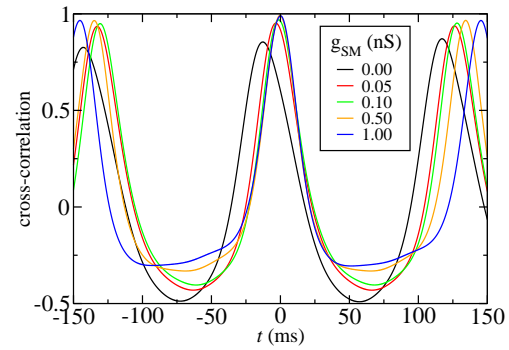


Figure 4.10: Effect of the synapses from the Slave population to the Master. (a)  $\tau$  as a function of the excitatory feedback as we varied the synaptic conductance  $g_{SM}$  for a fixed value of  $g_{MS} = 0.5$  nS. (b) Cross-correlation between the mean membrane potential of M and SI.

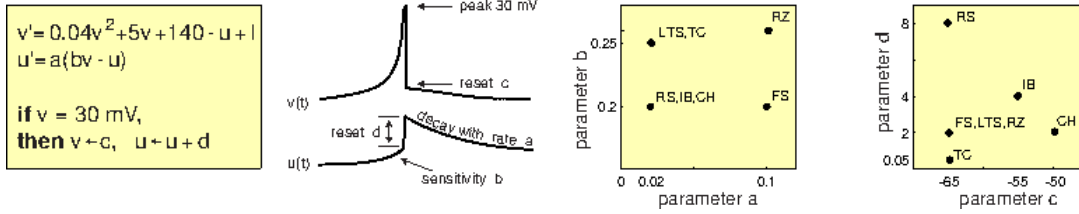


Figure 4.11: The parameters of the Izhikevich neuron model determines the different firing patterns of the neurons (shown in Fig. 1.2). For fixed  $a = 0.02$  and  $b = 0.2$  the response of the neuron to an applied constant current depend on the values of  $c$  and  $d$ . For  $(c,d) = (-65,8)$  the neuron is a regular spiking (RS), for  $(c,d) = (-55,4)$  it is an intrinsically bursting (IB), for  $(c,d) = (-50,2)$  it is a chattering (CH). Electronic version of the figure and reproduction permissions are freely available at [www.izhikevich.org](http://www.izhikevich.org).

## 4.5 Changing neuronal variability of the Slave

Neuronal synchronization, which might play an important role in the neural coding, provides a potential spike-based code (i.e. depending on spike-timing differences) that putatively coexists with a rate code (i.e. based on the neuronal firing rate) [104]. We suggest that AS can open a new and unexplored avenue to improve the computational power of spike-based code. Particularly, Brette [104] has proposed that heterogeneity is essential for the efficiency of computing with neural synchrony. He showed that in a heterogeneous neural population model, synchrony receptive field could be used as an additional information for computation. Therefore, we show that in our model, the AS regime is not only robust against neuronal variability but it is also a smooth function of the proportion of different types of neurons.

Depending on the parameters  $a$ ,  $b$ ,  $c$  and  $d$  in the Izhikevich model (see Eq. 4.1) each neuron in the populations respond differently to a constant current. We characterize the type of neuron by its response. In Fig. 4.11 there is a detailed description of the kinds of neurons covered by the Izhikevich model that we use here. In the absence of a constant current in our model, but in the presence of synaptic currents, the behavior of a regular neuron for example, may be slightly different in each cycle. The oscillatory activity of a population may change depending on the proportion of each kind of neuron.

By Voss's definition of AS the two dynamical systems need to be identical (see Eq. 1.1). Here we aim at verifying if small changes in the Slave population still leads to AS regimes. Furthermore, in Fig. 4.12 we show that continuous changes in the variability of the neurons from the Slave population produce continuous changes in the time delay. Particularly, if we want to simulate cortico-thalamic interactions we would like the Slave (thalamus) to have more bursting neurons than the Master (cortex).

In this section we redefine the parameters  $c$  and  $d$  from Eq. 4.1 as:

$$\begin{aligned} c &= -55 - x + (5 + x)\sigma_1^2 - (10 - x)\sigma_2^2 \\ d &= 4 + y - (2 + y)\sigma_1^2 + (4 - y)\sigma_2^2. \end{aligned} \quad (4.8)$$

Both  $\sigma_1$  and  $\sigma_2$  are random variables uniformly distributed in the interval  $[0,1]$ . If we simultaneously vary  $x$  and  $y$ , keeping the relation  $y = 2x/5$ , the maximum values of  $c$  and  $d$  vary

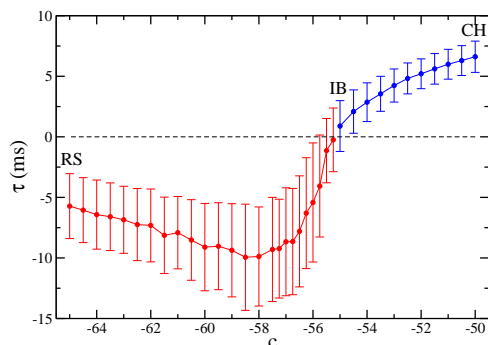


Figure 4.12: Neuronal variability. The time delay is a smooth function of the proportion of different kinds of neurons in the Slave.

along the line  $d = -6c/15 - 18$  which passes through RS, IB and CH in the plot at the right of Fig. 4.11. It means that, as before, there are all kind of neurons in each simulation. However, the distribution of the different types of neurons changes with  $c$ . For example, when  $c = -55$  (and consequently  $d = 4$ ) the majority of the neurons in the S population are IB neurons, but there are also RS and CH neurons in S. On the other hand, when  $c = -65$  and  $d = 8$  there are more RS than IB neuron in S and more IB than CH neurons. The effect of these changes in the time delay is shown in Fig. 4.12. It seems that the existence of more RS neurons facilitates AS. However, further investigation are necessary to distinguish whether changes in  $\tau$  are due to the amount of IB and CH neurons or due to the differences between M and S populations.

## 4.6 A toy model for the thalamus

The thalamus is a structure of the central nervous system (CNS) that could play an important role in the synchronization of cortical regions [118]. It is considered as the gateway to the neocortex, since all sensory signals, except for the olfactory inputs, reach the neocortex only after passing through a specific thalamic nuclei. The thalamus is believed to both process sensory information as well as relay it to the cerebral cortex, each of the primary sensory relay areas receives strong “back projections” from the cerebral cortex. Moreover, in the thalamus there are many inhibitory feedback loops due to reticular thalamic neurons (RTN) and thalamic interneurons [42]. Although the bidirectional connectivity pattern between thalamus and cortex [119, 120], here we investigated only the effects of unidirectional synapses from the cortex to the thalamus (the “back projections”). Since it is still possible to observe anticipatory oscillations in the presence of synapses from the Slave to the Master, our model can also be adapted to include the thalamic dynamical relaying [108, 118, 121].

In this section, we consider a similar motif to the one shown in Fig. 4.1, but the neurons in the Slave population are described by a different model of the neurons in M. The Master population is described as before (cortical like, see Section 4.1), but the Slave population mimics a thalamic region and is composed of 500 hundred neurons (80% excitatory 20% inhibitory).

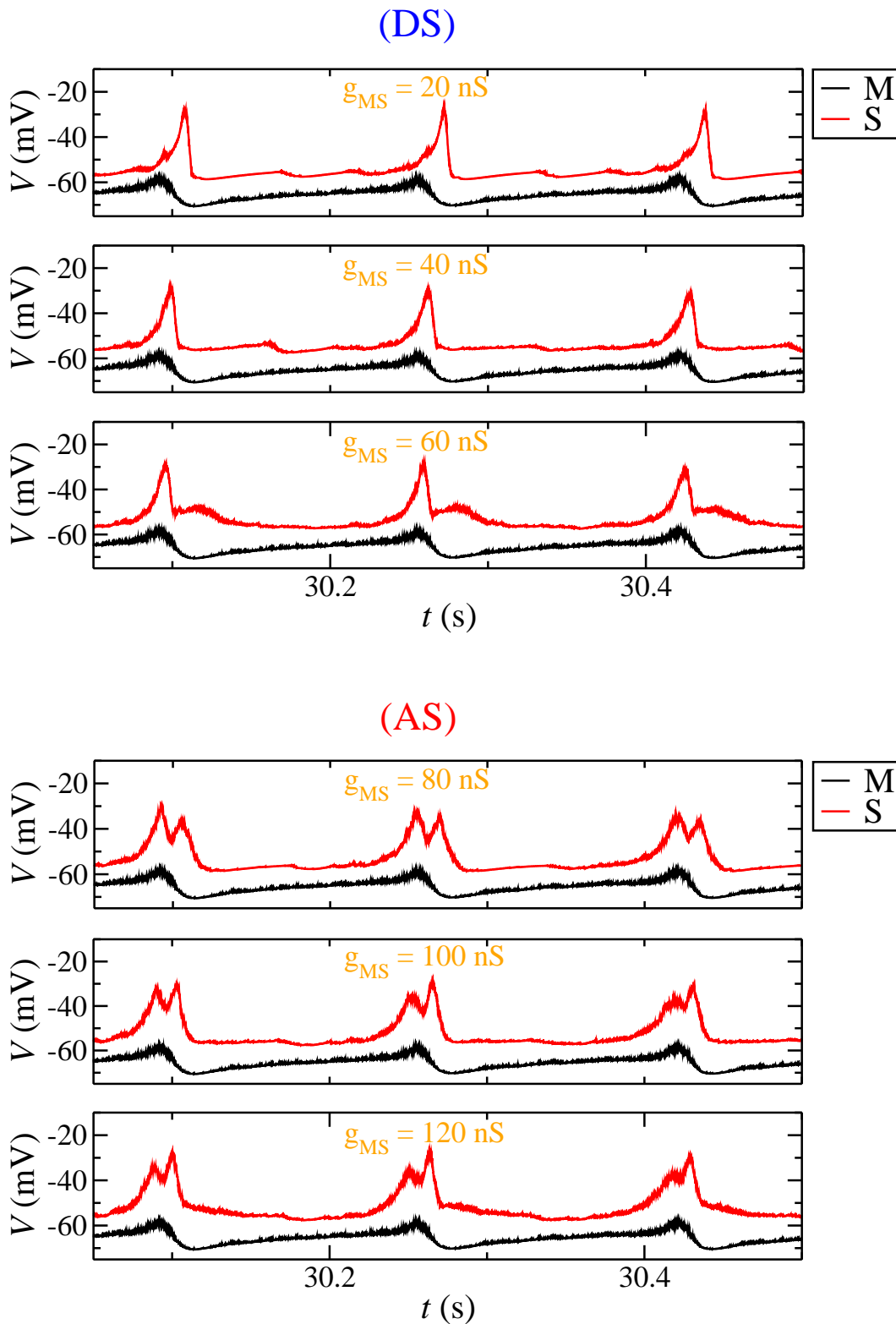


Figure 4.13: Time series for the Master cortical population and the Slave thalamic population for different values of  $g_{MS}$ . The AS regime is characterized by two peaks in the mean membrane potential of the Slave. The first peak anticipates de Master dynamics.

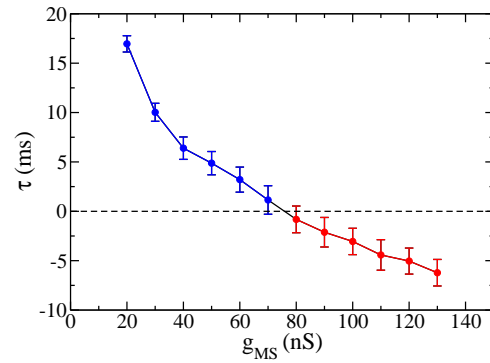


Figure 4.14: Time delay as a function of  $g_{MS}$ . In the presence of two peaks in the Slave, we define the time delay using the first peak.

[ht!]

parameters	thalamocortical	range varied
$n1$	500 (80% exc. / 20% inh.)	-
$n2$	500 (80% exc. / 20% inh.)	-
$n3$	100 (100% inhibitory)	-
$g_{MS}$	20 (DS) / 100 (AS)	5 - 150
$g_{SI}$	50	-
$g_{IS}$	50	-
$g_{SM}$	0	-
internal $g_{AMPA}$ M	0.5	-
internal $g_{AMPA}$ S	5	-
internal $g_{GABA_A}$ M	2	-
internal $g_{GABA_A}$ S and I	20	-
external noise $g_{AMPA}$ M	0.5	-
external noise $g_{AMPA}$ S and I	0.5	-
Poisson rate (Hz) $R$	2000	-
# internal connections $M$	50	-
# internal connections $S$	50	-
# internal connections $I$	10	-
# external connections $MS$	40	-
# external connections $SI$	50	-
# external connections $IS$	10	-
# external connections $SM$	0	-
external constant current $I_c$ in M	0	-
external constant current $I_c$ in S (exc)	42	-
external constant current $I_c$ in S (inh)	50	-
external constant current $I_c$ in I	50	-

Table 4.2: Parameters employed in the thalamocortical model.



The 400 excitatory neurons are described as the thalamocortical (TC) relay neurons [94]:

$$\begin{aligned} 200\dot{v} &= 1.6(v+60)(v+50) - u + \sum I_x \\ \dot{u} &= 0.01(b(v+65) - u), \end{aligned} \quad (4.9)$$

where  $b = 15$  if  $v \leq -65$  and  $b = 0$  otherwise. When  $v \geq 35 + 0.1u$  mV, then  $v$  is reset to  $-60 - 0.1u$  and  $u$  to  $u + 10$ . The 100 interneurons in the Slave population obey the thalamic interneurons equations:

$$\begin{aligned} 20\dot{v} &= 0.5(v+60)(v+50) - u + \sum I_x \\ \dot{u} &= 0.05(7(v+60) - u). \end{aligned} \quad (4.10)$$

When  $v \geq 20 - 0.08u$  mV, then  $v$  is reset to  $-65 + 0.08u$  and  $u$  to the minimum between  $u + 50$  and 530. The Interneuron population still has 100 inhibitory neurons but mimics the reticular thalamic nucleus (RTN) neurons:

$$\begin{aligned} 40\dot{v} &= 0.25(v+65)(v+45) - u + \sum I_x \\ \dot{u} &= 0.015(b(v+65) - u), \end{aligned} \quad (4.11)$$

where  $b = 10$  if  $v \leq -65$  and  $b = 2$  otherwise. When  $v \geq 0$  mV, then  $v$  is reset to  $-55$  and  $u$  to  $u + 50$ .

Each neuron receives an external constant current  $I_c$  and a Poisson input. The current applied to the excitatory neurons in the thalamus is  $I_c = 42$  pA, whereas in the thalamic inhibitory neurons and in the RTN  $I_c = 50$  pA. All parameters are shown in Table 4.2.

Since our model has two separated pools of inhibitory neurons, it is simpler to use  $g_{MS}$  as the control parameter. The time series of M and S are shown in Fig. 4.13 for different values of  $g_{MS}$ . The mean period and the mean time delay are calculated similarly to the previous sections. However, the existence of a second peak in the mean membrane potential of the thalamic population (see Fig. 4.13) is not considered in order to calculate  $\tau$ . Then, the time delay  $\tau$  is the difference between the time of the peak (or the first peak, if there are two) in mean membrane potential of S and the time of the closest peak in M. Using this definition, the model exhibits both AS ( $\tau < 0$ ) and DS ( $\tau > 0$ ) regimes. Fig. 4.14 shows the relation between  $\tau$  and  $g_{MS}$  which is qualitatively similar to that obtained with the cortico-cortical models (compare with Fig. 4.4(c) and (d)). Although this thalamocortical model would be more realistic in the presence of bidirectional connections, the existence of AS between two distinct M and S populations could play an important role in our understanding of the mechanisms underlying AS in oscillatory systems. However, further investigation is necessary to establish such mechanisms.

## 4.7 Stability analysis of phase-locking regimes between neuronal populations

In this section we simulate a different population model (coupled in a a master-slave configuration, see Fig. 4.15(a)) to study the stability of the phase-locking regimes using a locking

theorem proved in 1996 by Gerstner, Hemmen and Cowan [122, 55]. The time difference ( $\delta_{MS}$ ) between the oscillation of the two populations is typically a function of the strength of the excitatory synapses ( $J_m$ ) from the Master to the Slave and also of the internal inhibitory synapses in the Slave population ( $J_i$ ).

We perform the stability analysis of these phase-locking regimes by using Integrate-and-Fire (IF) neuron models coupled via synapses described by:  $\alpha(s) = (s/\tau^2)\exp(-s/\tau)$ . The membrane potential of each neuron is given by:

$$h_i(t) = \sum_f \eta(t - t_i^f) + \sum_j J_{ij} \sum_f \varepsilon(t - t_i^f) + I_o[1 - \exp(-t/\tau)], \quad (4.12)$$

where  $\varepsilon(t) = \int_0^t \alpha(s) \exp(-(t-s)/\tau) ds$ . Illustrative examples of the synaptic current ( $\alpha(t)$ ) and the neuronal response ( $\varepsilon(t)$ ) are shown in Fig. 4.15(b).

The locking theorem ensures that if

$$\left( \sum_j J_{ij} \sum_f \varepsilon(t - t_i^f) + I_o[1 - \exp(-t/\tau)] \right)' \Big|_{t=T} > 0, \quad (4.13)$$

the oscillatory regime (of period  $T$ ) is stable [122]. In addition, if the left side of Eq. 4.13 is negative or zero the phase-locking regime is unstable.

Unlike the previous sections, in the motif shown in Fig. 4.15(a) each neuron in the Slave population receives excitatory (inhibitory) synapses from all other excitatory (inhibitory) neurons in the same population, which leads to  $\sum_j J_{ij} = (J + J_i)$  (in the simplest case). It also receives the excitatory synapses from the excitatory neurons in the Master population ( $\sum_j J_{ij} = J_m$ ). Using these expressions and calculating the derivatives in Eq. 4.13 our stability condition becomes:

$$\sum_k ((J + J_i)(T - kT)(2\tau - (T - kT)) \exp(-(T - kT)/\tau) + J_M(\delta_{MS} - kT)(2\tau - (\delta_{MS} - kT)) \exp(-(\delta_{MS} - kT)/\tau) + 2I_o\tau^2 \exp(-T/\tau)) > 0. \quad (4.14)$$

The only condition for stable oscillations in the Master population is  $|J_{inh}| > J_{exc}$ . Fig. 4.16(c) shows the stability map for fixed values of all parameters except  $\delta_{MS}$  and  $J_i$ . Different values of  $J_i$  lead to continuous and finite intervals of  $\delta_{MS}$  in which the phase-locking regime is stable.

Since the anti-phase synchronization ( $\sigma_{MS} = T/2$ ) is an unstable solution, and in order to match this results with our previous ones of anticipated synchronization between neuronal population, we separate the stable regions in  $\delta_{MS} < T/2$  (Delayed Synchronization - DS) and  $\delta_{MS} > T/2$  (Anticipated Synchronization - AS). Examples of both situations are shown in Fig. 4.16(a) and (b).

It is also possible to obtain stable phase-locking between the Master and the Slave populations if the excitatory and inhibitory neurons in the Slave population oscillate with a phase difference  $\delta_{SI}$ . In such case they can be considered as two different populations giving rise to two stability conditions: one for the excitatory subpopulation of the Slave and other for the inhibitory subpopulation (data not shown).

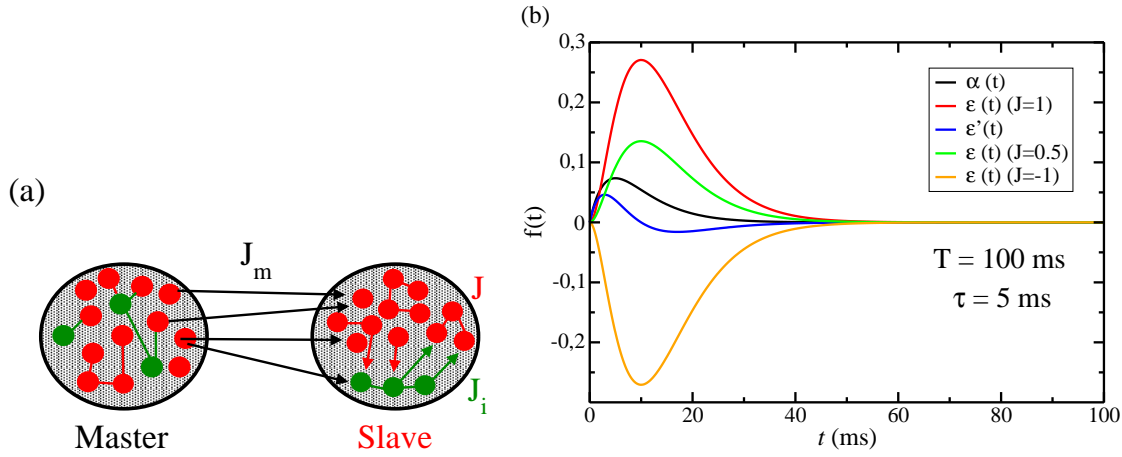


Figure 4.15: IF neurons with high connectivity and in the absence of noise. (a) Two neuronal populations coupled in a master-slave configuration. (b) Examples of the synaptic current and neuronal responses in one period.

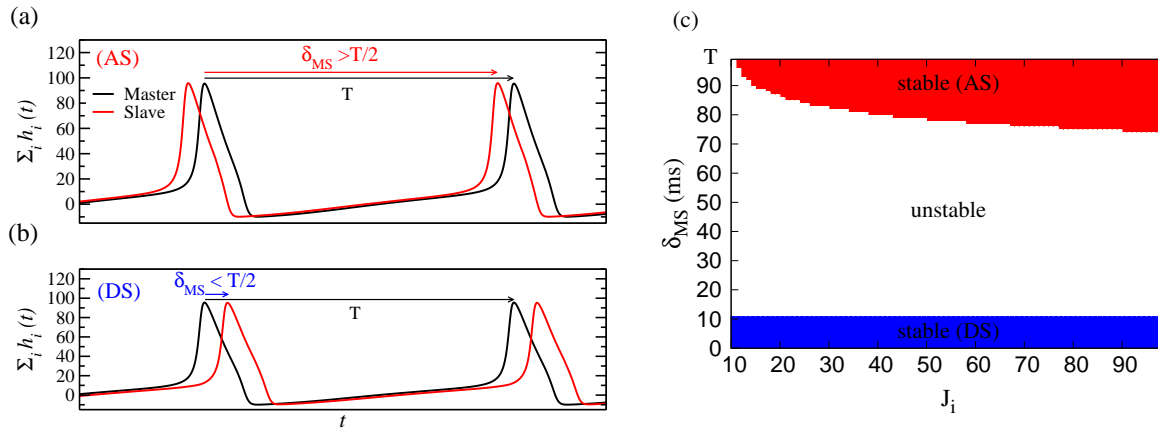


Figure 4.16: Both Anticipated Synchronization (AS) and Delayed Synchronization (DS) are stable for a wide range of parameters. (a)-(b) Examples of phase-locking. The only difference between AS and DS is that (a)  $\delta_{MS} > T/2$  in AS and (b)  $\delta_{MS} < T/2$ . (c) Stability map of the phase-difference  $\delta_{MS}$  for different values of  $J_i$ . Note that the anti-phase regime is unstable.

## 4.8 Discussion

### 4.8.1 Neuronal populations can exhibit AS

Although Voss [4] has suggested that AS could explain phenomena such as the delayed induced transition in visually guided movements [31], to the best of our knowledge there are no explicit reports of AS in neuronal populations. With rare exceptions [36], previous observations of AS in theoretical, physical, and biological systems were based on the original framework, which included a somehow artificial negative delayed self-feedback [4, 29, 8, 20, 33, 10, 12, 14]. Our simple model requires very few ingredients for the emergence of AS in physiologically plausible models. We have shown that substituting the negative delayed self-feedback by a dynamical inhibition, AS can be observed in a model of coupled cortical populations. This would open new perspectives to investigate the existence of the AS regime in other biological systems.

In particular, we have addressed the emergence of AS in populations of neurons representing certain cortical areas and studied its robustness against external noise, heterogeneity and synaptic characteristics. Similarly to what occurs in a 3-neurons motif [39], here the anticipation time emerges from the system dynamics, instead of being explicitly hard-wired in the dynamical equations [4] (see Eq. 1.1). Since the time delay depends on the strength of the synapses, AS could be tuned by neuromodulation.

Comparing structural and functional connectivity matrices of macaque monkey cortex from the CoCoMac database [117, 123] we can emphasize two important aspects. First, both the structural and functional connectivity matrices are not symmetrical, what indicates that there is a moderate amount of preferential coupling direction as in the master-slave configuration. As an example we mention the connectivity matrices of areas that belong to the somatomotor and visual cluster from the CoCoMac database [123]. Second, some pairs of regions have opposite directionality in the structural and in the functional connections. This can be verified in the matrices cited above, for example between areas OC and OA and also between OB and PEp, TA and TF. The names of the areas follow the scheme of Felleman and Van Essen [124] (for more details see Stephan et al. [123]). This can result from the influence of all other areas on these two regions, but could also be AS regimes that were not well characterized.

The robustness and stability of our model indicate that AS results can probably be extended beyond cortical areas (or even beyond the brain). For example the brainstem and central patterns generators in the spinal cord are driven by tonic excitatory brainstem input [125]. Due to biophysical similarities between brainstem spinal cord and neocortical circuits [125] and the fact that inhibition together with excitation dynamically regulate oscillations, these regions can be modeled as master-slave systems with feedback inhibition. The MSI motif in Fig 4.1 is also similar to a simplification of the circuit involving the retina and the lateral geniculate nucleus in the thalamus [65, 68], as well as to the olfactory epithelium and the olfactory bulb [126].

### 4.8.2 Different synchronization regimes within the same anatomical connectivity

Neuronal synchronization is a widespread type of activity, which occurs from sensory systems to higher cortical areas. Due to the communication-through-coherence hypothesis [66] it

is very important that the same structural motif can generate different coherent regimes of oscillations. Flexible patterns of coherence in the same structural motifs facilitate flexible communication. Moreover, different working regimes within the same anatomical connectivity [109] are necessary during changes in behavioral aspects with short time-scales. Our model provides different patterns of coherence within the same anatomical connections. Therefore, flexible communication is one of the possible functional significances of the AS regime and the transitions to DS mediated by inhibition.

Several LFP measures in the brain exhibit synchronization with phase difference [127, 107, 128], for example the theta phase synchronization between hippocampus and medial prefrontal cortex in rats [129, 130], the gamma band synchronization between the frontal eye field and area V4 in monkeys [131] and the beta band synchronization between cortical areas in monkeys [70, 132, 133, 71]. Typically, these phase differences are associated to the synaptic delay between distant regions. However, one needs not be a direct consequence of the other [127]. As we have shown in this chapter, the pool of inhibitory neurons [134, 135] in the cortex can regulate the time delay between the oscillations. It means that the inhibition may annihilate the effect of synaptic delays, providing shorter phase differences (including negative values).



## Cortical data analysis

Phase synchronization is an ubiquitous phenomenon in the study of complex systems that may underlie a variety of neurocognitive processes [136]. Particularly, it has been related to large-scale integration [128], efficiency of information exchange [66], as well as working and long-term memory [127]. Correlation measures are the most widely employed tools for measuring phase synchronization and it is typically used to infer interactions between brain areas [107, 137]. However, correlation alone cannot reveal the influences that are exerted by neurons in one area on those in the other by axonal transmission and synaptic effect. One approach to detecting directional influence in the brain has been to infer it from relative phase measures [138, 139, 140, 141, 131] of neuroelectric indices, such as the electroencephalogram (EEG). The assumption here is that the timing difference implicit in relative phase reflects the transmission time of neural activity. By contrast, other measures of directional influence, such as Granger Causality (GC), have emerged in recent years as an alternative approach that is grounded in the theoretical framework of statistical predictability between stochastic processes [142, 143].

A dominant value for directional influence from one brain area (A) to another (B) indicates that the activity of neurons in area A exerts an effect on the activity of those in area B. It is often assumed that such a directional influence should be accompanied by a positive time delay (relative phase lead of the activity in area A before that in area B), indicating that A's activity temporally precedes that of B. However, this assumed relationship is not theoretically justified. Furthermore, it has been empirically observed that a dominant directional influence between areas of sensorimotor cortex may be accompanied by either a negative or a positive time delay [70]. Brovelli et al. showed that steady contractions of arm and hand muscles by macaque monkeys performing a visual pattern discrimination task are accompanied by phase synchronization of beta-band (14-30 Hz) Local Field Potentials (LFPs) recorded from somatosensory and motor cortical areas [70]. Directional influence among those areas, as assessed by GC, showed that interareal functional relations are usually asymmetrical. Importantly, the interareal relative phase showed no obvious relation to the directionality determined by the dominant direction of causal influence. Thus, for example, even when GC indicated that area A exerted a stronger influence on area B than in the reverse direction, suggesting an asymmetric functional relation dominated by the influence from A to B, it was often the case that area A lagged behind area B in time [70].

A similar incongruence between phase difference and GC between PreFrontal Cortex (PFC) and Posterior Parietal Cortex (PPC) in monkeys performing a working memory task was reported by Salazar et al. [71]. They observed a dominant parietal-to-frontal beta-band GC influence that was opposite to the direction of influence implied by the 2.4 – 6.5 ms time lead of

PFC before PPC derived from relative phase. The dominant parietal-to-frontal direction of GC influence was supported by spike-field coherence analysis, again suggesting that relative phase is not a reliable indicator of directional influence.

Despite efforts to join concepts of anticipatory behavior and AS dynamics [144, 145], biological models of AS, and experimental evidence for it in the brain, have been lacking. As shown in the previous chapters, anticipated synchronization occurs when a unidirectional influence from a generator dynamical system (A) to a receiver dynamical system (B) is accompanied by a negative phase difference between A and B [4, 5, 6]. The only difference between the definition of AS and the reported paradox, is that the causal influence measured in the experiments can not ensure a structural unidirectionality. Therefore, here we propose that the existence of AS in the cortical model presented in Chapter 4 could explain the apparent paradox reported by Broveli [70] et al. and Salazar et al. [71]. We show that our model reproduces delay times, as well as coherence and GC spectra, from the cortical data. Our findings provide a theoretical basis for the observed cortical dynamics, while suggesting that the primate cortex operates in the AS dynamical regime during cognitive function. The model further suggests that the local inhibitory interactions in a receiving neuronal population in the cortex will determine whether that population will anticipate or lag behind sending populations.

## 5.1 More realistic features

To simplify the modeling of the asymmetry observed in the Granger causal influences between pairs of areas, we simulated two unidirectionally coupled cortical-like neuronal populations similar to the modified MSI motif described in the previous chapter. The cortical regions and the motif studied along this chapter are illustrated in Fig. 5.1(c). Connectivity within the M population randomly targets 10% of the neurons, with excitatory conductances set at  $g_E^M = 0.5$  nS and inhibitory conductances set at  $g_I^M = 4$  nS. The S population is also composed of 400 excitatory and 100 inhibitory neurons, forming excitatory slave (ES) and inhibitory slave (IS) subpopulations (Fig. 5.1C). Neurons in the ES subpopulation receive 40 synapses ( $g_E^S = 0.5$  nS) from other neurons of the ES subpopulation, and 10 synapses (with conductance  $g_I^S$ ) from neurons of the IS subpopulation. Neurons in the IS subpopulation receive 40 synapses ( $g_E^S = 0.5$  nS) from neurons of the ES subpopulation and 10 synapses ( $\tilde{g}_I^S = 4$  nS) from neurons of the IS subpopulation (Fig. 5.1C). Note that neurons of the IS subpopulation project synapses with different synaptic conductances to neurons in the same subpopulation ( $\tilde{g}_I^S = 4$  nS) and to neurons in the ES subpopulation ( $g_I^S$ ). Subpopulation IS accounts for the inhibitory loop previously reported to be essential for the emergence of AS [39]. The M and S populations are connected as follows: 20 synapses (with conductance  $g_E^{MS}$ ) from each excitatory neuron of the population projects on the S population. Unless otherwise stated, each neuron receives a Poisson input  $R = 2400$  Hz and no external current  $I_c = 0$ .



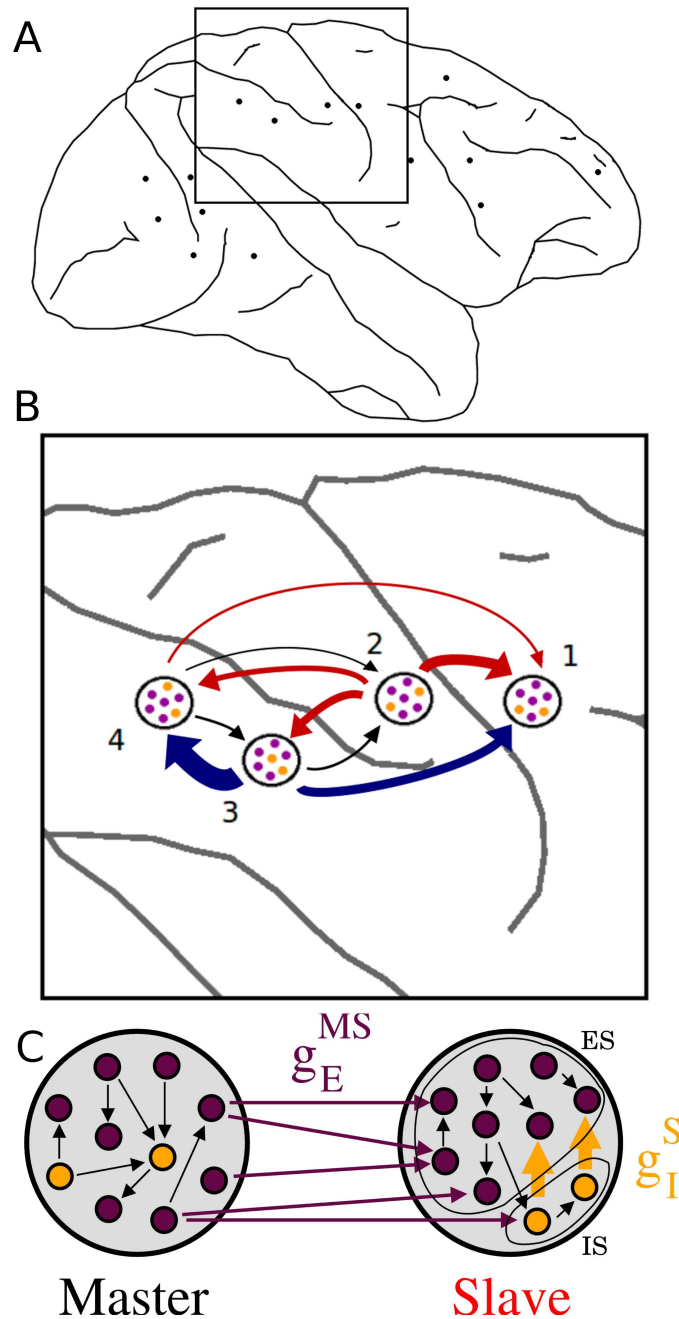


Figure 5.1: (A) Location of recording sites in monkey GE (zoom in the four electrodes analyzed). (B) Sites 1 and 2 are in the primary motor cortex and primary somatosensory cortex respectively. Sites 3 and 4 are in the parietal cortex. Arrows indicate the direction of influence between each pair (Granger causality) and their width are related to the peak of Granger causality shown in Table 5.2. Colors indicate the sign of time delay between pairs, relative to the influence direction. Blue arrows indicate the sender (master) leads the receiver (slave). Red arrows indicate the receiver leads the sender. (C) Schematic representation of two cortical areas coupled in a master-slave configuration. In the model the structural connectivity ensures the direction of influence from the master to the slave. The effective connectivity may also be accessed by Granger causality measures (see Fig. 5.2).

Site Pairs M $\rightarrow$ S	Coherence		Peak of Granger Causality				Phase	Time delay
	Peak	$f_{peak}$ (Hz)	M $\rightarrow$ S	$f_{peak}$ (Hz)	S $\rightarrow$ M	$f_{peak}$ (Hz)	Difference (rad)	$\tau$ (ms)
2 $\rightarrow$ 1	0.1065	25	0.0429	25	—	—	-1.1380	-7.24 (AS)
2 $\rightarrow$ 3	0.4506	24	0.2092	26	0.1205	26	-2.8485	-18.89 (AS)
2 $\rightarrow$ 4	0.1892	24	0.1207	26	—	—	-2.5775	-17.09 (AS)
3 $\rightarrow$ 1	0.1295	24	0.1074	24	—	—	1.4714	9.76 (DS)
3 $\rightarrow$ 4	0.5804	25	0.3029	25	—	—	0.4554	2.90 (DS)
4 $\rightarrow$ 1	0.1027	25	0.0507	27	—	—	0.7236	4.61 (DS)

Table 5.1: Peak of coherence, Granger causality and time delay between all 6 pairs of sites shown in 5.1. Positive values of time delay indicates the master leads the slave (DS), while negative value indicates the master lags behind the slave (AS). From 300 ms to 400 ms after the stimulus onset during a NO-GO task the oscillatory behavior appears again. Comparing to the wait window, shown in Table 5.2, all the directions of causality relations are maintained. The sign of the time delay changes only between sites 1 and 4.

## 5.2 Data acquisition

LFP data was recorded via up to 15 microelectrodes (51- $\mu$ m diameter, 2.5-mm separation) from the sensorymotor cortex (right hemisphere) of an adult male rhesus macaque monkey, as described in Brovelli et al. [70] (Fig. 5.1A)<sup>1</sup>. Data was acquired while the monkey performed a GO/NO-GO visual pattern discrimination task which required it to release (on GO trials) a previously depressed hand lever. Our analysis focuses on 710 trials of the 90-ms period (18 points, 200-Hz sample rate) ending with the visual stimulus onset (wait window). Only correct trials (both GO and NO-GO) were analyzed. Considering the whole task, each trial lasts for 500 ms.

We also tested our model against results from a different experiment, where monkeys performed a working memory task while LFP activity from two cortical regions (PFC and PPC) were recorded. In that case, results were directly extracted from Salazar et al. [71].

## 5.3 Granger causality

Granger causality is a statistical concept of causality that is based on prediction [146]. In Granger's words: "The topic of how to define causality has kept philosophers busy for over two thousand years and has yet to be resolved. It is a deep convoluted question with many possible answers which do not satisfy everyone, and yet it remains of some importance."

The basic idea behind the definition of the Granger causality is quite simple:  $x$  Granger causes  $y$  if the past of  $x$  helps to predict  $y$  better than the past of  $y$ . In a more general way: suppose we have three time series:  $x(t)$ ,  $y(t)$ , and  $w(t)$ . First, we realize an attempt to forecast the value of  $x(t+1)$  using past terms of  $x(t)$  and  $w(t)$ . Second, we repeat the process using, besides the past terms of  $x(t)$  and  $w(t)$ , the past terms of  $y(t)$ . If the second prediction is found

<sup>1</sup>Data from these experiments was kindly provided by Prof. Steven Bressler (Florida Atlantic University).

to be more successful, according to standard cost functions, then the past of  $y(t)$  appears to contain information helping in forecasting  $x(t+1)$  that is not in the past  $x(t)$  or  $w(t)$ . In this case we say  $y(t)$  "Granger causes"  $x(t+1)$  if two conditions are satisfied: (i)  $y(t)$  occurs before  $x(t+1)$ ; and (ii) it contains information useful in forecasting  $x(t+1)$  that is not found in a group of other appropriate variables. This multivariate extension (number of variables  $n > 2$ ), sometimes referred to as conditional Granger causality [147], is extremely useful because repeated pairwise analyses among multiple variables can sometimes give misleading results.

In the simplest case of  $n = 2$  we can write:

$$\begin{aligned} x(t) &= \sum_{j=1}^p A_{11,j}x(t-j) + \sum_{j=1}^p A_{12,j}y(t-j) + E_x(t) \\ y(t) &= \sum_{j=1}^p A_{21,j}x(t-j) + \sum_{j=1}^p A_{22,j}y(t-j) + E_y(t), \end{aligned} \quad (5.1)$$

where  $p$  is the maximum number of previous observations to take into account in the model (the model order), the matrix  $A$  contains the coefficients of the model (i.e., the contributions of each lagged observation to the predicted values of  $x(t)$  and  $y(t)$ ), and  $E_x$  and  $E_y$  are residuals (prediction errors) for each time series. If the variance of  $E_x$  (or  $E_y$ ) is reduced by the inclusion of the  $y(t-1)$  (or  $x(t-1)$ ) terms in the first (or second) equation, then it is said that  $y(t-1)$  (or  $x(t-1)$ ) Granger causes  $x(t)$  (or  $y(t)$ ). In other words,  $y(t-1)$  Granger causes  $x(t)$  if the coefficients in  $A_{12}$  are jointly significantly different from zero.

For data consisting of multiple trials, each trial can be considered as a separate realization of a single underlying stochastic process. Moreover, the coefficients in the multivariate regressive model can be interpreted in the frequency domains, allowing causal interactions to be analyzed by frequency [147]. In this spectral Granger causality, the statistical significance of our results were estimated by constructing surrogate data.

The main limitation of the mathematical formulation given in the Eq 5.2 is that it only accounts for linear information transfer. It is a problem in complex systems (such as the brain) because lots of information is also transferred non-linearly. More complex extensions to non-linear cases exist, however these extensions are often more difficult to apply in practice [146]. Another problem is that Granger causality cannot distinguish between actual straight causality from the interaction via a third process which is not included into the analysis. Moreover, the choice of the factors, for example the model order  $p$  in Eq. 5.2, may influence on the final result. Then, Granger causality should not be directly interpreted as physical causality.

### 5.3.1 Causality measures in neuroscience

Despite the limitations, Granger causality is emerging as a promising and pragmatic measure of information flow in neuroscience [143]. Besides the already mentioned applications of Granger causality to study cortical interactions [70, 71], there are several other works using this method to infer effective connection in data acquired from different techniques [146]. For example, Liang et al. [148] employed it to differentiate feedforward, feedback, and lateral dynamical influences in monkey ventral visual cortex during pattern discrimination. Kaminski et al. [149] noted increasing anterior to posterior causal influences during the transition from

waking to sleep by analysis of EEG signals. In the domain of fMRI, Roebroeck et al. [150] applied it to data acquired during a complex visuomotor task, whereas Sato et al. [151] used a wavelet variation of G-causality to identify time-varying causal influences, and Liao et al. [152] aimed to reveal the network architecture of the directed influence brain network on resting-state. Granger causality has also been applied to simulated neural systems in order to probe the relationship between neuroanatomy, network dynamics, and behavior [153, 154].

Although there are many new methods to infer information flow beyond Granger causality, there is no unanimity as to what is the best method to use. Transfer entropy and directed transfer function are among the most employed methods within neuronal data. In particular, several other methods employed the idea of phase to infer connectivity: phase slope index [155], phase locking value [156], imaginary part of coherency [157], weighted phase lag index [158], pairwise phase consistency [159]. At least one of them, the phase slope index [155], clearly claims to be useful to estimate causality.

An advantage of information theoretic measures (mutual information and transfer entropy), as compared to standard Granger causality, is that they are sensitive to nonlinear signal properties [146]. A limitation of transfer entropy, as compared to Granger method, is that it is currently restricted to bivariate situations. Also, information theoretic measures often require substantially more data than regression methods such as Granger causality [160]. Particularly in the analyzed data here, there are only 18 points in each trial which turns out to be too few points to use transfer entropy.

## 5.4 Spectral Analysis of LFP and simulation data.

Coherence, Granger causality and phase difference spectral analysis were calculated following the methodology reported in Brovelli et al. [70] using the GCCA Matlab toolbox [161]. The autoregressive modeling method (MVAR) employed in Refs. [161, 70] to estimate the spectral analysis from the LFP time series requires the ensemble of single-trial time series to be treated as produced from a zero-mean stochastic process. Therefore, we have preprocessed the LFP time series by including detrending (subtraction of best-fitting line), demeaning (subtraction of the ensemble mean) and normalization (division by the temporal standard deviation) of each trial.

It was also necessary to determine an optimal order for the MVAR model. For this purpose we obtained the minimum of the Akaike Information Criterion (AIC) [162] as a function of model order. The AIC dropped monotonically with increasing model order up to the number of points in a trial minus one. We consider that the model order of 10 (50 ms) used in [70] is sufficient to provide good spectral resolution and avoid overparameterization. In fact, we verified the consistency of the results using model orders of 5 and 15.

For each pair of sites ( $l, k$ ) we calculated the spectral matrix element  $S_{lk}(f)$  [70, 163], from which the coherence spectrum  $C_{lk}(f) = |S_{lk}|^2 / [S_{ll}(f)S_{kk}(f)]$  and the phase spectrum  $\phi_{lk}(f) = \tan^{-1}[\text{Im}(S_{lk})/\text{Re}(S_{lk})]$  were calculated. A peak of  $C_{lk}(f)$  indicated synchronized oscillatory activity at the peak frequency  $f_{peak}$ , with a time delay  $\tau_{lk} = \phi_{lk}(f_{peak}) / (2\pi f_{peak})$ . Directional influence from site  $l$  to site  $k$  was assessed via the Granger causality spectrum  $I_{l \rightarrow k}(f)$  [70, 163] (arrows in Fig. 5.1B are in agreement with Table 5.2).

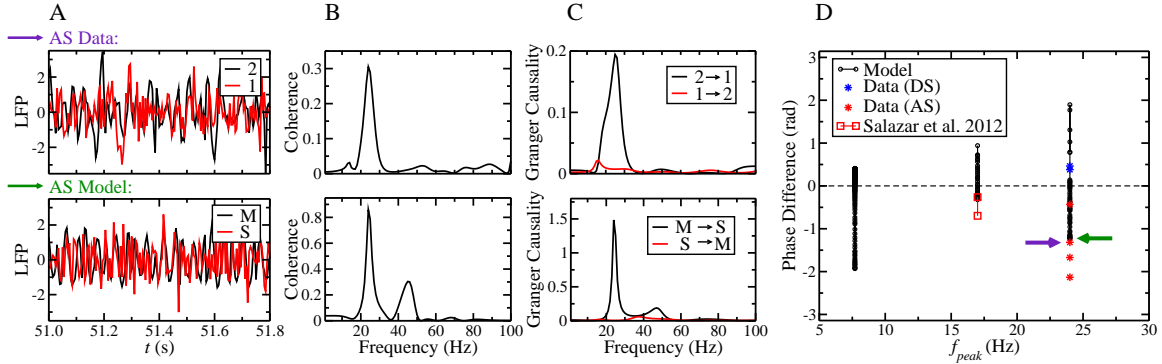


Figure 5.2: Comparison between data from sites 1 and 2 (top) with the results of our model in the AS regime (bottom). (A) Measured and simulated LFP time series. (B) Both in data and model the sites are synchronized with main frequency 24 Hz (peak of the coherence). (C) In data, site 2 Granger causes site 1 (as if site 2 were the master and site 1 were the slave). However, site 2 lags behind site 1 ( $\tau = -8.7$  ms as shown in Table 5.2). Similarly, in the model the master Granger causes the slave, but lags behind it ( $\tau = -8.2$  ms). (D) Phase difference between pairs of site as a function of the frequency in which coherence reaches its maximum value ( $f_{peak}$ ).  $f_{peak} = 24$  Hz, comparable with Ref. [70].  $f_{peak} = 17$  Hz, comparable with Ref. [71]. In this work, posterior parietal cortex Granger causes prefrontal cortex, but prefrontal cortex leads the former ( $\tau$  varies from  $-2.45$  ms to  $-6.53$  ms)

## 5.5 Comparing data and model

From the experimental data, we have selected four pairs of electrodes for which the two following criteria were satisfied: strongly asymmetric influence inferred by Granger causality and strong coherence. In these cases, both the coherence and Granger causality peaks were at similar frequencies. Those results are represented in Fig. 5.1 and summarized in Table 5.2. In all cases the pairs were synchronized in the beta band (around 24 Hz).

Whenever a site  $l$  strongly and asymmetrically Granger causes  $k$ , we refer to  $l$  as a master (M) site and  $k$  as a slave (S) site. Intuitively, in these cases one would expect M to lead S (i.e.  $\tau_{lk} > 0$ ), but the counterintuitive result revealed by Table 5.2 is that there is no consistent relation between GC and  $\tau$  [70, 71]. Given the complexity of the cortical interactions, several mechanisms could account for this phenomenon. Here we propose a minimal model that explains how asymmetrically coupled neuronal populations can synchronize with either positive or negative time delay.

The asymmetry between M and S neuronal populations is structurally built-in in the simulations (Fig. 5.1C). Despite the noise and heterogeneity, the mean membrane potential of the M and S populations can synchronize with the same main frequency. Depending on the synaptic conductances, the system can exhibit delayed synchronization (DS), with  $\tau > 0$ , or anticipated synchronization (AS), with  $\tau < 0$ .

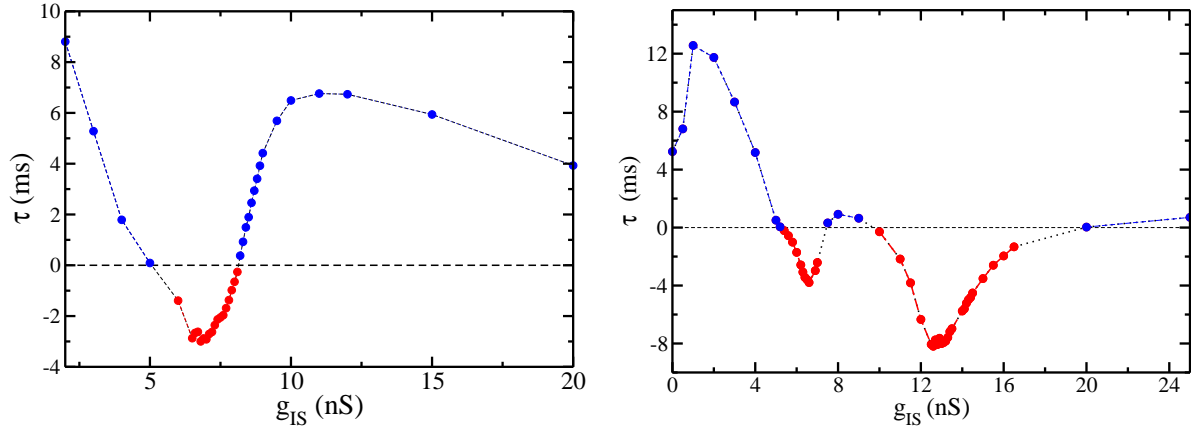


Figure 5.3: Time delay as a function of the inhibitory conductance, corresponding to black dots in Fig. 5.2(d) in the following frequencies: a)  $f_{peak} = 17$  Hz b)  $f_{peak} = 24$  Hz. Like in the previous chapters, the transitions from AS to DS are smooth and continuous.

### 5.5.1 Model reproduces experimental coherence and GC spectra

We have adapted the model to fit the data coherence peak frequency (24 Hz in Fig. 5.2), by adding a constant current to every neuron ( $I = 9$  pA) and adjusting the synaptic conductances ( $g_I^M = \tilde{g}_I^S = 3.2$  nS,  $g_E^{MS} = 0.5$  nS and  $g_I^S = 12.6$  nS). This modification also produced noisier time series that better mimic measured LFPs (Fig. 5.2A). For a fair comparison with data, simulated LFPs took both the ES and IS subpopulations into consideration. We have downsampled the model time series to the same rate employed for the data (200 Hz), after which simulated data was analyzed exactly like experimental data.

In Fig. 5.2 we compare simulation results with experimental data from sites 1 and 2 (primary motor and somatosensory cortices respectively, see Fig 5.1B), which showed a clear unidirectional influence (from 2 to 1) and negative time delay. Tuned to AS, the model yielded a coherence spectrum similar to that of the data (Fig. 5.2B), particularly in its sharpness around the measured peak frequency. Not surprisingly, the absolute values of the peak coherence for the simulations is larger than for the data, probably reflecting the fact that, differently from our simple model, in the brain one region is also influenced by many other regions.

The model also successfully reproduced the main features of the GC spectrum of the data (Fig. 5.2C). A sharp peak was obtained in one direction ( $M \rightarrow S$  in the model), whereas the reverse direction showed a weak and flat spectrum. The fact that the peak frequency of the GC spectra approximately coincides with the peak frequency of the coherence suggests that causality is mediated by the coherence oscillations around 24 Hz [70].

Results by Brovelli et al. showed positive as well as negative time delays, given an asymmetrical GC between two sites [70]. By changing the inhibitory conductance  $g_I^S$ , the model managed to reproduce both regimes (Fig. 5.2D), which corresponded to what we refer to as DS and AS, respectively.

In the second dataset, the peak frequencies were around 17 Hz and the average relative

Site Pairs M → S	Peak Coherence		Peak Granger Causality				Phase	Time delay	
	Magnitude	$f_{peak}$ (Hz)	M → S	$f_{peak}$ (Hz)	S → M	$f_{peak}$ (Hz)	Difference (rad)	$\tau$ (ms)	
2 → 1	0.3051	24	0.1944	25	—	—	-1.3166	-8.73	(AS)
2 → 3	0.4029	24	0.1547	26	0.0892	25	-2.1316	-14.14	(AS)
2 → 4	0.2552	24	0.1086	24	0.0265	26	-1.6706	-11.08	(AS)
3 → 1	0.2546	24	0.1610	24	—	—	0.4637	3.08	(DS)
3 → 4	0.7186	24	0.4203	26	0.0859	28	0.3799	2.52	(DS)
4 → 1	0.2072	24	0.0644	26	—	—	-0.4313	-2.86	(AS)

Table 5.2: Peak of coherence, Granger causality and time delay between all 6 pairs of sites shown in 5.1. In each pair, the site which exerts a larger influence on the other is called the master. The other site, which receives the larger influence, is the slave. Positive values of time delay indicates the master leads the slave (DS), while negative value indicates the master lags behind the slave (AS). A dash (—) indicates that no peak was observed in the Granger Causality spectrum.

phase between PPC and PFC was negative [71]. Our simple model yielded similar results with changes in parameters ( $g_E^{MS} = 1.0$  nS,  $g_I^M = \tilde{g}_I^S = 7.5$  nS,  $g_I^S$  from 6 to 20 nS and a Poisson rate equal to 6000 Hz). In Fig. 5.2D we summarize the comparison between phase differences observed in the model and in the data.

The time delay  $\tau$  as a function of the inhibitory conductances  $g_I^S$  is shown in Fig. 5.3 for both sets of parameters ((a)  $f_{peak} = 17$  Hz and (b)  $f_{peak} = 24$  Hz). Similarly to what was observed in previous chapters, the transition from DS to AS is smooth and continuous. It means that the same model may represent different pairs of sites in Fig. 5.1, since they are modulated by different amounts of inhibition. In particular, sites 1 and 2 from the data have a time delay  $\tau = -8.7$  ms which is quite close to the minimum time delay obtained with our model,  $\tau = -8.2$  ms for  $g_I^S = 12.6$  nS.

Hitherto all results are for the wait period of the task (90 ms before the stimulus onset). Nonetheless, we also analyzed the whole task, which comprehends 500 ms in each trial. After the stimulus, the synchronized activity decreases and, consequently, the peak in the coherence between pairs of sites also decreases. However, during NO-GO tasks, which requires to the monkey to maintain the hand lever depressed, the synchronized activity reappear before the end of the trial. This result was reported by Zhang et al. [164] In Table 5.1 we repeated the same analysis shown in Table 5.2, but for a different interval (from 300 to 400 ms after the stimulus onset) and only for NO-GO tasks. Results are qualitatively the same between all pairs, except for 1 and 4. It means almost all pairs that exhibits AS (or DS) during the wait period, show the same regime in the end of the task (a result which was not reported by Brovelli et al. [70] neither by Zhang et al. [164]).

## 5.6 Discussion

### 5.6.1 Relative time delay is a poor indicator of directional influence

It is well known that the correlation between two variables does not necessarily imply that one causes the other. However, there is a tendency in the literature to use the relative phase between synchronized populations to infer which one is the driver region [165]. As we have shown, in our model the leading population does not necessarily drives the lagging population. By definition, in a master-slave configuration the direction of information flow is from the master to the slave. It means the master drives the slave in both AS and DS regimes. As there is no violation of causality, the existence of an AS regime in such systems reveals that the relative time delay does not always indicate the direction of causal relation.

In prior analysis of cortical LFP data [70], an apparent contradiction was found between the time lag and the GC direction for some pairs of sites (see Table 5.2). A similar paradox was also reported by Salazar et al. for different cortical regions [71]. The apparent contradiction is caused by the assumption that the direction of information flow from one process (A) to another (B) must result in process B following process A in time. However, our model of AS not only proves that this intuition fails but also sets a framework in which an AS regime naturally emerges, reconciling causality with a negative phase lag. To the best of our knowledge, this is the first model to exhibit AS between cortical populations.

It is important to mention that LFPs are highly sensitive to the depth of the recording, which can lead to phase reversal as a function of electrode depth (e.g. [166, 167, 168]). Although this could shift all phase delays by  $\pi$  radians and possibly confound AS with DS and vice versa, that would not eliminate the apparent contradiction between phase lag and causality. In pairs of brain regions in which DS occurs (as e.g. regions 3 and 1 in Table 5.2), causality and phase lag would not match and would still require an explanation.

### 5.6.2 Correspondence between dynamical synchronization regime and functional brain state

In light of the hypothesis that synchronization plays an important role in neural processing and coding [104, 66], different dynamical synchronization regimes may be required for flexible communication to occur within a given structural network architecture. For instance, changes in dynamical synchronization state may be necessary for short-term changes in functional brain state related to cognitive processing [109, 169], or long-term changes related to learning. AS may represent such a dynamical state of synchronization, and thus may be able to open new and unexplored perspectives for understanding this type of coding. Our model suggests that even populations with a strongly unidirectional connectivity can exhibit dynamical flexibility. Simply by small changes in the relative weights of excitatory and inhibitory synaptic conductances, a range of synchronization patterns, displaying positive to negative time lags, can be achieved for the same anatomical structure. In fact, recent neurophysiological evidence [170] suggests that top-down attentional influences act to affect the balance of excitation and inhibition in visual cortical area V4.



### 5.6.3 Effective connections and functional significance

In order to characterize the interaction between distant brain areas, correlated oscillations used to be analyzed [107]. However, cross-correlation functions as well as coherence measures are not always sufficient to indicate neither the structural connection nor the direction of the flux of information of the network [109]. The motifs explored here are examples of such a situation, since the time in which the peak of the cross-correlation function occurs can be positive or negative. A step further in the analysis of brain connectivity during specific tasks is to infer the effective connection (i.e. to infer directional influences, besides correlations) [62]. For this purpose, one should calculate the flux of information using, for example Granger, causality or transfer entropy.

It is worth to mention that if the analyzed data is too small or has low resolution, in an anticipatory situation causal measures such as transfer entropy or Granger causality would state that the information flux is from the slave to the driver (master) [171]. In these situations the sign of the time delay would seem to agree with the apparent flux of information. Such an effective connectivity calculated in the wrong way would not represent real causal flux neither the structural connectivity.

Since the model presented here predicts that the AS-DS transition is mediated by synaptic changes, a related question is whether the functional significance of AS and DS regimes (if any) could be unveiled by monitoring causality and phase lag during the process of learning a new task. On the conservative side, given the central dependence of phase lag on inhibition in the slave population, the observation of AS between primary somatosensory and motor areas could be just an epiphenomenon, reflecting strong inhibition at the primary motor cortex in order to prevent movement, as required by the task [70]. Alternatively, the precise timing in the coordination among areas might subserve additional functions, possibly in connection with attention and perceptual coordination.



# The interplay between spike-timing dependent plasticity and anticipated synchronization in the organization of neuronal networks

How learning and memory is achieved in the brain is a central question in neuroscience. Since antiquity, philosophers have been thinking about this problem. It was Aristotle who proposed the notion of the mind as a *tabula rasa*, or a blank slate. This idea is exactly opposite to that of Plato, who defended that the human mind was created in the heavens, pre-formed and ready. Since then, there is a long-standing discussion about whether we are primarily a product of nature or of nurture [172].

## 6.1 Synaptic plasticity

The most accepted idea nowadays is that the storage of information in our brain is mediated by changes in the synaptic efficiency, a phenomenon called synaptic plasticity. This assumption emerged after the demonstration by Ramón y Cajal that networks of neurons are not in cytoplasmic continuity but communicate with each other via specialized junctions called synapses. In 1949, Donald Hebb [69] conjectured that if input from neuron A often contributes to the firing of neuron B, the synapse from A to B should be strengthened. In his own words: “When an axon of cell A is near enough to excite a cell B and repeatedly or persistently takes part in firing it, some growth process or metabolic change takes place in one or both cells such that A’s efficiency, as one of the cells firing B, is increased” [172]. His ideas are known by the popular slogan: “cells that fire together, wire together”. However, strictly speaking, Hebb’s rule is directional: cell A helps fire cell B.

The strengthening of connections between co-active cells has become known as Hebbian plasticity. The resulting groups of cells joined together through this form of plasticity are called Hebbian assemblies. Hebb also propose that the neural basis of the thought process are the chains of assemblies that create specific sequences of fire. The same cells can participate of several different chains (or percepts) depending on which cells are active at the same time and on the sequence of activation. Then, distinct sequences may represent distinct thought processes [172].

Along the last decades, several experimental works in a number of brain regions including the hippocampus, neocortex, and cerebellum, have revealed activity-dependent processes that can produce changes in the efficacies of synapses that persist for varying amounts of time. Bliss and Løomo’s study [173] was the first to demonstrate that the effects could last for a long period.

Their work was the first verification of synaptic plasticity in the mammalian brain, particularly in the excitatory synapses of the hippocampus, a region which participates in learning and formation of memory in humans. They showed that brief trains of high-frequency stimulation to monosynaptic excitatory pathways in the hippocampus cause an abrupt and sustained increase in the efficiency of synaptic transmission.

Lynch et al. [174] reported that while high-frequency stimulation induced potentiation of the activated pathway, the inactive pathway may suffer depression. This was in agreement with Hebb's idea of a slow "synaptic decay" for unused connections. Even though he did not propose an active mechanism to weaken synapses, long-lasting depression was also found to occur at the activated pathway when the activation frequency was low [175]. Synaptic increase or decrease that persists for tens of minutes or longer are generally called long-term potentiation (LTP) and long-term depression (LTD), respectively.

Despite plenty of plasticity models based on correlations of pre- and postsynaptic firing (known as rate-based rules), in more recent years a novel concept in cellular learning has emerged, where temporal order of pre- and post-synaptic spikes instead of frequency is emphasized. This new learning paradigm, known as spike-timing-dependent plasticity (STDP), has rapidly gained interest because of its combination of simplicity, biological plausibility, and computational power. [172]

### 6.1.1 Spike-timing-dependent plasticity (STDP)

Markram and Sakmann reported a breakthrough study on the importance of precise relative timing of spikes emitted by the pre and post-synaptic neurons in the neocortex [176]. They revealed that LTP occurs when the time difference between the pre- and the postsynaptic neurons is around 10 ms and the presynaptic neuron spikes first. On the other hand, LTD was shown to happen due to acausal pre-after-postsynaptic spike timings, even when they employed the same stimulation frequency to generate pre-post and post-pre spikes.

In 1998, Bi and Poo [177, 178] mapped essentially the entire STDP window. First, they evoked spikes in both pre and postsynaptic neurons with a precise time difference ( $\Delta t$ ). Second, they measured changes in the excitatory postsynaptic potential (EPSP) as an indirect measure of the strength of the synapse (see Fig. 6.1). A positive  $\Delta t$  means that the presynaptic neuron fires spike before the post synaptic neuron, which has been shown to induce LTP. A negative  $\Delta t$  is associated with the opposite order (a post-pre spike) and generates a decrease in the amplitude of the EPSPs, which characterizes LTD. Then, they repeated the process in a roughly 40-ms-long coincidence window. More interestingly, they reported a rapid 1-ms transition between LTP and LTD for near-perfect coincidence between pre and postsynaptic cell activity. This sudden transition between LTP and LTD is in biological terms essentially instantaneous. Despite quite surprising, it was later reproduced in the neocortex [179] and is now considered one of several hallmark features of STDP [172].

To mathematically describe the relation shown in Fig. 6.1 an additive STDP rule has typically been used:

$$g = \begin{cases} g + A_+ \exp(-t/\tau_+), & \text{if } t > 0 \\ g - A_- \exp(t/\tau_-), & \text{if } t < 0 \end{cases} \quad (6.1)$$

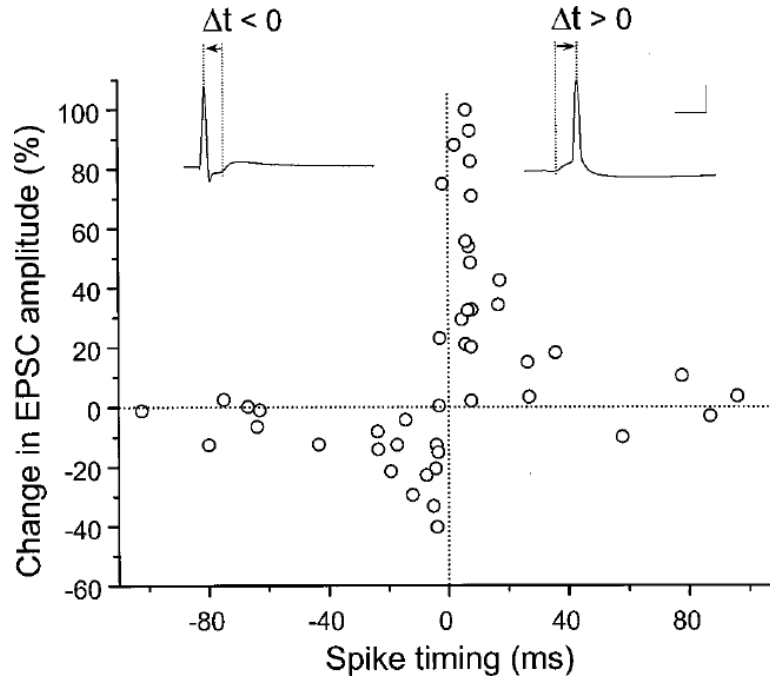


Figure 6.1: Spike-timing-dependent plasticity (STDP) verification in paired recordings in dissociated neuronal cultures. Changes in the strength of unidirectional excitatory synapses due to different time differences between the spikes from pre and post synaptic neurons. Figure reproduced from Bi and Poo [177].

where  $g$  is the synaptic conductance (or weight) and  $t = t^{post} - t^{pre}$  is the time difference between pre and post synaptic spikes.  $A_+$ ,  $A_-$ ,  $\tau_+$  and  $\tau_-$  are the parameters to fit the data. In our notation along this thesis, in a unidirectional configuration, the postsynaptic neuron is the slave and the presynaptic neuron is the master. The experiments suggest that  $\tau_+$  varies in a range of tens of milliseconds [180].

Over the past decades, STDP has been found in a range of species from insects to humans [181]. Specially, STDP has been demonstrated in the human primary motor cortex [182]. Pairing electrical stimulation of somatosensory afferent nerve with transcranial magnetic stimulation (TMS) leads to long-lasting changes in the motor-evoked potentials (MEPs) elicited by TMS.

It is worth mentioning that inhibitory synapses can also display plasticity, but just in the last years this was thoroughly investigated both experimentally and theoretically [183]. Moreover, different experiments reported completely different temporal windows [181]. Therefore, along this chapter we will not apply STDP rules to the inhibitory synapses.

## 6.2 AS and STDP synergetically organize the network dynamics

The interplay between STDP and Anticipated Synchronization can have a major influence over the structural organization of neuronal networks. STDP relies on relative spike timing to induce modifications on the connectivity of neuronal networks, through the potentiation or depression of synaptic strengths. On the other hand, the modification of the synaptic strengths can induce transitions between AS and DS synchronization regimes. However when the network synchronization regime changes from DS to AS, the relative spiking time between pre and post-synaptic neurons is inverted, leading to an inversion of the STDP (e.g. from potentiation to depression).

One problem in applying STDP rules in neuronal networks is the stability. In numerical simulations of unidirectional couplings, it is usually necessary to set an arbitrary upper boundary to the synaptic weights [180]. It is also necessary to avoid that the plasticity rule changes the signal of the conductance, because it should not turn an excitatory synapse into an inhibitory one. Moreover, according to experimental data, synaptic weights should fulfill the following key properties [184, 185]: (i) The weight distribution should be stable. Unchanged patterns during a synchronized regime would allow the information carried through the connections to be consistently interpreted; (ii) Synaptic weights should present diversity. This is the opposite to all weights having the same value or binary weights. Functionally, a graded set of connections can perform a richer set of computations [186, 187]; (iii) Weights should be limited. It means that due to the finite number of neuromodulators, bindings, etc, the synaptic weights should not grow to biophysically unrealistic values. It also avoids amplification of neuronal activity to pathological levels.

We started by extending the 3-neuron model presented in Chapter 2 to the presence of STDP in the synapse from the master to the slave (excitatory to excitatory neuron). Then we studied the neuronal population model presented in Chapter 3 in light of STDP rules between synapses from neurons in the master population to neurons in the slave population. First, we verified that AS exists and can be stable in the presence of STDP rules. Second, we proposed that STDP could facilitate a self-organized near zero-lag synchronization. More interestingly, we showed that the interplay between AS and STDP rules gives stable synaptic weight distributions that are comparable to experiments in the cortex [185].

## 6.3 STDP in the 3-neuron motif

To initiate the study of the effects of STDP rules in a system that exhibits a smooth transition from AS to DS, we chose the 3-neuron motif modeled by HH neurons of Chapter 2. The microcircuit is represented in Fig. 6.2(a). Synaptic plasticity was applied in the excitatory synapses from the Master to the Slave  $g_{MS}$ . Unless otherwise stated, all parameters are as in Table 2.1.

For fixed  $g_{IS} = g_{SI} = 40$  nS, the time delay  $\tau$  between the Master and the Slave is a smooth function of  $g_{MS}$  (i.e. in the absence of STDP). This relation is shown in Fig. 6.3. Similarly to what is described in Chapter 2, the motif in Fig. 6.2(a) presented two phase-locking regimes: DS (blue) and AS (red), and a phase-drift (PD) regime. It is important to mention that in

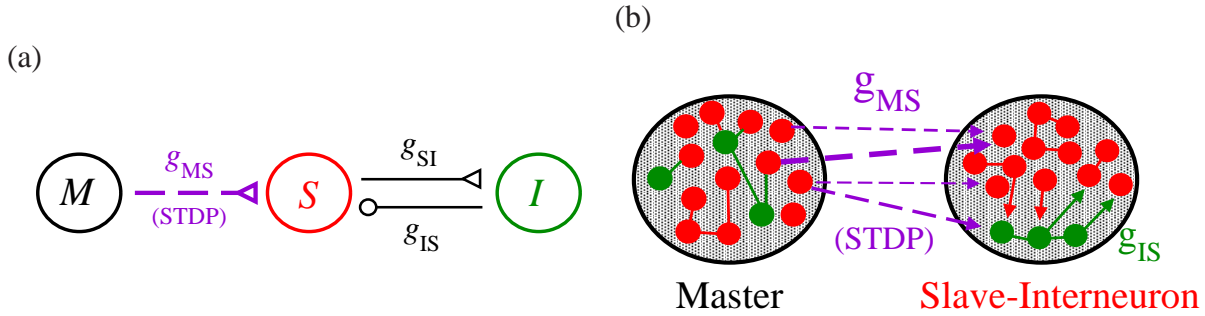


Figure 6.2: MSI motifs in the presence of STDP rules. (a) Three neurons coupled by chemical synapses in the master-slave-interneuron (MSI) configuration. Excitatory AMPA synapse from the Master to the Slave  $g_{MS}$  under STDP rules. (b) Master and Slave-Interneuron cortical-like populations. Each synapses from M to SI has a different conductance  $g_{MS}$  which can change due to STDP.

Chapter 2 we varied the two excitatory synapses  $g_A$ , mediated by AMPA, at the same time, which means  $g_{MS} = g_{IS}$ , whereas in this chapter we fixed  $g_{IS} = 40$  nS.

Considering the results shown in Fig. 6.3 we expected that if we switched on the STDP rules, in an AS regime the synaptic conductance  $g_{MS}$  decreases by LTD, while in a DS regime,  $g_{MS}$  increases by LTP (see arrows in Fig. 6.3). To verify this hypothesis, we applied the additive rule described in Eq. 6.1 with  $\tau_+ = \tau_- = 10$  ms and  $A_+ = A_- = 1$  nS for the excitatory conductance  $g_{MS}$ .

We studied three different situations: initial value of conductance  $g_{MS} = 40$  nS (DS),  $g_{MS} = 20$  nS (AS) and  $g_{MS} = 2$  nS (PD). In Fig. 6.4 we show how the conductance changes along the time in each case. As mentioned above, to avoid infinitely large or negative values of conductances it is necessary to choose an upper ( $g_{MS} = 300$  nS) and a lower ( $g_{MS} = 0$ ) boundary for the conductance. For  $t < 500$  ms the system is in a well defined regime, then the STDP rules are turned on and there is a transient time until the new regime is reached. Together with the boundaries ( $g_{MS}^{upper} = 300$  nS and  $g_{MS}^{lower} = 0$ ), the three initial conditions allow the following transitions: DS $\rightarrow$ DS, AS $\rightarrow$ PD, and PD $\rightarrow$ PD. In Fig. 6.5 we illustrate the membrane potential of the Master (black), the Slave with no STDP rules (red) and the Slave after the STDP rules are applied and the system reached the new regime (dashed-violet lines).

Moreover, if we use another lower boundary, for example  $6 < g_{MS} < 32$  nS, it is possible to end in an AS regime (data not shown). Although distinct temporal windows for STDP between excitatory-inhibitory synapses have been proposed, if we apply the additive STDP rules of Eq. 6.1 on the synapse from the slave to the interneuron,  $g_{SI}$  simply goes to the upper boundary. Since the order of pre-post spikes between S and I does not change either in AS or DS, the time difference  $t^I - t^S$  is always positive and the conductance  $g_{SI}$  always increases through LTP. We employed a fixed value of conductance  $g_{SI} = 40$  nS, but we verified that the results are qualitatively similar for other values of  $g_{SI}$ .

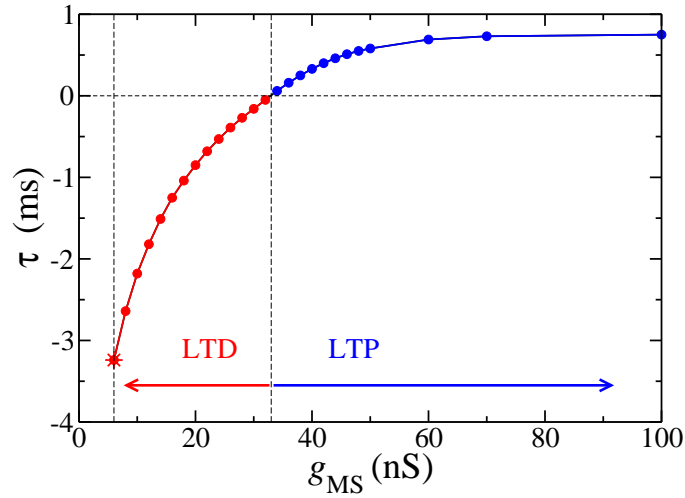


Figure 6.3: Time delay as a function of the excitatory conductance  $g_{MS}$  for fixed values of  $g_{SI} = g_{IS} = 40$  nS and no plasticity rules. If we turn on STDP, the DS region  $g_{MS} > 32$  nS should lead to LTP whereas the AS region  $6 < g_{MS} < 32$  nS should lead to LTD. For  $g_{MS} < 6$  nS the system presents a phase-drift (PD) regime and  $\tau$  does not converge to a fixed value.

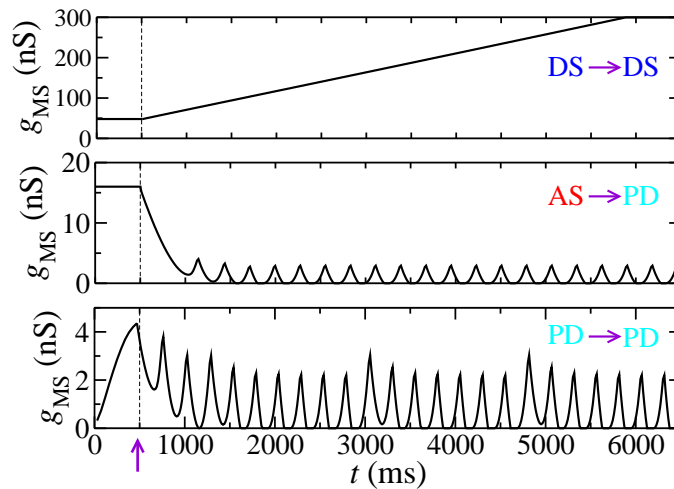


Figure 6.4: The synaptic weights as functions of time for three different situations. Initial values of  $g_{MS}$  are:  $g_{MS} = 40$  nS in the top (starting from a DS regime),  $g_{MS} = 20$  nS in the middle (starting from AS) and  $g_{MS} = 2$  nS in the bottom (PD). STDP rules were switched on at  $t = 500$  ms (vertical arrow).



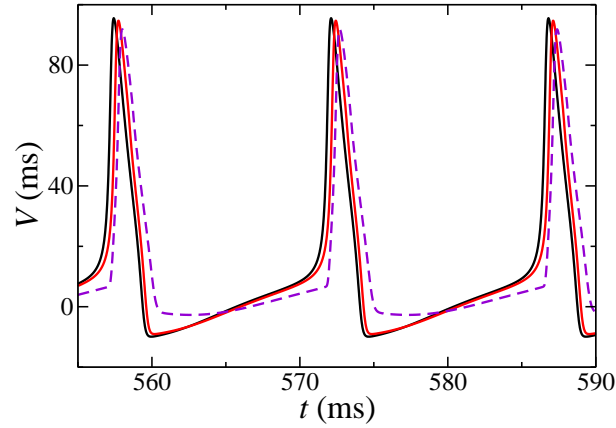
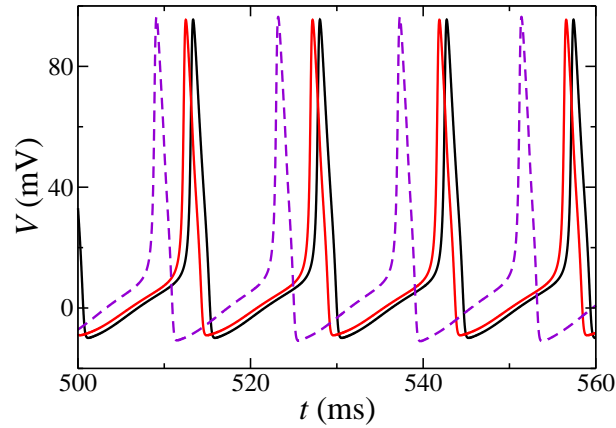
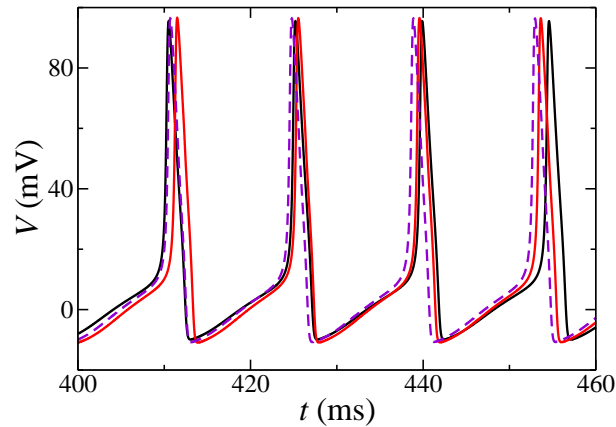
(a) DS  $\rightarrow$  DS(b) AS  $\rightarrow$  PD(c) PD  $\rightarrow$  PD

Figure 6.5: The effect of STDP rules in the 3-neuron motif for the three cases shown in Fig 6.4. Membrane potential of the Master (black), the Slave without STDP (red) and the Slave (dashed violet) with STDP rules acting on the  $g_{MS}$ . (a) Initial value of  $g_{MS} = 40$  nS, final value  $g_{MS}^{upper} = 300$  nS (upper boundary arbitrarily chosen). The system begins in the DS regime and remains there. (b) Initial value of  $g_{MS} = 20$  nS. The system starts in the AS regime, then  $g_{MS}$  decreases until values smaller than 6 nS and the system reaches the PD.  $g_{MS}$  periodically oscillates between  $0 \leq g_{MS} \leq 3$ . (c) Initial value of  $g_{MS} = 2$  nS. Lower boundary:  $g_{MS}^{lower} = 0$ .

## 6.4 STDP between neuronal populations

In this section, we are interested in comparing the connectivity effects of the interplay between AS and STDP in a model to experimental data from the cortex. Therefore, we applied STDP rules to the synapses between two neuronal populations coupled in a master-slave configuration. In particular, we used the modified MSI motif described in Chapters 4 and 5 in which the Slave and Interneuron (S) are together as a single cortical region (see Fig. 6.2). Without plasticity, all excitatory synapses  $g_{MS}$  have the same value, and the time delay  $\tau$  is a function of both  $g_{MS}$  and  $g_{IS}$  as shown in Fig. 4.9. A positive value of  $\tau$  indicates DS (blue), whereas  $\tau < 0$  characterizes AS (red).

In the additive rule described in Eq. 6.1 both the amounts of potentiation and depression do not depend on the previous values of the weights. This is a good model to describe situations in which the relative potentiation in strong synapses is less intense than in weak synapses. However, it does not always hold for synaptic depression [188]. In these cases a hybrid rule has been proposed as an improved model for the STDP rule:

$$g = \begin{cases} g + A_+ \exp(-t/\tau_+), & \text{if } t > 0 \quad (\text{additive LTP}) \\ g - A_- g \exp(t/\tau_-), & \text{if } t < 0 \quad (\text{multiplicative LTD}) \end{cases} \quad (6.2)$$

where  $\tau_- = \tau_+ = 5$  ms,  $A_- = 1.0$  and typically  $A_+ = 0.5$  nS, but it can be varied from 0.2 to 3.5 nS. We will show that this hybrid rule together with AS provide more realistic results.

### 6.4.1 AS in the presence of STPD: an emergent property

For simplicity, we fixed all the intra-population synapses and applied STDP rules only in the synapses  $g_{MS}$  between M and S populations. Unless otherwise stated, all parameters are given by Table 4.1. When we turned on the STDP rules, each  $g_{MS}$  synapse were modified according to Eq. 6.2 and consequently the mean of the time delay in each period ( $\tau = \langle \tau_i \rangle$ ) changed. After a transient time, the system reached a synchronized regime in which the two populations oscillate with a well defined value of  $\tau$ . The time delay could be either positive (DS) or negative (AS). The mean membrane potential of the M and S populations as well as the time delay are illustrated in Fig. 6.6 for an example of AS and DS, both in the presence of STDP. Results are robust independently of when we turn on the plasticity rules (i.e. in the beginning of the simulation or after the system reaches a synchronized regime).

In the cortical-like networks explored in this chapter, it is possible to start in an AS regime and go to DS via STDP (changing the parameters  $g_{IS}$  and  $A_+$ ), or to go in the opposite way: DS  $\rightarrow$  AS (differently from what happens in the 3-neuron microcircuit). This is an emergent property that arises from the synergetic interplay between STDP and AS in modifying  $\tau$  to generate changes in  $g_{MS}$  and vice versa. In Fig. 6.7(a) we show the relation between  $\tau$  and  $g_{IS}$ . Comparing the two curves with and without plasticity in Fig. 6.7(a), we can see, for example, that for  $g_{IS} = 7.5$  nS the effect of STDP is to take the system from DS to AS.

Furthermore, in Fig. 6.7(b) one can see  $\tau$  as a function of the dimensionless parameter  $A_+$  for fixed  $g_{IS} = 4$  nS. In the absence of STDP and  $g_{IS} = 4$  nS the system is in AS. Thus, this plot shows that for  $A_+ \leq 2.2$  the system can start on AS and stay in the same regime, whereas

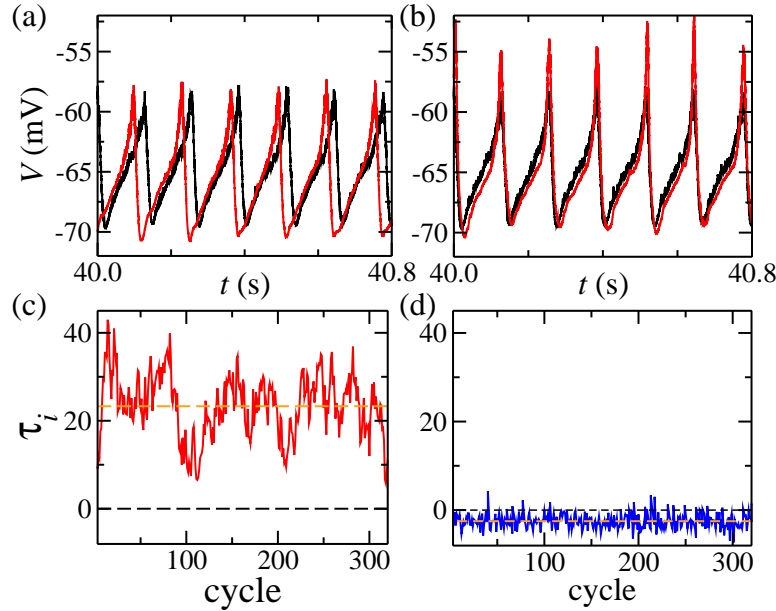


Figure 6.6: Characterizing AS and DS regimes in the presence of STPD. (a) and (b) Membrane potentials of Master (black) and Slave (red) populations. Since the peaks of M and S are very close, the DS regime can be considered a near zero-lag regime. (c) and (d) Time delay  $\tau_i$  in each cycle. The mean time delay  $\tau$  (orange dashed line) is positive in the AS regime and negative in DS.

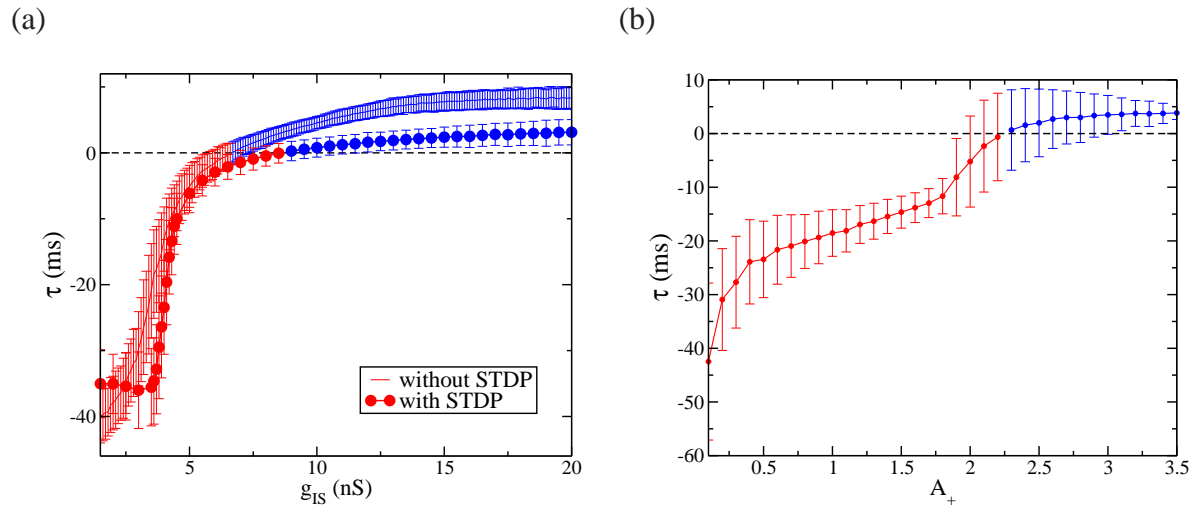


Figure 6.7: Smooth transition from AD to DS (a) Time delay as a function of inhibitory conductances. Comparing the case with no plasticity and the hybrid STDP rule with  $A_+ = 0.5$  and  $A_- = 1.0$ . Plasticity brings the system to near zero lag synchronization. (b) Time delay as a function of  $A_+$  For fixed  $g_{IS} = 4.0$  nS and  $A_- = 1.0$ . There is AS even for  $A_+$  higher than  $A_-$ .

for for  $A_+ > 2.2$  the system can go from AS to DS. Indeed, the two regimes and the possible

transitions from one to the other are spread in large regions of the parameter space. Altogether, AS and DS are stable and robust against STDP.

### 6.4.2 Hybrid STDP and AS stabilize synaptic weight distribution

There have been several attempts to link weight distributions and synaptic plasticity rules; in particular, STDP rules have received most of the attention [185, 180]. Typically, the additive rule in Eq. 6.1 produces a bimodal distribution [24,26], with synaptic strengths clustering both around zero and at the imposed maximum synaptic weight. However, Barbour et al. argued that “the bimodal distribution resulting from an additive rule appears to be in conflict with existing data, in which no such bimodality can be detected” [185]. Fig. 6.8 shows examples of experimental synaptic weight distributions in different brain regions and types of cells reported in the literature. All the distributions shown have similar shapes (but different scales): a monotonic decay with maximum probability near zero [185]. In addition, plenty of studies (in the cortex, hippocampus, and cerebellum) strongly suggest the existence of a large majority of undetectable (silent or potential) synapses with almost zero weight.

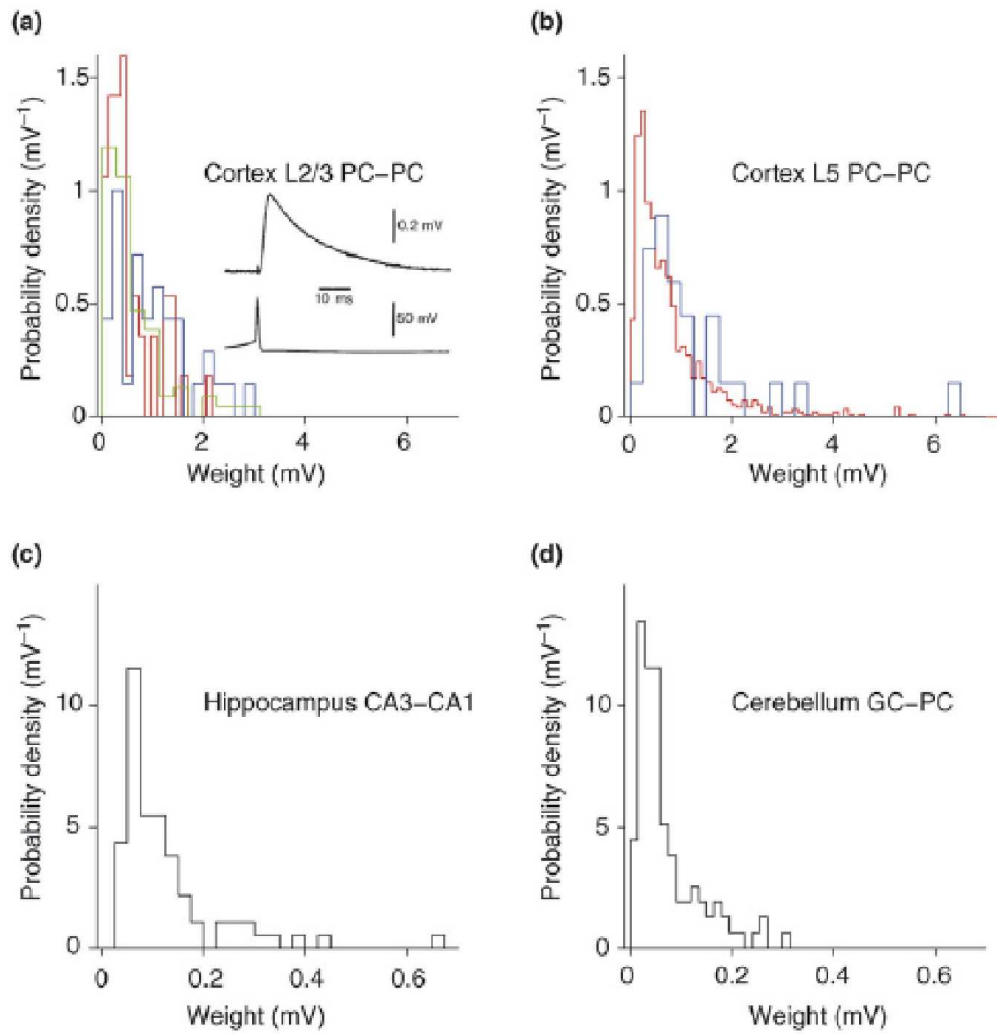
The most amazing result in our model is related to the synaptic weight distribution when the system reaches an AS regime via STDP. The mentioned features about experimental shape of the weight distributions (monotonic decay with maximum probability near zero) are reproduced by our MSI motif in the AS regime (see Fig. 6.9(a)). Moreover, the distribution of  $g_{MS}$  obeys the three key properties explained in Sec. 6.2 as a result of the dynamical interaction between AS and STDP: (i) the distribution is stable, (ii) diverse and (iii) limited. More interestingly, the synaptic weight distributions are limited without the necessity of arbitrarily chosen boundaries. Even considering that each synapse individually is changing along the time, the distribution of all synaptic weights maintains the same pattern and the system remains in the same synchronized regime.

On the other hand, for a DS regime, the third property is not completely satisfied. Eventually it is necessary to arbitrarily choose an upper boundary for the weights, otherwise some of them grow beyond biophysical limits. In the bottom of Fig. 6.9(a), in the absence of a boundary, we see that there is probability of finding large values of  $g_{MS}$  in the DS regime, whereas that does not happen for AS. The choice of the maximum value of  $g_{MS}$  can lead to a bimodal distribution for DS (data not shown). However, stability and diversity are present.

Differently from the 3-neuron motif studied in Section 6.3, results here do not depend on the initial values of  $g_{MS}$ . Each synapse has a different behavior but all synapses together give similar weight distributions along the time. In Fig. 6.9(b) we see the evolution in time of four randomly chosen synapses from each different initial condition in the AS (top) and DS (bottom) examples. In DS there is a probability of extremely fast growing which results in large values of conductance as mentioned before. In AS all weights converge to small values, no matter its initial values.

### 6.4.3 Other STDP rules

In order to compare the different possible cases, besides the hybrid rule we tested our model against two other rules that can also describe the data shown in Fig. 6.1. Firstly, the multiplica-



TRENDS in Neurosciences

Figure 6.8: Experimental synaptic weight distribution in the cortex. All data have similar features: a monotonic decay with maximum probability near zero, but distinct scales. Reproduced from Ref. [185].

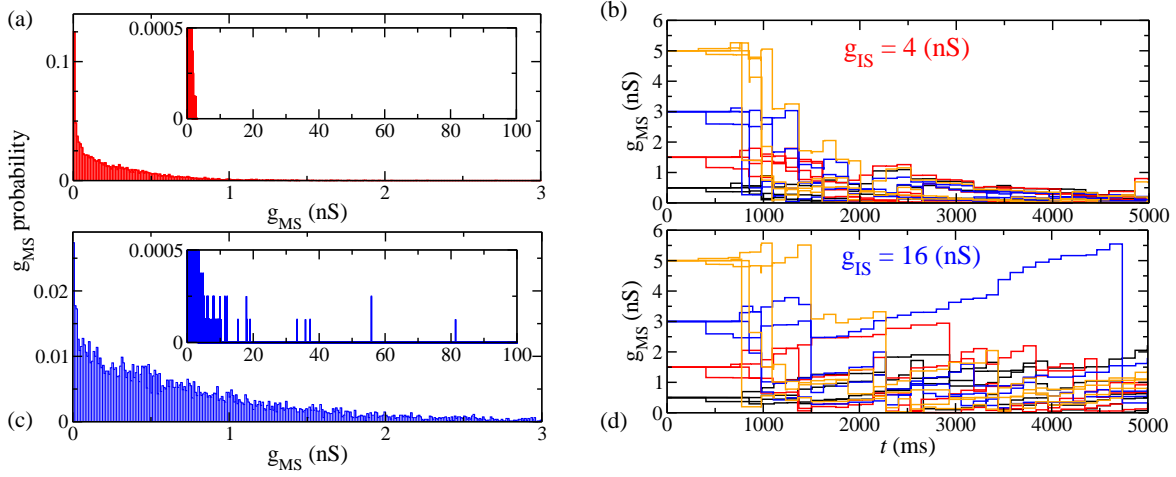


Figure 6.9: Synaptic weight distributions in the presence of hybrid STDP rules. (a) and (b) AS, with  $g_{IS} = 4$  nS. (c) and (d) DS  $g_{IS} = 16$  nS.  $A_+ = 0.5$  and  $A_- = 1.0$  are kept fixed. (a) and (c) Histogram of the  $g_{MS}$  values. In the inset of (a) AS gives limited weight distribution even without choosing an arbitrary upper boundary. However, in the DS regime some synapses grow unlimited. (c) and (d) Independence of the initial synaptic conductances. Each color represents a different simulation in which all initial synaptic conductances were the same  $g_{MS} = 0.5$  nS (black),  $g_{MS} = 1.0$  nS (red),  $g_{MS} = 3.0$  nS (blue),  $g_{MS} = 5.0$  nS (orange). For each simulation we show 4 randomly chosen synaptic conductances evolving in time. In the AS regime (top), the conductances  $g_{MS}$  vary in a limited interval. In the DS regime (bottom), since the beginning of the simulation, there is a tendency for some synapses to grow more than others.

tive STDP model:

$$g = \begin{cases} g + A_+ g \exp(-t/\tau_+), & \text{if } t > 0 \\ g - A_- g \exp(t/\tau_-), & \text{if } t < 0. \end{cases} \quad (6.3)$$

This rule requires an upper boundary  $g^{upper}$  for both DS and AS and provides no diversity in the weight distribution. Virtually all weights end up in the minimum  $g_{MS} = 0$  or in the maximum value  $g_{MS} = g^{upper}$ .

Secondly, we employed the additive rule in Eq. 6.1 with no boundaries. The distribution is a Gaussian centering in zero for the AS case and centering in a positive number for DS. However, it allows negative conductances, which is not biophysically plausible. If we choose the lower boundary to be zero, in order to avoid the negative values of conductances, the weight distribution for AS is similar to the hybrid case. Nevertheless, in the DS regime the stability is compromised, and  $\tau_i$  is non-stationary (i.e. its mean and variance change over time).

The 3-neuron results are qualitatively the same for the three STDP rules. The results with this microcircuits should be more interesting in the presence of plasticity in the inhibitory synapses. Although inhibitory plasticity was reported to provide completely opposite STDP window in certain experiments, which cannot be described by any of the rules employed in this chapter, this could be potentially enlightening for the interplay between AS and STDP.

## Concluding remarks and further perspectives

Understanding the brain is a challenge that is attracting an increasing number of scientists from many different fields, what makes neuroscience perhaps the most remarkable example of interdisciplinarity. In particular, computational neuroscience aims to use theoretical approaches from physics, mathematics, computer science and engineering to integrate experimental observation, data analysis and theoretical modeling. In this thesis, we studied the relation between structure and dynamics in distinct biophysical models of neurons and brain regions. We presented a detailed analysis of anticipated synchronization (AS) in biologically plausible neuronal network models within different scales and proposed experimental setups to test our hypothesis. Moreover, we proposed that the mismatch between directional influence and phase difference in cortical experiments reported by Brovelli et al. [70], whose data we also analyzed here, can be the first verification of AS in the brain.

As explained in the scope of this Thesis, AS is a form of synchronization that occurs when a unidirectional influence is transmitted from a generator to a receiver, but the receiver precedes the generator in time. This counterintuitive synchronization regime can be a stable solution of two dynamical systems coupled in a master-slave configuration, when the slave receives a negative delayed self-feedback. In this thesis, we showed that a master-slave system can also exhibit AS when this negative delayed self-feedback is replaced by a dynamical inhibitory loop mediated by chemical synapses. This replacement opens new avenues in the study of AS in biophysical systems.

In Chapter 2, we showed that a canonical neuronal microcircuit with standard chemical synapses, and where the delayed inhibition is provided by an interneuron, may exhibit AS. It means that, when a master neuron sends an excitatory synapse to a slave neuron, which excites an interneuron and receives an inhibitory synapses back from it, the slave is able to fire spikes before the master. Moreover, the time delay  $\tau$  between consecutive spikes of the master and the slave is shown to be a continuous and smooth function of the inhibitory synaptic conductance. Therefore, this 3-neuron motif presents a smooth transition from the delayed synchronization (DS, when the master spikes before the slave) to AS mediated by synaptic conductances.

The phenomenon is shown to be robust in the 3-neuron motif when model parameters are varied within a physiological range. The AS regime and the transition AS-DS is also exhibited when different setups are included in our motif: in the presence of a common driver neuron that simultaneously excites all three neurons; when there exists external noise; in modified neuron models; in a chain of slaves and interneurons; in the presence of an excitatory feedback from the slave to the master; and in a simple model for the motor circuit of the spinal cord. Moreover, results in this chapter could be tested in a hybrid patch clamp setup, in which the inhibitory synaptic conductance can be simulated in real time.

In Chapter 3, the 3-neuron motif was analytically investigated using the theory of phase response curves (PRCs) for phase-locking regimes. We employed the approximation of weak coupling oscillators, to calculate the Poincaré phase map for the difference between spike timing of the neurons. The stability conditions were calculated as a function of the PRCs of the master, the slave and the interneuron. This approach could facilitate the investigation of AS, reducing the problem to the analysis of a set of conditions that should be satisfied by the PRC of the involved neurons. These results still need to be corroborated by further numerical simulations. As a matter of fact, we cannot use the standard Hodgkin-Huxley neuron model employed in chapter 1 for this task, because it was not able to satisfy the necessary weak coupling approximation, and the choice of a better model remains under consideration.

In Chapter 4, we presented a model of two brain regions coupled by a well-defined directional influence (master M and slave S populations), that is the first model of neuronal population to displays AS. Each population is composed of hundreds of neurons with the necessary ingredients to mimic cortical-like sub-networks. We employed realistic brain features, such as the proportion of excitatory and inhibitory neurons, variability in the neuronal dynamics, noise, baseline firing rates and global topological motifs. Similarly to the 3-neuron motif case, the system exhibits an AS regime and a smooth AS-DS transition, which could be mediated by several parameters: synaptic conductances, Poisson rate, proportion of different classes of neurons in S, etc. Since the anticipation time emerges from the system dynamics, instead of being explicitly hard-wired in the dynamical equations [4] (see Eq. 1.1), AS could be tuned by neuromodulation.

Despite of the several existing studies of AS in physical systems, a verification on AS in the brain has not been reported. Therefore, in Chapter 5 we proposed that our neuronal population model can be compared to *in vivo* experimental results and explain counter-intuitive results reported in cortical data. Brovelli et al. [70] observed that, in monkeys engaged in processing a cognitive task, a dominant directional influence from one cortical area to another may be accompanied by either a negative or a positive time delay. Here we compared our populational model's dynamics in the AS regime to the experimental results of Brovelli et al. By reproducing delay times and coherence spectra, our results provide a theoretical basis for observed neurocognitive dynamics, and suggest that the primate cortex may operate in the AS dynamical regime as part of normal neurocognitive function. The existence of AS between cortical regions in non-humans primates unveil new possibilities for the investigation of AS in humans.

Since the DS-AS transition amounts to an inversion in the timing of the pre- and postsynaptic spikes, in Chapter 6 we investigated the effects of spike-timing-dependent plasticity (STDP) in our neuronal-scale models and in our large-scale networks. We showed that AS is robust and stable in neuronal populational models in the presence of STDP. The interplay between STDP and AS regulates the distribution of synaptic weights, which can be compared to experimental weights distribution from the cortex. Moreover, it stabilizes the unlimited growth of some synaptic conductances in the absence of arbitrary chosen upper boundary to them.

Improvements in our study can be accomplished in several directions. In the theoretical point of view, our models can be modified in a plethora of ways. In the following, we suggest several situations in which further investigations on neuronal AS regimes may be relevant:



on the existence of AS between bursting neuron models as well as in chaotic neuron models; on the relation between Type-I and Type-II PRCs and the existence of AS; on the effect that the inclusion of delays in synaptic conductance may have in AS and in the AS-DS transition. In addition, one could investigate existence of AS in a neuron mass model [189], which is a mesoscale model that employs few differential equation to describe entire cortical columns. All the distinct neuron mass models present internal inhibition which can mediate the inhibitory loop required for AS.

Other biophysical models should be proposed to relate AS and phenomena such as the delayed induced transition in visually guided movements [31] as suggested by Voss [4]. Moreover, the inversion in the order of pre-post and post-pre spikes could also be useful as a mechanism to facilitate unsupervised learning. A more realistic model for the motor neurons in spinal cord could, in principle, relate AS regimes and our reaction time. Another relevant step would be the investigation of an AS regime beyond brain models, as for example, in gene regulation dynamical models that exhibit inhibitory loops [190].

Our work is a step further towards a better insight on the relation between concepts of anticipatory behavior and AS dynamics [144, 145]. However, there are still countless questions that should be answered in order to understand the mechanisms underlying our capacity of predict and act based on our models of the world. In the experimental point of view, we expect that the analysis of EEG data will be able to reveal the same mismatch between causality and phase lag which was reported in LFP measures. Since the EEG is a non-invasive technique, AS could be verified in humans.

Doubtless, more experiments should be performed in order to answer several questions about the existence and functionality of AS in the brain. What is the role of the time delay (specially in the AS regime) during learning tasks and/or in the performance of a specific task. Is AS specially related to the working memory task reported by Salazar et al. [71], or to the premovement period of the GO/NO-GO task reported by Brovelli et al. [70]? Is AS just an epiphenomenon? Which are the advantages of patterns of coherence with different time delays? Investigation of these questions could enlighten the functional significance of the AS regime on the cognitive process. Altogether, we hope that this Thesis could stimulate the research in this new and interesting field of anticipated synchronization in biological systems.



# Bibliography

- [1] M. Sigman. La máquina que construye la realidad. *TEDxBuenosAires*, 2010. <http://tedxtalks.ted.com/video/TEDxBuenosAires-Mariano-Sigman>. 1
- [2] G. Buzsaki. *Rhythms of the Brain*. Oxford University Press (New York), 2006. 1
- [3] S. Boccaletti, J. Kurths, G. Osipov, D. L. Valladares, and C. S. Zhou. The synchronization of chaotic systems. *Phys. Rep.*, 366(1-2):1 – 101, 2002. 1.1
- [4] H. U. Voss. Anticipating chaotic synchronization. *Phys. Rev. E*, 61:5115, 2000. 1.1, 1.1, 1.1, 1.1.1, 4.8.1, 5, 7
- [5] H. U. Voss. Dynamic long-term anticipation of chaotic states. *Phys. Rev. Lett.*, 87(1):014102, 2001. 1.1, 1.1, 1.1, 1.1.1, 5
- [6] H. U. Voss. Erratum: Anticipating chaotic synchronization [phys. rev. e 61, 5115 (2000)]. *Phys. Rev. E*, 64(3):039904, 2001. 1.1, 1.1, 1.1, 1.1.1, 5
- [7] C. Masoller. Anticipation in the synchronization of chaotic semiconductor lasers with optical feedback. *Phys. Rev. Lett.*, 86(13):2782–2785, 2001. 1.1.1
- [8] C. Masoller and D. H. Zanette. Anticipated synchronization in coupled chaotic maps with delays. *Physica A*, 300(3-4):359 – 366, 2001. 1.1.1, 4.8.1
- [9] E. Hernández-García, C. Masoller, and C.R. Mirasso. Anticipating the dynamics of chaotic maps. *Phys. Lett. A*, 295:39–43, 2002. 1.1.1
- [10] S. Sivaprakasam, E. M. Shahverdiev, P. S. Spencer, and K. A. Shore. Experimental demonstration of anticipating synchronization in chaotic semiconductor lasers with optical feedback. *Phys. Rev. Lett.*, 87(15):154101, 2001. 1.1.1, 4.8.1
- [11] Y. Liu, Y. Takiguchi, P. Davis, T. Aida, S. Saito, and Liu J .M. Experimental observation of complete chaos synchronization in semiconductor lasers. *Appl. Phys. Lett.*, 80(23):4306, 2002. 1.1.1
- [12] S. Tang and J. M. Liu. Experimental verification of anticipated and retarded synchronization in chaotic semiconductor lasers. *Phys. Rev. Lett.*, 90:194101, 2003. 1.1.1, 4.8.1
- [13] H. U. Voss. Real-time anticipation of chaotic states of an electronic circuit. *Int. J. Bifurcation Chaos Appl. Sci. Eng.*, 12:1619, 2002. 1.1.1

- [14] M. Ciszak, C. R. Mirasso, R. Toral, and O. Calvo. Predict-prevent control method for perturbed excitable systems. *Phys. Rev. E*, 79(4):046203, 2009. [1.1.1](#), [1.1.2](#), [1.1.2.1](#), [4.8.1](#)
- [15] A. N. Pisarchik, R. Jaimes-Reategui, and H. Garcia-Lopez. Synchronization of coupled bistable chaotic systems: experimental study. *Phil. Trans. R. Soc. A*, 366:459–473, 2008. [1.1.1](#)
- [16] J. N. Blakely, M. W. Pruitt, and N. J. Corron. Time shifts and correlations in synchronized chaos. *Chaos*, 18:013117, 2008. [1.1.1](#)
- [17] K. Srinivasan, D. V. Senthilkumar, K. Murali, M. Lakshmanan, and J. Kurths. Anticipating, complete and lag synchronizations in rc phase-shift network based coupled chuaâs circuits without delay. *Chaos*, 21:023119, 2011. [1.1.1](#)
- [18] K. Srinivasan, D. V. Senthilkumar, R. Mohamed, K. Murali, M. Lakshmanan, and J. Kurths. Anticipating, complete and lag synchronizations in rc phase-shift network based coupled chuaâs circuits without delay. *Chaos*, 22:023124, 2012. [1.1.1](#)
- [19] O. Calvo, D. R. Chialvo, V. M. Eguíluz, C. R. Mirasso, and R. Toral. Anticipated synchronization: a metaphorical linear view. *Chaos*, 14:7, 2004. [1.1.1](#)
- [20] M. Kostur, P. Hänggi, P. Talkner, and J. L. Mateos. Anticipated synchronization in coupled inertial ratchets with time-delayed feedback: A numerical study. *Phys. Rev. E*, 72(3):036210, 2005. [1.1.1](#), [4.8.1](#)
- [21] H. J. Wang, H. B. Huang, and G. X. Qi. Long-time anticipation of chaotic states in time-delay coupled ring and linear arrays. *Phys. Rev. E*, 71:015202, Jan 2005. [1.1.1](#)
- [22] H. J. Wang, H. B. Huang, and G. X. Qi. Coexistence of anticipated and layered chaotic synchronization in time-delay systems. *Phys. Rev. E*, 72:037203, Sep 2005. [1.1.1](#)
- [23] D. V. Senthilkumar and M. Lakshmanan. Transition from anticipatory to lag synchronization via complete synchronization in time-delay systems. *Phys. Rev. E*, 71:016211, Jan 2005. [1.1.1](#)
- [24] G. Ambika and R. E. Amritkar. Anticipatory synchronization with variable time delay and reset. *Phys. Rev. E*, 79:056206, May 2009. [1.1.1](#)
- [25] H. Weia and L. Li. Estimating parameters by anticipating chaotic synchronization. *Chaos*, 20:023112, 2010. [1.1.1](#)
- [26] M. Ciszak, J. M. Gutiérrez, A. S. Cofiño, C. R. Mirasso, R. Toral, L. Pesquera, and S. Ortín. Approach to predictability via anticipated synchronization. *Phys. Rev. E*, 72:046218, 2005. [1.1.1](#), [2.5](#)
- [27] S. Xu, Y. Yang, and L. Song. Control-oriented approaches to anticipating synchronization of chaotic deterministic ratchets. *Phys. Lett. A*, 373:2226–2236, 2009. [1.1.1](#)

- [28] C. Mayol, C. R. Mirasso, and R. Toral. Anticipated synchronization and the predict-prevent control method in the fitzhugh-nagumo model system. *Phys. Rev. E*, 85:056216, 2012. [1.1.1](#)
- [29] K. Pyragas and T. Pyragienė. Coupling design for a long-term anticipating synchronization of chaos. *Phys. Rev. E*, 78:046217, 2008. [1.1.1](#), [4.8.1](#)
- [30] N. J. Corron, J. N. Blakely, and S. D. Pethel. Lag and anticipating synchronization without time-delay coupling. *Chaos*, 15:023110, 2005. [1.1.1](#), [1.1.2](#)
- [31] P. Tass, J. Kurths, M. G. Rosenblum, G. Guasti, and H. Hefter. Delay-induced transitions in visually guided movements. *Phys. Rev. E*, 54:R2224–R2227, Sep 1996. [1.1.2](#), [4.8.1](#), [7](#)
- [32] P. A. Tass. *Phase Resetting in Medicine & Biology*. Springer (Berlin), 1999. [1.1.2](#)
- [33] M. Cizak, O. Calvo, C. Masoller, C. R. Mirasso, and R. Toral. Anticipating the response of excitable systems driven by random forcing. *Phys. Rev. Lett.*, 90:204102, 2003. [1.1.2](#), [1.1](#), [1.1.2.1](#), [2](#), [4.8.1](#)
- [34] M. Cizak, F. Marino, R. Toral, and S. Balle. Dynamical mechanism of anticipating synchronization in excitable systems. *Phys. Rev. Lett.*, 93:114102, 2004. [1.1.2](#), [1.1.2.1](#)
- [35] R. Toral, C. Masoller, C. R. Mirasso, M. Cizak, and O. Calvo. Characterization of the anticipated synchronization regime in the coupled FitzHugh-Nagumo model for neurons. *Physica A*, 325:192, 2003. [1.1.2](#)
- [36] T. Pyragienė and K. Pyragas. Anticipating spike synchronization in nonidentical chaotic neurons. *Nonlinear Dynamics*, pages 1–10, 2013. [1.1.2](#), [4.8.1](#)
- [37] E. R. Kandel, J. H. Schwartz, and T. M. Jessell, editors. *Essentials of Neural Science and Behavior*. Appleton & Lange, Norwalk, 1995. [1.1.2.1](#), [2.7.3](#)
- [38] A. Arvanitaki. Effects evoked in an axon by the activity of a contiguous one. *J. Neurophysiol*, 5(2):89–108, 1942. [1.1.2.1](#)
- [39] F. S. Matias, P. V. Carelli, C. R. Mirasso, and M. Copelli. Anticipated synchronization in a biologically plausible model of neuronal motif. *Phys. Rev. E*, 84:021922, 2011. [1.1.2.1](#), [2](#), [4.8.1](#), [5.1](#)
- [40] R. Milo, S. Shen-Orr, S. Itzkovitz, N. Kashtan, D. Chklovskii, and U. Alon. Network motifs: Simple building blocks of complex networks. *Science*, 298:824–827, 2002. [1.1.2.1](#), [2.1](#)
- [41] O. Sporns and R. Kötter. Motifs in brain networks. *PLoS Biology*, 2(11):e369, 10 2004. [1.1.2.1](#), [2.1](#)

- [42] G. M. Shepherd, editor. *The Synaptic Organization of the Brain*. Oxford University Press, New York, 1998. [1.1.2.1](#), [2.1](#), [4.6](#)
- [43] U. Kim, M. V. Sanchez-Vives, and D. A. McCormick. Functional dynamics of GABAergic inhibition in the thalamus. *Science*, 278(130):130–134, 1997. [1.1.2.1](#), [2.1](#)
- [44] D. Debay, J. Wolfart, Y. Le Franc, G. Le Masson, and T. Bal. Exploring spike transfer through the thalamus using hybrid artificial-biological neuronal networks. *J. Physiol.*, pages 540–558, 2004. [1.1.2.1](#), [2.1](#)
- [45] Sporns O., editor. *Networks of the brain*. The MIT Press (Cambridge), 2011. [1.2](#), [1.2.3](#)
- [46] A. L. Hodgkin and A. F. Huxley. A quantitative description of membrane current and its application to conduction and excitation in nerve. *J. Neurophysiol.*, 117:500–544, 1952. [1.2.1](#), [1.2.1](#), [2.1.1](#)
- [47] C. M. Jeffrey and P. C. Erik. Somatic epsp amplitude is independent of synapse location in hippocampal pyramidal neurons. *Nature*, 3:895–903, 2000. [1.2.1](#)
- [48] M. Migliore, M. L. Hines, and Shepherd G. M. The role of distal dendritic gap junctions in synchronization of mitral cell axonal output. *J. Comp. Neurosc.*, 18:151–161, 2005. [1.2.1](#)
- [49] L. L. Gollo, O. Kinouchi, and M. Copelli. Active dendrites enhance neuronal dynamic range. *PLoS Comput. Biol.*, 5(6):e1000402, 2009. [1.2.1](#)
- [50] R. FitzHugh. Thresholds and plateaus in the Hodgkin-Huxley nerve equations. *J. Gen. Physiol.*, 43:867–896, 1960. [1.2.1](#)
- [51] E.M. Izhikevich. Simple model of spiking neurons. *IEEE Transaction on Neural Networks*, 14(6):1569, 2003. [1.2.1](#), [4.1](#), [4.1.1](#)
- [52] G. B. Ermentrout and N. Kopell. Parabolic bursting in an excitable system couples with a slow oscillation. *SIAM J Applied Mathematics*, 46:233–253, 1986. [1.2.1](#), [3.4.3](#)
- [53] E.M. Izhikevich. Which model to use for cortical spiking neurons? *IEEE Transaction on Neural Networks*, 15(5):1063, 2004. [1.3](#), [1.2.1](#), [2.6.2](#)
- [54] C. Koch. *Biophysics of Computation*. Oxford University Press, New York, 1999. [1.2.1](#), [1.4](#), [2.1.1](#), [2.1.1](#), [2.1.1](#), [2.7.3](#)
- [55] W. Gerstner and W. Kistler. *Spiking Neuron Models: Single Neurons, Populations, Plasticity*. Cambridge University Press, 2002. [1.2.1](#), [4.7](#)
- [56] T. M. Jessell and E. R. Kandel. Synaptic transmission: a bidirectional and self-modifiable form of cell-cell communication. *Cell*, 72:1–30, 1993. [1.4](#)
- [57] D. Purves, G. J. Augustine, D. Fitzpatrick, W. C. Hall, A.-S. Lamantia, J. O. McNamara, and S. M. Williams. *Neuroscience*. Sinauer Associates, second edition, 2000. [1.2.2](#)

- [58] C. Koch and I. Segev, editors. *Methods in Neuronal Modeling: From Ions to Networks*. MIT Press, 2nd edition, 1998. [1.2.2](#), [2.1.2](#), [2.1.2](#), [4.1](#)
- [59] J. R. P. Geiger, J. Lübke, A. Roth, M. Frotscher, and P. Jonas. Submillisecond ampa receptor-mediated signaling at a principal neuron-interneuron synapse. *Neuron*, 18(6):1009 – 1023, 1997. [1.2.2](#), [2.1.2](#)
- [60] M. Hausser and A. Roth. Estimating the time course of the excitatory synaptic conductance in neocortical pyramidal cells using a novel voltage jump method. *J. Neurosci.*, 17:7606–7625, 1997. [1.2.2](#), [2.1.2](#)
- [61] U. Kraushaar and P. Jonas. Efficacy and stability of quantal gaba release at a hippocampal interneuron?principal neuron synapse. *J. Neurosci.*, 20:5594–5607, 2000. [1.2.2](#), [2.1.2](#)
- [62] K. J. Friston. Functional and effective connectivity in neuroimaging: a synthesis. *Human brain mapping*, 2(1-2):56–78, 1994. [1.2.3](#), [4.4.2](#), [5.6.3](#)
- [63] X. J. Wang. Neurophysiological and computational principles of cortical rhythms in cognition. *Physiological Reviews*, 90:1195–1268, 2010. [1.2.4](#), [4](#)
- [64] P. J. Uhlhaas and W. Singer. Abnormal neural oscillations and synchrony in schizophrenia. *Nature Reviews Neuroscience*, 11:100, 2010. [1.2.4](#)
- [65] W. Singer. Neuronal synchrony: A versatile code for the definition of relations? *Neuron Review*, 24:49–65, 1999. [1.2.4](#), [4](#), [4.8.1](#)
- [66] P. Fries. A mechanism for cognitive dynamics: neuronal communication through neuronal coherence. *Trends in Cognitive Sciences*, 9(10):474–480, 2005. [1.2.4](#), [4.8.2](#), [5](#), [5.6.2](#)
- [67] A. A. Prinz and R. H. Cudmore. Dynamic clamp. 6(5):1470, 2011. [1.3](#)
- [68] G. L. Masson, S. R. Masson, D. Debay, and T. Bal. Feedback inhibition controls spike transfer in hybrid thalamic circuits. *Nature*, 417:854–858, 2002. [1.3](#), [2.6.1](#), [4.8.1](#)
- [69] D. O. Hebb. *The organization of behavior: A neuropsychological theory*. Psychology Press, 2002. [1.3](#), [6.1](#)
- [70] A. Brovelli, M. Ding, A. Ledberg, Y. Chen, R. Nakamura, and S. L. Bressler. Beta oscillations in a large-scale sensorimotor cortical network: Directional influences revealed by granger causality. *Proc. Natl. Acad. Sci. USA*, 101(26):9849–9854, 2004. [1.3](#), [4.4.1](#), [4.8.2](#), [5](#), [5.2](#), [5.3.1](#), [5.4](#), [5.2](#), [5.5](#), [5.5.1](#), [5.6.1](#), [5.6.3](#), [7](#)
- [71] R. F. Salazar, N. M. Dotson, S. L. Bressler, and C. M. Gray. Content-specific frontoparietal synchronization during visual working memory. *Science*, 338:1097–1100, 2012. [1.3](#), [4.8.2](#), [5](#), [5.2](#), [5.3.1](#), [5.2](#), [5.5](#), [5.5.1](#), [5.6.1](#), [7](#)

- [72] A. Destexhe and C. Bedard. Local field potential. 8(8):10713, 2013. [1.3](#)
- [73] G. B. Mindlin and R. Laje. *The Physics of Birdsong*. Springer, 2005. [2.1](#)
- [74] J. Rinzel and R. N. Miller. Numerical calculation of stable and unstable periodic solutions to the hodgkin-huxley equations. *Math. Biosci.*, 49(1-2):27 – 59, 1980. [2.1.1](#), [2.4](#)
- [75] S. H. Strogatz. *Nonlinear Dynamics and Chaos: with Applications to Physics, Biology, Chemistry and Engineering*. Addison-Wesley, Reading, MA, 1997. [2.2.1](#), [2.3](#)
- [76] R. Toral, C. R. Mirasso, and J. D. Gunton. System size coherence resonance in coupled FitzHugh-Nagumo models. *Europhys. Lett.*, 61:162–167, 2003. [2.3](#)
- [77] A. H. Nayfeh and D. T. Mook. *Nonlinear oscillators*. John Wiley & Sons, New York, 1979. [2.3](#)
- [78] Abeles M., editor. *Local Cortical Circuits: An Electrophysiological study*. Springer (Berlin), 1982. [2.5](#)
- [79] M. Abeles. Synfire chains. *Scholarpedia*, 4(7):1441, 2009. [2.5](#)
- [80] F. Chersi, P. F. Ferrari, and L. Fogassi. Neuronal chains for actions in the parietal lobe: a computational model. *PloS one*, 6(11):e27652, 2011. [2.5](#)
- [81] M. A. Long, D. Z. Jin, and M. S. Fee. Support for a synaptic chain model of neuronal sequence generation. *Nature*, 468(7322):394–399, 2010. [2.5](#)
- [82] D. Golomb. Neuronal synchrony measures. *Scholarpedia*, 2(1):1347, 2007. [2.6.1](#)
- [83] M. Pospischil, M. Toledo-Rodriguez, C. Monier, Z. Piwkowska, T. Bal, Y. Frégnac, H. Markram, and A. Destexhe. Minimal hodgkin–huxley type models for different classes of cortical and thalamic neurons. *Biological cybernetics*, 99(4-5):427–441, 2008. [2.6.1](#), [2.6.2](#)
- [84] A. Destexhe, D. Contreras, and M. Steriade. Mechanisms underlying the synchronizing action of corticothalamic feedback through inhibition of thalamic relay cells. *Journal of Neurophysiology*, 79(2):999–1016, 1998. [2.6.1](#)
- [85] D. A. McCormick, Z. Wang, and J. Huguenard. Neurotransmitter control of neocortical neuronal activity and excitability. *Cerebral Cortex*, 3(5):387–398, 1993. [2.6.1](#)
- [86] ModelDB accession number: 123623. [2.6.1](#)
- [87] G. D. Smith, C. L. Cox, S. M. Sherman, and J. Rinzel. Fourier analysis of sinusoidally driven thalamocortical relay neurons and a minimal integrate-and-fire-or-burst model. *Journal of Neurophysiology*, 83(1):588–610, 2000. [2.6.2](#)



- [88] R. Brette and W. Gerstner. Adaptive exponential integrate-and-fire model as an effective description of neuronal activity. *Journal of neurophysiology*, 94(5):3637–3642, 2005. [2.6.2](#)
- [89] R. Perin, T. K. Berger, and H. Markram. A synaptic organizing principle for cortical neuronal groups. *Proceedings of the National Academy of Sciences*, 108(13):5419–5424, 2011. [2.7.1](#)
- [90] Eric R Kandel, James H Schwartz, Thomas M Jessell, Agud Aparicio, and Angel Hernando Saudan. *Principios de neurociencia*. McGraw-Hill Interamericana, 2001. [2.22](#)
- [91] D. R. Ladle, E. Pecho-Vrieseling, and S. Arber. Assembly of motor circuits in the spinal cord: driven to function by genetic and experience-dependent mechanisms. *Neuron*, 56(2):270–283, 2007. [2.7.3](#)
- [92] V. W. Lin and C. M. Bono. *Spinal cord medicine: principles and practice*. Demos Medical Publishing, 2010. [2.7.3](#)
- [93] T. I. Netoff, M. I. Banks, A. D. Dorval, C. D. Acker, J. S. Haas, N. Kopell, and J. A. White. Synchronization in hybrid neuronal networks of the hippocampal formation. *Journal of neurophysiology*, 93(3):1197–1208, 2005. [3.1](#)
- [94] E. M. Izhikevich. *Dynamical systems in neuroscience*. The MIT press, 2007. [3.1](#), [3.1](#), [3.2.1](#), [4.1](#), [4.6](#)
- [95] E. M. Izhikevich and B. Ermentrout. Phase model. *Scholarpedia*, 3(10):1487, 2008. [3.1](#), [3.2.1](#), [3.4.3](#)
- [96] G. B. Ermentrout. Type I membranes, phase resetting curves and synchrony. *Neural Comput.*, 8:979–1001, 1996. [3.1](#)
- [97] C. C. Canavier. Phase response curve. *Scholarpedia*, 1(12):1332, 2006. [3.1](#), [3.2](#)
- [98] J. Rinzel and B. Ermentrout. Analysis of neural excitability and oscillations. In C. Koch and I. Segev, editors, *Methods in Neuronal Modeling: From Ions to Networks*, pages 251–292. MIT Press, 2nd edition, 1998. [3.1](#)
- [99] D. Sterratt, B. Graham, A. Gillies, and D. Willshaw. *Principles of Computational Modelling in Neuroscience*. Cambridge University Press, 2011. [3.2](#)
- [100] C. C. Canavier and S. Achuthan. Pulse coupled oscillators. *Scholarpedia*, 2(4):1331, 2007. [3.2.1](#), [3.3](#), [3.3](#)
- [101] G. B. Ermentrout and N. Kopell. Multiple pulse interactions and averaging in systems of coupled neural oscillators. *Journal of Mathematical Biology*, 29(3):195–217, 1991. [3.2.1](#)

- [102] D. Hansel, G. Mato, and C. Meunier. Synchrony in excitatory neural networks. *Neural computation*, 7(2):307–337, 1995. [3.2.1](#)
- [103] R. E. Mirollo and S. H. Strogatz. Synchronization of pulse-coupled biological oscillators. *SIAM Journal on Applied Mathematics*, 50(6):1645–1662, 1990. [3.3](#)
- [104] R. Brette. Computing with neural synchrony. *PLoS Comput. Biol.*, 8:e1002561, 06 2012. [4](#), [4.5](#), [5.6.2](#)
- [105] S. Banerjee, A. C. Snyder, S. Molholm, and J. J. Foxe. Oscillatory alpha-band mechanisms and the deployment of spatial attention to anticipated auditory and visual target locations: Supramodal or sensory-specific control mechanisms? *The Journal of Neuroscience*, 31(27), 2011. [4](#)
- [106] P. J. Uhlhaas, G. Pipa, B. Lima, L. Melloni, S. Neuenschwander, D. Nikolić, and W. Singer. Neural synchrony in cortical networks: history, concept and current status. *Front. Integr. Neurosci.*, 3:17, 2009. [4](#)
- [107] M. Siegel, T. H. Donner, and A. K. Engel. Spectral fingerprints of large-scale neuronal interactions. *Nat. Rev. Neurosci.*, 13:121–134, 2012. [4](#), [4.8.2](#), [5](#), [5.6.3](#)
- [108] R. Vicente, L.L. Gollo, C.R. Mirasso, I. Fischer, and G. Pipa. *PNAS*, 105:17157–17162, 2008. [4.1.1](#), [4.4.2](#), [4.6](#)
- [109] D. Battaglia, A. Witt, F. Wolf, and T. Geisel. Dynamic effective connectivity of inter-areal brain circuits. *PLoS Comput. Biol.*, 393:18–21, 1998. [4.2.1](#), [4.4.2](#), [4.8.2](#), [5.6.2](#), [5.6.3](#)
- [110] H. Haken, J. A. S. Kelso, and H. Bunz. A theoretical model of phase transitions in human hand movements. *Biological cybernetics*, 51(5):347–356, 1985. [4.2.1](#)
- [111] T. Ditzinger and H. Haken. Oscillations in the perception of ambiguous patterns a model based on synergetics. *Biological Cybernetics*, 61(4):279–287, 1989. [4.2.1](#)
- [112] E. D. Lumer, K. J. Friston, and G. Rees. Neural correlates of perceptual rivalry in the human brain. *Science*, 280(5371):1930–1934, 1998. [4.2.1](#)
- [113] R. Moreno-Bote, J. Rinzel, and N. Rubin. Noise-induced alternations in an attractor network model of perceptual bistability. *Journal of neurophysiology*, 98(3):1125–1139, 2007. [4.2.1](#)
- [114] G. Deco and R. Romo. The role of fluctuations in perception. *Trends in neurosciences*, 31(11):591–598, 2008. [4.2.1](#)
- [115] G. Deco, E. T. Rolls, and R. Romo. Stochastic dynamics as a principle of brain function. *Progress in neurobiology*, 88(1):1–16, 2009. [4.2.1](#)

- [116] G. Deco, V. K. Jirsa, and A. R. McIntosh. Emerging concepts for the dynamical organization of resting-state activity in the brain. *Nature Reviews Neuroscience*, 12(1):43–56, 2010. [4.2.1](#)
- [117] C. J. Honey, R. Kötter, M. Breakspear, and O. Sporns. Network structure of cerebral cortex shapes functional connectivity on multiple time scales. *Proc. Natl. Acad. Sci. USA*, 104(24):10240–10245, 2007. [4.4.1](#), [4.4.2](#), [4.8.1](#)
- [118] L. L. Gollo, C. Mirasso, and A. E. P. Villa. Dynamic control for synchronization of separated cortical areas through thalamic relay. *Neuroimage*, 52:947, 2010. [4.6](#)
- [119] M. Steriade and R. R. Llinás. The functional states of the thalamus and the associated neuronal interplay. *Physiological reviews*, 68(3):649–742, 1988. [4.6](#)
- [120] A. E. P. Villa. Cortical modulation of auditory processing in the thalamus. *Virtual lesions: Examining Cortical Function with reversible Deactivation*, pages 83–119, 2002. [4.6](#)
- [121] S. R. Olsen, D. S. Bortone, H. Adesnil, and M Scanziani. Gain control by layer six in cortical circuit of vision. *Nature*, 483:47–52, 2012. [4.6](#)
- [122] What matters in neuronal locking. *Neural Comput.*, 8. [4.7](#), [4.7](#)
- [123] K. E. Stephan, K. Zilles, and R. Kötter. Coordinate-independent mapping of structural and functional data by objective relational transformation (ort). *Phil. Trans. R. Soc. Lond. B*, 355:37–54, 2000. [4.8.1](#)
- [124] D. J. Felleman and D. C. Van Essen. Distributed hierarchical processing in the primate cerebral cortex. *Cerebral cortex*, 1(1):1–47, 1991. [4.8.1](#)
- [125] R. Yuste, J. N. MacLean, J. Smith, and A. Lansner. The cortex as a central pattern generator. *Nat. Rev. Neurosci.*, 6:477–483, 2005. [4.8.1](#)
- [126] L. M. Kay and S. M. Sherman. An argument for an olfactory thalamus. *Trends in Neuroscience*, 30(2):47–53, 2006. [4.8.1](#)
- [127] J. Fell and N. Axmacher. The role of phase synchronization in memory processes. *Nat. Rev. Neurosci.*, 12:105–118, 2011. [4.8.2](#), [5](#)
- [128] F. Varela, J. P. Lachaux, E. Rodriguez, and J. Martinerie. The brainweb: Phase synchronization and large-scale integration. *Nat. Rev. Neurosci.*, 2:229–239, 2001. [4.8.2](#), [5](#)
- [129] K. Benchenane, A. Peyrache, M. Khamassi, P. L. Tierney, Y. Gioanni, F. P. Battaglia, and S. I. Wiener. Coherent theta oscillations and reorganization of spike timing in the hippocampal- prefrontal network upon learning. *Neuron*, 66(6):921–936, 2010. [4.8.2](#)

- [130] M. W. Jones and M. A. Wilson. Theta rhythms coordinate hippocampalâprefrontal interactions in a spatial memory task. *PLoS Biology*, 3(12):2187–2199, 2005. 4.8.2
- [131] G. G. Gregoriou, S. J. Gotts, H. Zhou, and Desimone R. High-frequency, long range coupling between prefrontal and visual cortex during attention. *Science*, 324:1207–1210, 2009. 4.8.2, 5
- [132] R. Rajagovindan and M. Ding. Decomposing neural synchrony: Toward an explanation for near-zero phase-lag in cortical oscillatory networks. *PLoS One*, 3(11), 2008. 4.8.2
- [133] S. L. Bressler, C. G. Richter, Y. Chen, and M. Ding. Top-down cortical influences in visual expectation. In *Neural Networks, 2006. IJCNN'06. International Joint Conference on*, pages 188–194. IEEE, 2006. 4.8.2
- [134] M. Bartos, I. Vida, M. Frotscher, A. Meyer, H. Monyer, J. R. P. Geiger, and P. Jonas. Fast synaptic inhibition promotes synchronized gamma oscillations in hippocampal interneuron networks. *Proc. Natl. Acad. Sci. USA*, 99(20), 2002. 4.8.2
- [135] S. Oláh, M. Füle, G. Komlósi, C. Varga, R. Báldi, P. Barzó, and G. Tamás. Regulation of cortical microcircuits by unitary gaba-mediated volume transmission. *Nature*, 461(7268):1278–1281, 2009. 4.8.2
- [136] A. Pikovsky, M. Rosenblum, and J. Kurths. *Synchronization: A Universal Concept in Nonlinear Sciences*. Cambridge University Press, Cambridge, UK, 2001. 5
- [137] S. L. Bressler and V. Menon. Large-scale brain networks in cognition: emerging methods and principles. *Trends in Cognitive Sciences*, 14(6):277–290, 2010. 5
- [138] J. F. Marsden, P. Limousin-Dowsey, P. Ashby, P. Pollak, and P. Brown. Subthalamic nucleus, sensorimotor cortex and muscle interrelationships in parkinson's disease. *Brain*, 124(2):378–388, 2001. 5
- [139] D. Williams, M. Tijssen, G. van Bruggen, A. Bosch, A. Insola, V. D. Lazzaro, P. Mazzone, A. Oliviero, A. Quartarone, H. Speelman, and P. Brown. Dopamindependent changes in the functional connectivity between basal ganglia and cerebral cortex in humans. *Brain*, 125(7):1558–1569, 2002. 5
- [140] A. Schnitzler and J. Gross. Normal and pathological oscillatory communication in the brain. *Nat. Rev. Neurosci.*, 6:285–296, 2005. 5
- [141] P. Sauseng and W. Klimesch. What does phase information of oscillatory brain activity tell us about cognitive processes? *Neuroscience & Biobehavioral Reviews*, 32(5):1001–1013, 2008. 5
- [142] C. W. J. Granger. Investigating causal relations by econometric models and cross-spectral methods. *Econometrica*, 37(3):pp. 424–438, 1969. 5

- [143] S. L. Bressler and A. K. Seth. Wienergranger causality: A well established methodology. *NeuroImage*, 58(2):323–329, 2011. 5, 5.3.1
- [144] N. Stepp and M. T. Turvey. On strong anticipation. *Cognitive Systems Research*, 11(2):148–164, 2010. 5, 7
- [145] D. G. Stephen and J. A. Dixon. Coordinate-independent mapping of structural and functional data by objective relational transformation (ort). *Chaos, Solitons and Fractals*, 44:160–168, 2011. 5, 7
- [146] A. Seth. Granger causality. *Scholarpedia*, 2(7):1667, 2007. 5.3, 5.3, 5.3.1
- [147] M. Ding, Y. Chen, and S. L. Bressler. 17 granger causality: Basic theory and application to neuroscience. *Handbook of time series analysis*, page 437, 2006. 5.3, 5.3
- [148] H. Liang, M. Ding, R. Nakamura, and S. L. Bressler. Causal influences in primate cerebral cortex during visual pattern discrimination. *Neuroreport*, 11(13):2875–2880, 2000. 5.3.1
- [149] M. Kamiński, M. Ding, W. A Truccolo, and S. L. Bressler. Evaluating causal relations in neural systems: Granger causality, directed transfer function and statistical assessment of significance. *Biological cybernetics*, 85(2):145–157, 2001. 5.3.1
- [150] A. Roebroeck, E. Formisano, and R. Goebel. Mapping directed influence over the brain using granger causality and fmri. *Neuroimage*, 25(1):230–242, 2005. 5.3.1
- [151] J. R. Sato, E. A. Junior, D. Y. Takahashi, M. de Maria Felix, M. J. Brammer, and P. A. Morettin. A method to produce evolving functional connectivity maps during the course of an fmri experiment using wavelet-based time-varying granger causality. *Neuroimage*, 31(1):187–196, 2006. 5.3.1
- [152] W. Liao, J. Ding, D. Marinazzo, Q. Xu, Z. Wang, C. Yuan, Z. Zhang, G. Lu, and H. Chen. Small-world directed networks in the human brain: multivariate granger causality analysis of resting-state fmri. *Neuroimage*, 54(4):2683–2694, 2011. 5.3.1
- [153] A. K. Seth. Causal connectivity of evolved neural networks during behavior. *Network: Computation in Neural Systems*, 16(1):35–54, 2005. 5.3.1
- [154] A. K. Seth and G. M. Edelman. Distinguishing causal interactions in neural populations. *Neural Computation*, 19(4):910–933, 2007. 5.3.1
- [155] G. Nolte, A. Ziehe, V. V. Nikulin, A. Schlögl, N. Krämer, T. Brismar, and K. R. Müller. Robustly estimating the flow direction of information in complex physical systems. *Phys. Rev. Lett.*, 100:234101, Jun 2008. 5.3.1
- [156] J. P. Lachaux, E. Rodriguez, J. Martinerie, F. J. Varela, et al. Measuring phase synchrony in brain signals. *Human brain mapping*, 8(4):194–208, 1999. 5.3.1

- [157] G. Nolte, O. Bai, L. Wheaton, Z. Mari, S. Vorbach, and M. Hallett. Identifying true brain interaction from eeg data using the imaginary part of coherency. *Clinical Neurophysiology*, 115(10):2292–2307, 2004. [5.3.1](#)
- [158] M. Vinck, R. Oostenveld, M. van Wingerden, F. Battaglia, and C. Pennartz. An improved index of phase-synchronization for electrophysiological data in the presence of volume-conduction, noise and sample-size bias. *Neuroimage*, 55(4):1548–1565, 2011. [5.3.1](#)
- [159] M. Vinck, M. van Wingerden, T. Womelsdorf, P. Fries, and C. Pennartz. The pairwise phase consistency: a bias-free measure of rhythmic neuronal synchronization. *Neuroimage*, 51(1):112–122, 2010. [5.3.1](#)
- [160] E. Pereda, R. Q. Quiroga, and J. Bhattacharya. Nonlinear multivariate analysis of neurophysiological signals. *Progress in neurobiology*, 77(1):1–37, 2005. [5.3.1](#)
- [161] A. Seth. A matlab toolbox for granger causal connectivity analysis. *Journal of Neuroscience Methods*, 186:262–273, 2010. [5.4](#)
- [162] H. Akaike. A new look at the statistical model identification. *Automatic Control, IEEE Transactions on*, 19(6):716–723, 1974. [5.4](#)
- [163] H. Lütkepohl. *Introduction to Multiple Time Series Analysis*. Springer, Berlin, 1993. [5.4](#)
- [164] Y. Zhang, Y. Chen, S. L. Bressler, and M. Ding. Response preparation and inhibition: The role of the cortical sensorimotor beta rhythm. *Neuroscience*, 156(1), 2008. [5.5.1](#)
- [165] A. Sharott, P. J. Peter J Magill, J. P. Bolam, and P. Brown. Directional analysis of coherent oscillatory field potentials in the cerebral cortex and basal ganglia of the rat. *The Journal of Physiology*, 562, 2005. [5.6.1](#)
- [166] B.W.A. Feenstra and J. Holsheimer. Dipole-like neuronal sources of theta rhythm in dorsal hippocampus, dentate gyrus and cingulate cortex of the urethane-anesthetized rat. *Electroencephalography and Clinical Neurophysiology*, 47:532–538, 1979. [5.6.1](#)
- [167] J. J. Chrobak and G. Buzsáki. Gamma oscillations in the entorhinal cortex of the freely behaving rat. *J. Neurosci.*, 18:388–398, 1998. [5.6.1](#)
- [168] A. Alonso and E. GarcíaAustt. Neuronal sources of theta rhythm in the entorhinal cortex of the rat. ii. phase relations between unit discharges and theta field potentials. *Rev. Mod. Phys.*, 67:502–509, 1987. [5.6.1](#)
- [169] S.L. Bressler and J.A.S. Kelso. Cortical coordination dynamics and cognition. *Trends in Cognitive Sciences*, 5(1):26–36, 2001. [5.6.2](#)
- [170] E. B. Anderson, J. F. Mitchell, and H. Reynolds, J. Attention-dependent reductions in burstiness and action-potential height in macaque area v4. *Nat. Neurosci.*, 16:1125–1131, 2013. [5.6.2](#)

- [171] D. W. Hahs and S. D. Pethel. Distinguishing anticipation from causality: Anticipatory bias in the estimation of information flow. *Phys. Rev. Lett.*, 107:128701, Sep 2011. 5.6.3
- [172] H. Markram, W. Gerstner, and P. J. Sjöström. A history of spike-timing-dependent plasticity. *Frontiers in Synaptic Neuroscience*, 3(0004):1–24, 2011. 6, 6.1, 6.1.1
- [173] T. V. P. Bliss and T. Lømo. Long-lasting potentiation of synaptic transmission in the dentate area of the anaesthetized rabbit following stimulation of the perforant path. *The Journal of physiology*, 232(2):331–356, 1973. 6.1
- [174] G. S. Lynch, T. Dunwiddie, and V. Gribkoff. Heterosynaptic depression: a postsynaptic correlate of long-term potentiation. 1977. 6.1
- [175] T. Dunwiddie and G. Lynch. Long-term potentiation and depression of synaptic responses in the rat hippocampus: localization and frequency dependency. *The Journal of physiology*, 276(1):353–367, 1978. 6.1
- [176] H. Markram, J. Lübke, M. Frotscher, and B. Sakmann. Regulation of synaptic efficacy by coincidence of postsynaptic APs and EPSPs. *Science*, 275(5297):213–5, 1997. 6.1.1
- [177] G. Q. Bi and M. M. Poo. Synaptic modifications in cultured hippocampal neurons: dependence on spike timing, synaptic strength, and postsynaptic cell type. *J. Neurosci.*, 18(24):10464–72, 1998. 6.1.1, 6.1
- [178] L. I. Zhang, H. W. Tao, C. E. Holt, W. A. Harris, and M. Poo. A critical window for cooperation and competition among developing retinotectal synapses. *Nature*, 395(6697):37–44, 1998. 6.1.1
- [179] T. Celikel, V. A. Szostak, and D. E. Feldman. Modulation of spike timing by sensory deprivation during induction of cortical map plasticity. *Nature neuroscience*, 7(5):534–541, 2004. 6.1.1
- [180] S. Song, K. D. Miller, and L. F. Abbott. Competitive hebbian learning through spike-timing-dependent synaptic plasticity. *Nature neuroscience*, 3(9):919–926, 2000. 6.1.1, 6.2, 6.4.2
- [181] N. Caporale and Y. Dan. Spike timing-dependent plasticity: a hebbian learning rule. *Annu. Rev. Neurosci.*, 31:25–46, 2008. 6.1.1
- [182] A. Wolters, F. Sandbrink, A. Schlottmann, E. Kunesch, K. Stefan, L. G. Cohen, R. Benecke, and J. Classen. A temporally asymmetric hebbian rule governing plasticity in the human motor cortex. *Journal of Neurophysiology*, 89(5):2339–2345, 2003. 6.1.1
- [183] P. Dayan and L. F. Abbott. *Theoretical neuroscience: Computational and mathematical modeling of neural systems*. Taylor & Francis, 2001. 6.1.1

- [184] K. S. Burbank and G. Kreiman. Depression-biased reverse plasticity rule is required for stable learning at top-down connections. *PLoS computational biology*, 8(3):e1002393, 2012. 6.2
- [185] B. Barbour, N. Brunel, V. Hakim, and J. P. Nadal. What can we learn from synaptic weight distributions? *TRENDS in Neurosciences*, 30(12):622–629, 2007. 6.2, 6.4.2, 6.8
- [186] S. Fusi, P. J. Drew, and L. F. Abbott. Cascade models of synaptically stored memories. *Neuron*, 45(4):599–611, 2005. 6.2
- [187] J. Satel, T. Trappenberg, and A. Fine. Are binary synapses superior to graded weight representations in stochastic attractor networks? *Cognitive neurodynamics*, 3(3):243–250, 2009. 6.2
- [188] G. Billings and M. C. W. van Rossum. Memory retention and spike-timing-dependent plasticity. *Journal of neurophysiology*, 101(6):2775–2788, 2009. 6.4
- [189] G. Deco, V. K. Jirsa, P. A. Robinson, M. Breakspear, and K. Friston. The dynamic brain: from spiking neurons to neural masses and cortical fields. *PLoS computational biology*, 4(8):e1000092, 2008. 7
- [190] R. Blossey, L. Cardelli, and A. Phillips. Compositionality, stochasticity, and cooperativity in dynamic models of gene regulation. *HFSP journal*, 2(1):17–28, 2008. 7